

**RADIATION DETECTION  
USING MOBILE SENSOR NETWORKS**

by

Jianxin Sun

A dissertation submitted to the Faculty of the University of Delaware in partial fulfillment of the requirements for the degree of Doctor of Philosophy in Mechanical Engineering

Spring 2016

© 2016 Jianxin Sun  
All Rights Reserved

ProQuest Number: 10156476

All rights reserved

INFORMATION TO ALL USERS

The quality of this reproduction is dependent upon the quality of the copy submitted.

In the unlikely event that the author did not send a complete manuscript and there are missing pages, these will be noted. Also, if material had to be removed, a note will indicate the deletion.



ProQuest 10156476

Published by ProQuest LLC (2016). Copyright of the Dissertation is held by the Author.

All rights reserved.

This work is protected against unauthorized copying under Title 17, United States Code  
Microform Edition © ProQuest LLC.

ProQuest LLC.  
789 East Eisenhower Parkway  
P.O. Box 1346  
Ann Arbor, MI 48106 - 1346

**RADIATION DETECTION  
USING MOBILE SENSOR NETWORKS**

by  
Jianxin Sun

Approved: \_\_\_\_\_  
Suresh G. Advani, Ph.D.  
Chair of the Department of Mechanical Engineering

Approved: \_\_\_\_\_  
Babatunde A. Ogunnaike, Ph.D.  
Dean of the College of Engineering

Approved: \_\_\_\_\_  
Ann L. Ardis, Ph.D.  
Senior Vice Provost for Graduate & Professional Education

I certify that I have read this dissertation and that in my opinion it meets the academic and professional standard required by the University as a dissertation for the degree of Doctor of Philosophy.

Signed: \_\_\_\_\_  
Herbert G. Tanner, Ph.D.  
Professor in charge of dissertation

I certify that I have read this dissertation and that in my opinion it meets the academic and professional standard required by the University as a dissertation for the degree of Doctor of Philosophy.

Signed: \_\_\_\_\_  
Ioannis Poulakakis, Ph.D.  
Member of dissertation committee

I certify that I have read this dissertation and that in my opinion it meets the academic and professional standard required by the University as a dissertation for the degree of Doctor of Philosophy.

Signed: \_\_\_\_\_  
Guoquan Huang, Ph.D.  
Member of dissertation committee

I certify that I have read this dissertation and that in my opinion it meets the academic and professional standard required by the University as a dissertation for the degree of Doctor of Philosophy.

Signed: \_\_\_\_\_  
Ryan Zurakowski, Ph.D.  
Member of dissertation committee

## ACKNOWLEDGEMENTS

I would like to gratefully thank Dr. Herbert Tanner, for his guidance, support and patience. He introduced me to the massive body of knowledge in robotics and optimal control theories, and I always enjoy the fun of working with challenging robots. I also like to thank Dr. Chetan Pahlajani, for his rigorous work on radiation detection, which sets the prerequisite for this dissertation. I am also thankful to the committee members Dr. Ioannis Poulakakis, Dr. Guoquan Huang, and Dr. Ryan Zurakowski, for providing their valuable feedback on this research topic. This work was made possible in part by ARL MAST CTA #W911NF-08-2-000.

Sincere thanks to members of Cooperative Robotics Lab who supported this work in various ways: Shridhar Shah, for his help in bringing the quadrotors back to life; Prasanna Kannappan, for his support in visual processing programming; Adam Stager, for his brilliant crawler robot design and his help in my experiments; Konstantinos Karydis, for his study on quadrotor modeling; and Jie Fu, for her insights into problems I encountered.

Finally, I would like to thank my parents for their unconditional support and love, which is always the bedrock of my life.

## TABLE OF CONTENTS

<b>LIST OF TABLES</b> . . . . .	<b>viii</b>
<b>LIST OF FIGURES</b> . . . . .	<b>ix</b>
<b>GLOSSARY</b> . . . . .	<b>xi</b>
<b>ABSTRACT</b> . . . . .	<b>xii</b>
 <b>Chapter</b>	
<b>1 INTRODUCTION</b> . . . . .	<b>1</b>
1.1 Motivation . . . . .	1
1.2 Objective . . . . .	1
1.3 Background on Radioactive Material Detection . . . . .	2
1.4 Existing Methods . . . . .	3
1.4.1 Radiation Detection Using Passive Radiation Counters . . . . .	3
1.4.2 Visual Based Target Tracking . . . . .	5
1.4.3 Motion Planning . . . . .	5
1.4.4 Source Seeking with Limited Information . . . . .	7
1.5 Problem Statement . . . . .	8
1.6 Scientific Contributions . . . . .	9
<b>2 TECHNICAL PRELIMINARIES</b> . . . . .	<b>11</b>
2.1 Radiation Sensor Model . . . . .	12
2.2 Decision Making . . . . .	13
2.3 Chernoff Bounds on Error Probabilities of Likelihood Ratio Test . . . . .	14
2.4 Optimal Control . . . . .	15
2.5 Motion Planning . . . . .	16
2.6 Vehicle Control . . . . .	17
2.7 Extremum Seeking . . . . .	18
2.8 Stochastic Hybrid System Modeling . . . . .	19
2.9 Conclusion . . . . .	20

<b>3</b>	<b>OPTIMAL STRATEGIES FOR RADIATION DETECTION . . .</b>	<b>21</b>
3.1	Problem Statement . . . . .	22
3.2	Threshold Selection for Radiation Detection . . . . .	22
3.3	Minimize Error Bounds by Optimal Control . . . . .	25
3.3.1	Optimization Problem Formulation . . . . .	25
3.3.2	Numerical Determination of Optimal Sensor Trajectories . . .	27
3.3.3	Analytic Determination of Optimal Sensor Trajectories . . . .	30
3.4	Conclusion . . . . .	34
<b>4</b>	<b>ROBOT NAVIGATION . . . . .</b>	<b>36</b>
4.1	Problem Statement . . . . .	37
4.2	Navigation Function Construction . . . . .	38
4.3	Navigation Function Controller: Convergence . . . . .	38
4.4	Navigation Function Controller: Boundedness . . . . .	40
4.5	Conclusion . . . . .	42
<b>5</b>	<b>ROBOTIC PLATFORM INTERFACES . . . . .</b>	<b>43</b>
5.1	Problem Statement . . . . .	43
5.2	Quadrotor . . . . .	43
5.2.1	Dynamics Model . . . . .	43
5.2.2	Acceleration Controller Design . . . . .	46
5.2.3	Planar Trajectory Controller . . . . .	47
5.3	Wheeled Robot . . . . .	48
5.3.1	Kinematic Model . . . . .	48
5.3.2	Position Controller . . . . .	48
5.4	Conclusions . . . . .	49
<b>6</b>	<b>SIMULATION RESULTS . . . . .</b>	<b>51</b>
6.1	Chernoff Bounds: Monte Carlo Validation . . . . .	52
6.2	Boundedness of the Navigation Function Based Motion Planner . . .	56
6.3	Simulated Radiation Detection With Mobile Sensors . . . . .	57

6.4	Conclusion . . . . .	60
<b>7</b>	<b>EXPERIMENTAL VALIDATION . . . . .</b>	<b>61</b>
7.1	Robot Control System . . . . .	62
7.2	State Transitions in Quadrotor Controller . . . . .	66
7.3	Target Tracking Using Visual Feedback . . . . .	67
7.3.1	Quadrotor Camera System . . . . .	68
7.3.2	Image Transmission and Processing . . . . .	69
7.4	Navigation Function Based Controller Performance . . . . .	73
7.5	Laser-emulated Radiation Emissions . . . . .	75
7.5.1	Laser-emulation: Experimental Setup . . . . .	76
7.5.2	Results and Discussion . . . . .	79
7.6	Detection of Vaseline Beads Mounted on Mobile Robot . . . . .	81
7.7	Conclusion . . . . .	86
<b>8</b>	<b>SOURCE SEEKING WITH LIMITED SENSOR INFORMATION . . . . .</b>	<b>87</b>
8.1	Modeling Boundary Reflection Events . . . . .	87
8.2	Lower Bound on Probability of Reaching Field Extremum . . . . .	90
8.3	Conclusion and Next Steps . . . . .	92
<b>9</b>	<b>CONCLUSIONS AND FUTURE DIRECTIONS . . . . .</b>	<b>93</b>
	<b>BIBLIOGRAPHY . . . . .</b>	<b>95</b>
	<b>Appendix</b>	
<b>A</b>	<b>THEOREM 4.3.1: INTERMEDIATE RESULTS . . . . .</b>	<b>103</b>
<b>B</b>	<b>COPYRIGHT PERMISSIONS . . . . .</b>	<b>116</b>

## LIST OF TABLES

7.1	Optimal <a href="#">LRT</a> parameters, and detection results for the static and mobile sensor network configurations . . . . .	81
7.2	<a href="#">SNR</a> of individual sensors in the experimental tests, for static and mobile sensor network configurations . . . . .	81

## LIST OF FIGURES

3.1	Numerical Determination of Optimal Sensor Trajectory . . . . .	29
3.2	Numerical Determination of Optimal Sensor Velocity . . . . .	30
5.1	AscTec Hummingbird Command to Thrust Plot . . . . .	44
5.2	AscTec Hummingbird Coordinates System . . . . .	45
5.3	iCreate and Geiger Counter . . . . .	49
5.4	iCreate Geometric Model . . . . .	50
6.1	Simulation Setup for Monte Carlo Validation of the Chernoff Bounds	52
6.2	Validate Chernoff Bounds through Monte Carlo Simulation . . . . .	55
6.3	Simulated Flight with Navigation Function-based Controller . . . . .	56
6.4	Initial Positions in Workspace that Satisfies Bounded Control Condition . . . . .	57
6.5	Senor Trajectories in Simulated Radiation Detection With Mobile Sensors . . . . .	58
6.6	Distance-to-Target Profile in Simulated Radiation Detection With Mobile Sensors . . . . .	59
7.1	Robot Control System Layout . . . . .	64
7.2	Quadrotor State Transitions . . . . .	66
7.3	Quadrotor Onboard Sensors Assembly–Top View . . . . .	69
7.4	Quadrotor Onboard Sensors Assembly–Bottom View . . . . .	70

7.5	Target Robot Template Image . . . . .	71
7.6	Target Robot Raw Image . . . . .	72
7.7	Target Robot Detection . . . . .	72
7.8	Target Robot's Pose Transform Between Frames . . . . .	73
7.9	Navigation Function-based Controller: Comparison Between Simulated and Actual Quadrotor Flight . . . . .	74
7.10	Quadrotor Flight Distance Log . . . . .	76
7.11	Quadrotor Flight Acceleration Log . . . . .	77
7.12	Laser Emulated Radiation Detection Experiment Setup . . . . .	78
7.13	Geiger Counter Effective Area Illustration . . . . .	79
7.14	Laser Simulated Radiation Detection Experiment Result . . . . .	80
7.15	Radiation Detection of Vaseline Beads Experiment Setup . . . . .	82
7.16	Radioactive Source Intensity Characterization . . . . .	83
7.17	Visual Tracking Performance . . . . .	84
7.18	Sensor Trajectories in Radiation Detection of Vaseline Beads Experiment . . . . .	85
8.1	Markov Chain for Boundary Bouncing Robot Mode. $x$ is the robot's continuous state when starting in $(1, \mathcal{X}_1)$ . The jumps from $(1, \mathcal{X}_1)$ always happen on $\partial\mathcal{X}_1 = \mathcal{X}_2 \cup \mathcal{X}_3$ . . . . .	90

## GLOSSARY

- cpm** counts per minute
- FPS** frames per second
- IMU** Inertial Measurement Unit
- GPOPS** General Pseudospectral Optimal Control Software
- HSV** Hue Saturation Value
- LiPo** Lithium Polymer
- LRT** Likelihood Ratio Test
- NLP** Non-linear Programming
- ODE** Ordinary Differential Equation
- PID** Proportional-Integral-Derivative
- $P_{FA}$  Probability of false alarm
- $P_M$  Probability of missed detection
- PRM** Probabilistic Road Map
- PRM\*** Optimal Probabilistic Road Map
- ROS** Robot Operating System
- RRT** Rapidly exploring Random Tree
- RRT\*** Optimal Rapidly exploring Random Tree
- SDE** Stochastic Differential Equation
- SHS** Stochastic Hybrid System
- SNR** Signal-to-Noise Ratio
- SURF** Speeded Up Robust Feature

## ABSTRACT

This dissertation addresses a fixed-time interval decision making problem from an optimal control perspective, in the context of deciding the radioactive nature of a single target in transit using multiple mobile sensors. The mobility of sensors facilitates detecting extreme weak sources that may otherwise slip through stationary radiation sensor networks. However challenging problems also arise in terms of searching for the optimal way to utilize such mobility.

Based on existing work, the decision on target's radioactive nature is made through a Likelihood Ratio Test ([LRT](#)), whose probability of making mistakes are upper bounded by analytic expressions related to both [LRT](#) thresholds and trajectories of mobile sensors. This dissertation proposes a threshold selection process for the [LRT](#) based on the constraint on its false alarm rate and solves for the optimal sensor trajectories that would minimize the upper bounds on the probability of missing detection.

Under simplifying assumptions on the motion and geometry of the source, the sensors, and the surrounding environment, the optimal control problem admits an intuitive, analytic closed-form solution. The intuition derived from this analytic solution supports the development of a motion control law that steers (suboptimally) the sensors to a given neighborhood of the suspected source, while navigating among stationary obstacles in their environment. This motion controller closes the loop at the acceleration level of a heterogeneous collection of sensor platforms.

This dissertation detailed a robot control system developed for conducting the radiation detection experiment using physical platforms, which is capable of controlling multiple robots simultaneously. Experimental studies with these robots corroborate the

theoretical convergence results of the proposed navigation controller. The detection of weak radioactive source (Vaseline beads) is achieved with these sensor platforms.

The limitation of this work is that it relies on some strong localization assumptions as the optimal strategy requires the position feedback of both the robots and the target, which might be difficult to obtain in some scenarios. One extension discussed in this dissertation is to study the possibility of achieving convergence to signal extremum without global localization in cluttered environment. In this dissertation, the unavoidable collisions resulted from the lack of localization is modeled as a Markov process and the effect of these collisions on the probability of the robot successfully converging to the signal extremum is studied. Future studies on the reachability problem of the underlying stochastic hybrid system could lead to better usage of the multiple sensor platforms to survey uncertain areas.

# Chapter 1

## INTRODUCTION

### 1.1 Motivation

As the capabilities of robots grow, automated sensor deployment in hazardous environments becomes more realistic. For example, using robots for search and rescue tasks is an increasingly more practical choice in recent disaster response scenarios: quadrotors were used in searching survivors after the calamitous Sichuan earthquake of 2008; unmanned ground vehicles were there to measure radiation levels after Fukushima nuclear accident of 2011; robotic submarines also contributed to the search for MH370 in 2014. With the rapid development of robotics technology, autonomous robots that can carry out search and rescue missions are around the horizon and attract a lot of research interest.

### 1.2 Objective

This dissertation aims at studying the potential of using robots to detect the presence of weak radioactive sources in transit and assess the environmental impact of accidental or malicious release of radiological agents, by exploiting the mobility of radiation sensors when mounted on robots. Detecting radioactive sources is relevant and timely due to the increasing risk of nuclear material proliferation [2,9] and the need for inspecting vehicles and humans safely without hindering traffic and commerce.

Before mathematically defining and addressing such problems in subsequent chapters, let us walk through the available approaches to detecting radioactive sources, which shall narrow down our scope to the parts that still present challenges.

### 1.3 Background on Radioactive Material Detection

To detect radioactive sources in transit from a distance, one potential method that complements existing monitoring systems [13] is the deployment of a large network of spatially distributed detectors. Geiger counters appear to be among the few realistic choices for constructing autonomous, meso-scale mobile radiation measurement networks; larger and more sophisticated sensors (providing spectroscopy information), are prohibitively expensive to be deployed on a large scale [66], and either too heavy or too delicate to be mounted on mobile platforms. In addition, any active (e.g. X-ray) interrogation technology cannot be used to check vehicles that carry passengers or livestock [61].

However Geiger counter’s limited performance introduces serious mathematical and technical challenges. Geiger counters merely record radiation rays hitting their internal crystal, regardless of whether these rays come from the source to be detected or from naturally occurring background radiation. The question thus is whether the aggregate count is due to background alone or to the superposition of background and source. This problem can be formulated as a binary hypothesis test—if deadlines are imposed, this becomes a fixed-time interval test—that has received considerable coverage in the literature [7].

When detecting radioactive material, the perceived rate of count reception at each sensor changes with the distance between the sensor and the source, giving rise to a dynamic, time-inhomogeneous stochastic process. As a result, analytic characterization for the error probabilities in this decision problem is usually intractable, and thus upper and lower bounds are sought, and efforts to this end have been made using Chernoff bounds [21, 31, 48, 58]. Analytic bounds like these are central to designing motion control strategies for the mobile sensors that optimize detection probability.

## 1.4 Existing Methods

### 1.4.1 Radiation Detection Using Passive Radiation Counters

It should first be noted that “passive” here means that the radiation sensor considered here only counts the radiation rays emitted by source and background, without otherwise interacting with the target. The term “passive” does not mean that the sensors are necessarily static. Literature in radioactive material detection exposes the difficulties in determining the radioactivity of a target using exclusively (passive) radiation counters, motivating combining sensor modalities.

For the most part, approaches in available literature attempt to identify not only the nature of the target but also its location solely based on radiation counters [8, 15, 46]. Such approaches essentially face a combination of problems—detection and localization—which is inherently very challenging, both at analytic and computational level. For static sensors and source, a location estimator can be constructed, and a sequential probability ratio test can be formed [15]. In addition to estimating the source’s position, algorithms within a Bayesian framework can also estimate source intensity [8, 46]. How the sensor-to-source distance change affects the sensor measurement quality is explained [47]: the Signal-to-Noise Ratio (SNR) scales with the inverse square of the distance, which means the contribution to radiation detection of a small sensor closer to the source is equivalent to that of a much bigger sensor at a longer distance.

Utilizing mobility in nuclear measurement has recently been studied [19, 34, 43], but their research directions are different from the one in this dissertation. To achieve network coverage, randomized sensor motion is utilized [43]; to fulfill the radiation mapping task, controller for sensor motion is designed [19]; and to determine the existence of static sources, predetermined [38] or information-driven [55, 56] sensor motion controller are proposed. These methods often require that during each observation period, the mean radiation intensities observed by sensors remain constant. If the distance between sensors and source change dynamically while measurements are taken, the observed radiation counts follows a time-inhomogeneous Poisson distribution that

must be treated differently.

It is also not entirely clear about the direct relation between sensor mobility and the performance of these radiation measuring tasks. Several performance measures that relates the sensor motion to nuclear measurement are proposed, such as the variance of the expected radiation intensity at individual spatial bin [34, 38], and various information-theoretic measures [18, 55, 56]. Although these are intuitive choices, they may be considered equally arbitrary from the perspective of the decision maker. Because it is not clear how the direct performance metrics, such as detection rate and false alarm rate, depend explicitly on sensor mobility, and how they can be optimized.

Published results support the hypothesis that sensor networks can be effective in remotely detecting static radiation sources [8]. When the source is in motion, however, the associated analytic complexity translates to significantly increased computational complexity, and updating posterior probabilities using Bayes rule becomes problematic, even for networks of modest size [14, 46] and under assumptions on the motion of the source being linear with constant velocity or acceleration.

This dissertation focuses on one of the constituent problems—namely, detection. That is to study what is the best that can be done about sensor deployment for detection task, under the *assumption* that the emission characteristics and trajectory of the source are known. The rationale behind this divide-and-conquer strategy is that on one hand, given the security application in mind, one probably may have an idea of the type of material that is expected to be found. On the other hand, a multitude of other sensing modalities (e.g. cameras [75]—see Section 1.4.2) can be used to detect and track a mobile target; one does not need to track motion based solely on Geiger counters.

In existing literature, the sensors’ motion are not directly related to the detection performance, i.e, error probabilities, but the focus is more on exploring the workspace following indirect metrics or even predetermined paths. The approach in this dissertation, on the contrary, directly minimizes the upper bound on error probability and

focuses on the target detection problem. The assumption that the target can be localized has led to the determination of Chernoff bounds on error probabilities [49], which are utilized here to formulate an optimal sensor motion control problem. The optimal motion solutions based on those bounds drive the mobile robots to minimize the Chernoff bounds of the probabilities of error with respect to their control inputs. Unlike information theory based metrics [18, 55, 56], these error probability bounds directly measure the reliability of the decision made by detection process.

#### **1.4.2 Visual Based Target Tracking**

Target tracking using vision, laser, sonar and other sensor measurements is widely used in autonomous robot technologies. This utilization supports the assumption that sensory perceptions other than mere radiation measurements can inform about the motion of the target.

Cameras on unmanned aerial vehicles have shown great potential in recognizing and tracking targeted subjects [4, 17, 28]. In the same spirit, studies on simultaneously monitoring and detecting abnormal behavior in crowds [59] can be valuable in generating potential target lists for radiation detection process. Multi-robot tracking problems also attract a lot attention for applications in surveillance [68, 78, 79]. Using multiple sensor modalities [60] contributes to robust target tracking. Model-based target motion prediction [53, 71] can offer information on target motion when tracking mobile targets. Yet, working with mobile sensors, including the field of view constraint [23] as part of the motion planning can be challenging. These studies offer evidence that target localization using sensors other than radiation counters can help reveal the nature of a potentially radioactive target.

#### **1.4.3 Motion Planning**

In this dissertation, assumptions are made that motion of target can be acquired via means other than those based on radiation measurements. Based on this assumption, the motion planning problem that guides sensor nodes towards time-varying

target in complex environments is studied. Existing motion planning methods face challenges when targets are moving. Sampling based methods have to handle trade offs between performance and optimality. Their computation cost is not quite suitable yet for real-time, onboard implementation on small scale robots. On the other hand, potential-based methods are not developed to natively handle time-varying targets in cluttered environments, and does not provide optimality guarantees. There is a need for better navigation methods that can adapt to the dynamics of robots while minimizing computation cost.

The particular motion planning problem considered here is an instance of a general *time-varying* problem of navigating amongst obstacles. When it is the environment that is time-varying, e.g., the obstacles are moving, the problem has been approached from the perspective of roadmaps [80]. Optimal trajectories can be generated based on these roadmaps; however, as the dimensionality of the problem—primarily due to multiple platforms—increases, computational complexity presents some serious challenges. Alternatives that promise to preserve optimality (at least asymptotically) at a smaller computational cost, including Optimal Probabilistic Road Map (PRM\*) and Optimal Rapidly exploring Random Tree (RRT\*) [32]. These algorithms have been adapted to various situations that require fast generation of new solutions amongst obstacles [16, 44, 52]. Although asymptotically optimal in theory, appropriate extension heuristics have to be carefully chosen. At the end, there is always a trade-off between real-time performance and optimality.

Dealing with dynamic environments in real-time presents computational challenges to any sampling based technique. To circumvent such draw back, this dissertation adopts a potential (navigation) function approach. Although a sampling-based planner may offer travel distance optimal paths—which a potential field controller cannot guarantee—on-line trajectory adaptation imposes stringent constraints on the computational power mobile platforms should carry.

The time-varying nature of the workspace presents unique challenges to potential function based controllers too. Existing work has treated instances of moving

obstacles, particularly in cases where the “obstacles” are simultaneously deployed sensor platforms [20, 42, 67]. When moving entities are all controllable, this problem reduces to an instance of a (bigger) time invariant one. Avoiding collisions with both static and moving objects within a navigation function framework, however, needs to be treated with extreme care, because one of the basic working assumptions of the original methodology of [36] no longer holds: obstacles are no longer guaranteed to be some  $\epsilon$  apart. This issue is not addressed here; instead, the novelty of the navigation function approach used in this dissertation is in its ability to handle moving destinations with provable convergence guarantees.

#### 1.4.4 Source Seeking with Limited Information

Multiple sensory and mapping technologies, such as target localization, environment mapping, as well as self localization, are needed to carry out a radiation detection task in a complex environment. However some prerequisites for the application of these technologies may not be in place, due to limitations in robots’ sensing and computation capacity. It is then necessary to study possible options when some of the above mentioned assumptions no longer hold.

Studies on wifi [30], sound [1], radio [69, 72] signal strength-based mapping and source seeking have been shown promising for source seeking with limited information. A wheeled robot subject to unicycle kinematic constraints can converge to the extremum of a signal field by tuning its forward and turning velocity either deterministically [77] or stochastically [40, 41], solely relying on sampling such signal field without global localization. A general class of robot dynamics can perform source seeking tasks using stochastic approximation techniques [5]. However, these results usually only hold in obstacle free space. This dissertation performs a preliminary study on the possibility of extending such source seeking methods to cluttered environments by allowing robots to recover from collisions with some probability. This added collision recovery behavior extends a single continuous source seeking system into a hybrid one, that consists of both a continuous flow space as the robot navigates in the free space, as well as discrete

events that capture collisions. This type of hybrid system with random events is often referred to as a Stochastic Hybrid System (**SHS**). One particular interesting aspect of this problem is to find out the probability of reaching certain set while avoiding some other set in the workspace. Such reachability problem is studied in [11], where the flow dynamics is deterministic while the jumps are stochastic. Extension to systems with stochastic flow dynamics have been made [10, 12]. Further studies aim at maximizing the probability of reaching specified subsets through optimal control of a **SHS** by discretization and dynamic programming over limited time horizon [33, 62, 63]. However, the computation cost associated with solving the reachability and optimization problem for a **SHS** is quite high. In this dissertation, a method for bounding the reachability probability for source seeking in cluttered environments is presented, which shall serve as a first step in theoretically analyzing source seeking problems with wall collisions events.

## 1.5 Problem Statement

This dissertation focus on solving the following problem: find the optimal way to improve radiation detection methods, by exploiting sensor mobility.

The radiation detection process is closely tied to the distances between the sensors and the potential target due to the square distance attenuation of perceived source radiation strength, which leads to the first problem solved in this dissertation: what is the direct relation between sensor mobility and the radiation detection performance?

The answer to this problem given in Chapter 3 leads to a following question: given that some particular radiation detection performance measures can be computed as functions of sensor trajectories, what would be the optimal sensor trajectories that maximize detection performance with guaranteed bound on false alarm rate?

Once this optimal control problem is solved, a motion planner and robot controllers need to be designed to implement such optimal strategy on actual robots moving in physical world. A solution to motion planning in clustered environments while pursuing time-varying target set is given in Chapter 4 and the controllers are developed in

Chapter 5 to guarantee the robots with different dynamics can converge to the smooth trajectories given by the motion planner.

Lastly, assume that the robot of interest cannot locate themselves perfectly while in pursuit of their targets but are capable of recovering from collisions with obstacles in the environment with some probability, then a question arise as what would be the performance bounds on the chance of successfully converging to some signal field's extremum in cluttered environments for such robot. This question is investigated in Chapter 8. The conclusions drawn are to serve as first step in radiation detection using robots with only basic sensors, such as encoders, an Inertial Measurement Unit (IMU) and radiation counters.

## 1.6 Scientific Contributions

This dissertation addresses challenges in radioactive source detection that relate to minimizing error probabilities through sensor mobility and navigating in cluttered environments while tracking a time-varying target.

Existing literature on radiation detection usually utilizes static sensors and follows Bayesian approach to detecting and estimating target states including position, velocity as well as acceleration. This dissertation will reveal that using static sensors, tracking a weak mobile radioactive source is unrealistic due to low signal noise ratio and limited time window, which motivates us to take a different approach by focusing on detecting the nature of the target and estimate target trajectory through other means such as visual tracking.

Existing work on radiation detection using mobile sensors does not reveal the relation between the sensor motion and error probabilities directly. Their focus is more on exploring the workspace and locating static radioactive sources while our focus is on deciding the nature of the target given target's location. In this dissertation, the optimal sensor motion is obtained, which minimizes Chernoff bounds on detection error probabilities directly.

In terms of navigating mobile sensors, the fundamental challenge here is to work with time-varying targets. Sampling-based methods may not be able to re-plan fast enough to provide convergence guarantees to a mobile target. This dissertation shows that a modification to a navigation function-based controller can make it converge to time-varying target.

It has been shown that with local sensor readings and velocity feedback, a robot with limited sensing capacity can still converge to the extremum of the field in open space [40, 41, 77]. However, introducing obstacles completely changes the system dynamics. This dissertation proposes a new model that captures the uncertainty in occasional collisions and studies the success rate of the robot converging to field extremum while considering collisions with obstacles.

This dissertation starts with formulating and solving an optimization problem to obtain sensor trajectories that minimize an upper bound on the Probability of missed detection ( $P_M$ ) while constraining the Probability of false alarm ( $P_{FA}$ ) below a given constant  $\alpha \in (0, 1)$ . Based on the analytic solution of the aforementioned optimal control problem, a modified navigation function-based motion planner is proposed, which steers mobile sensors inside cluttered environment. Low-level controllers are designed to ensure that robots—in the experimental studies conducted here, these would be a quadrotor and a wheeled mobile robot—can converge to the reference trajectory given by the motion planner. Preliminary studies are initiated on the lower bounds on the probability of reaching signal extremum for mobile robots that are reasonably resilient to collisions using only local signal readings.

This dissertation includes material from [50], in which I contributed to the work of finding tightest Chernoff bounds, likelihood ratio test threshold selection, sensor management optimization and the simulation and experimental validation of the benefits of sensor mobility.

## Chapter 2

### TECHNICAL PRELIMINARIES

The first step towards solving a radiation detection problem is to make a decision on the validity of the two hypotheses: either the target is benign or radioactive; this corresponds to two Poisson processes with different intensity signatures. If the target is benign, the sensors are essentially recording background radiation, the mean intensity of which is assumed known. On the other hand, if the (moving) target is indeed radioactive, the sensors are expected to observe a Poisson process with time varying intensity. The observed Poisson process is a composition of the background radiation, and the radiation counts from the radioactive source, whose intensity suffers square distance attenuation between sensor and source. Because both the sensors and the source can be moving during the detection period, the observed Poisson process's intensity will also change accordingly.

Now assume that a set of measurements  $N_t(i)$  at each sensor is collected. To decide which hypothesis is true, a [LRT](#) is optimal [7] in the sense that compared to any other tests, it achieves the lowest probability of errors. The [LRT](#) is based on the idea of using the ratio between the likelihood of getting the given sensor measurements under the two hypotheses as the criterion for making a decision. If the ratio is above a carefully chosen threshold, then the hypothesis on the numerator is in favor, otherwise, the denominator one is decided.

This chapter provides the mathematical preliminaries on modeling radiation measurement process and making decisions between hypotheses using [LRT](#). Background information and essential assumptions made in this dissertation on formulating optimal control problems and navigating amongst obstacles are presented as well.

## 2.1 Radiation Sensor Model

The gamma ray reception process at the radiation counter side when the distance between sensor and source is time-varying can be described mathematically by a inhomogeneous Poisson process.

**Definition 2.1.1** *Suppose  $\lambda(t)$  is a nonnegative, measurable function such that  $\int_0^t \lambda(s) ds < \infty$  for all  $t > 0$ . A point process  $N_t$  on a probability space  $(\Omega, \mathcal{F}, \mathbb{P})$  adapted to the filtration  $(\mathcal{F}_t : t > 0)$  is said to be a  $(\mathbb{P}, \mathcal{F}_t)$ -Poisson process with intensity  $\lambda(t)$  if for  $0 \leq s \leq t$ ,*

1.  $N_t - N_s$  is independent of  $\mathcal{F}_s$ , and
2.  $N_t - N_s$  is a Poisson random variable with parameter  $\int_s^t \lambda(u) du$ , i.e. for all  $n \in \mathbb{Z}^+$ ,

$$\mathbb{P}(N_t - N_s = n) = e^{-\int_s^t \lambda(\tau) d\tau} \frac{(\int_s^t \lambda(\tau) d\tau)^n}{n!} .$$

To define this process in a radiation detection setting, first let  $(\Omega, \mathcal{F})$  be a measurable space, supporting a  $k$ -dimensional vector of counting processes  $\mathbf{N}_t = (N_t(1), \dots, N_t(k))$ ,  $t \in [0, T]$ . For our problem,  $N_t(i)$  represents the number of counts registered at sensor  $i \in \{1, 2, \dots, k\}$  up to (and including) time  $t \in [0, T]$ . These measurements are typically assumed to be independent from each other, with an exception of [66]. The two hypotheses  $H_0$  and  $H_1$  regarding the nature of the target correspond to two distinct probability measures on  $(\Omega, \mathcal{F})$ . Hypothesis  $H_0$  corresponds to a probability measure  $\mathbb{P}_0$ , with respect to which  $N_t(i)$ ,  $1 \leq i \leq k$ , are independent Poisson processes over  $t \in [0, T]$  with background radiation intensities  $\beta_i(t)$ , respectively. Hypothesis  $H_1$  corresponds to a probability measure  $\mathbb{P}_1$ , with respect to which the  $N_t(i)$ ,  $1 \leq i \leq k$ , are independent Poisson processes over  $t \in [0, T]$  with the sum of background and target induced radiation intensities  $\beta_i(t) + \nu_i(t)$ , respectively. The decision problem is thus one of identifying the correct probability measure ( $\mathbb{P}_0$  versus  $\mathbb{P}_1$ ) on  $(\Omega, \mathcal{F})$ , based on a realization of the  $k$ -dimensional process  $\mathbf{N}_t = (N_t(1), \dots, N_t(k))$ . The following requirements are imposed on  $\beta_i$  and  $\nu_i$ .

**Assumption 2.1.2** For  $1 \leq i \leq k$ ,  $\beta_i : [0, T] \rightarrow [\beta_{\min}, \beta_{\max}]$  is a bounded, continuous function with  $0 < \beta_{\min} < \beta_{\max} < \infty$ ,  $\beta_{\min}, \beta_{\max}$  independent of  $i \in \{1, 2, \dots, k\}$ .

**Assumption 2.1.3** For  $1 \leq i \leq k$ ,  $\nu_i : [0, T] \rightarrow [\nu_{\min}, \nu_{\max}]$  is a bounded, continuous function with  $0 < \nu_{\min} < \nu_{\max} < \infty$ ,  $\nu_{\min}, \nu_{\max}$  independent of  $i \in \{1, 2, \dots, k\}$ .

Let  $(\mathcal{F}_t^{\mathbf{N}} : 0 \leq t \leq T)$  be the filtration generated by the process  $\mathbf{N}_t$ .<sup>1</sup> Then, for any event  $A \in \mathcal{F}_t^{\mathbf{N}}$ , an observer of the sample path  $s \mapsto \mathbf{N}_s$ ,  $0 \leq s \leq t$ , knows at time  $t$  whether or not the event  $A$  has occurred. The  $\sigma$ -field  $\mathcal{F}_T^{\mathbf{N}}$  thus represents the information generated by the totality of sensor observations up to  $t = T$ ; to wit, the information on which the decision must be based.

## 2.2 Decision Making

The process of deciding whether an object is radioactive or not can be formulated as a hypotheses testing problem. Hypotheses 0: object is not radioactive and  $\lambda = \beta$ ; Hypotheses 1: object is radioactive and  $\lambda = \beta + \nu$ . According to Neyman-Pearson Lemma, a **LRT** is the optimal method for deciding between two hypotheses [7]. A test for deciding between hypotheses  $H_0$  and  $H_1$  on the basis of  $\mathcal{F}_T^{\mathbf{N}}$  observations can be thought of as a set  $A_1 \in \mathcal{F}_T^{\mathbf{N}}$  with the following significance: if the outcome  $\omega \in A_1$ ,  $H_1$  is decided; if  $\omega \in A_0 \triangleq \Omega \setminus A_1$ ,  $H_0$  is decided. For a test  $A_1 \in \mathcal{F}_T^{\mathbf{N}}$ , two types of errors might occur. A type I error, “false alarm”, occurs when the outcome  $\omega \in A_1$  (i.e.  $H_1$  is decided) while  $H_0$  is the correct hypothesis. A type II error, “miss”, occurs when  $\omega \in \Omega \setminus A_1$  (i.e.  $H_0$  is decided) while  $H_1$  is the correct hypothesis. The probability of false alarm is given by  $\mathbb{P}_0(A_1)$ , while the probability of a miss is given by  $\mathbb{P}_1(\Omega \setminus A_1)$ . Then, the probability of detection is given by  $\mathbb{P}_1(A_1) = 1 - \mathbb{P}_1(\Omega \setminus A_1)$ .

In the Neyman-Pearson framework, one is given an acceptable upper bound on the probability of false alarm  $\alpha \in (0, 1)$ , and the problem is to find an optimal test: a set  $A_1^* \in \mathcal{F}_T^{\mathbf{N}}$  which maximizes the probability of detection over all tests whose

---

<sup>1</sup> Thus, for  $t \in [0, T]$ ,  $\mathcal{F}_t^{\mathbf{N}} = \sigma(\mathbf{N}_s : 0 \leq s \leq t)$  is the smallest  $\sigma$ -field on  $\Omega$  with respect to which all the ( $k$ -dimensional) random variables  $\mathbf{N}_s$ ,  $0 \leq s \leq t$ , are measurable.

probability of false alarm is less than or equal to  $\alpha$ . The following result describes the optimal test. The underlying probabilistic setup is as described above.

**Theorem 2.2.1** ([49]) *Consider a network with  $k$  sensors and a fusion center connected in a parallel configuration.<sup>2</sup> For  $1 \leq i \leq k$ , let  $N_t(i)$ ,  $t \in [0, T]$  denote the observation at sensor  $i$  over the time interval  $[0, T]$  and let  $(\tau_n(i) : n \geq 1)$  be the jump times of  $N_t(i)$ . Assume that at decision time  $T$ , sensor  $i$  transmits to the fusion center the statistic*

$$L_T(i) \triangleq \exp \left( - \int_0^T \nu_i(s) ds \right) \prod_{n=1}^{N_T(i)} \left( 1 + \frac{\nu_i(\tau_n(i))}{\beta_i(\tau_n(i))} \right)$$

*computed on the basis of its observation  $t \mapsto N_t(i)$ ,  $t \in [0, T]$ . Then, the test  $A_1^* = \{L_T \geq \gamma\}$  performed at the fusion center, with  $L_T \triangleq \prod_{i=1}^k L_T(i)$  and  $\gamma > 0$  satisfying  $\mathbb{P}_0(L_T \geq \gamma) = \alpha$ , is optimal for  $\mathcal{F}_T^N$ -observations in the sense that for any  $A_1 \in \mathcal{F}_T^N$  with  $\mathbb{P}_0(A_1) \leq \alpha$ , we have  $\mathbb{P}_1(A_1^*) \geq \mathbb{P}_1(A_1)$ .*

### 2.3 Chernoff Bounds on Error Probabilities of Likelihood Ratio Test

The performance of the test  $\{L_T \geq \gamma\}$  can be measured by the probabilities of false alarm and miss defined by

$$P_{FA} \triangleq \mathbb{P}_0(L_T \geq \gamma) \quad \text{and} \quad P_M \triangleq \mathbb{P}_1(L_T < \gamma) \quad , \quad (2.1)$$

respectively. In many cases of interest, however, the exact computation of these error probabilities is mathematically intractable, motivating the need for good upper bounds which are easily computable. Theorem 2.3.1, stated below, derives such bounds on  $P_{FA}$  and  $P_M$  using Chernoff's inequalities.

For  $p \in \mathbb{R}$ , it is defined:

$$\Lambda(p) \triangleq \log \mathbb{E}_0[L_T^p] = \log \mathbb{E}_0[e^{p \ell_T}] \quad , \quad (2.2)$$

---

<sup>2</sup> Each sensor can only communicate with a central unit called the fusion center; see [70].

where  $\ell_T \triangleq \log L_T$  is the log likelihood ratio, and  $\mathbb{E}_i$  denotes expectation with respect to probability measure  $\mathbb{P}_i$ ,  $i \in \{0, 1\}$ . The term  $\Lambda(p)$  is thus the *cumulant generating function* of  $\ell_T$  under  $H_0$ . Also let

$$\mu_i(t) \triangleq 1 + \frac{\nu_i(t)}{\beta_i(t)} \quad (2.3)$$

for  $1 \leq i \leq k$ ,  $t \in [0, T]$ ; thus,  $\mu_i(t)$  is the ratio of intensities for  $H_1$  versus  $H_0$ . The intensities at sensor  $i$  at time  $t$  under  $H_0$  and  $H_1$  can now be written as  $\beta_i(t)$ , and  $\mu_i(t)\beta_i(t)$ , respectively.

**Theorem 2.3.1** ([50]) *Let  $\eta \triangleq \log \gamma \in \mathbb{R}$ . The Chernoff bounds on  $P_{FA}$  and  $P_M$  are given by*

$$P_{FA} \leq \exp \left( \inf_{p>0} [\Lambda(p) - p\eta] \right) , \quad (2.4a)$$

$$P_M \leq \exp \left( \inf_{p<1} [\Lambda(p) + (1-p)\eta] \right) , \quad (2.4b)$$

where for  $p \in \mathbb{R}$ ,  $\Lambda(p)$  is explicitly computable via

$$\Lambda(p) = \sum_{i=1}^k \int_0^T [\mu_i(s)^p - p\mu_i(s) + p - 1] \beta_i(s) ds . \quad (2.5)$$

Note that the explicit analytic formula for  $\Lambda(p)$  in (2.5) is a consequence of the assumption of deterministic intensities, which allows us to circumvent the intricate filtering analysis in [31] needed to accommodate stochastic intensities.

## 2.4 Optimal Control

This dissertation will formulate an optimization problem that aims at minimizing the Chernoff bounds on the error probabilities when deciding whether the target is radioactive or not. In general, an optimal control problem consists three parts: the state dynamics, the cost function associated with the states and control inputs, and the constraints on the states and control inputs.

Assume the state dynamics can be described by Ordinary Differential Equations (ODEs):

$$\dot{x} = f(t, x, u) , \quad x(t_0) = x_0 ,$$

where  $t$  is time, and  $t_0$  is the initial time. Variable  $x(t) \in \mathbb{R}^n$  is the state,  $u(t) \in U \subset \mathbb{R}^m$  is the control input and  $x_0$  is the initial value for the state.

The optimal control problem aims at minimizing a cost functional with respect to  $u$  in the form of:

$$J(u) = \int_{t_0}^{t_f} L(t, x, u) dt + K(t_f, x_f) ,$$

where  $L$  and  $K$  are given functions typically referred to as running, and terminal cost respectively. The time period  $[t_0, t_f]$  can either be fixed or free to change.

The constraints may include the upper or lower bounds on the states and control inputs, and it may also be in the integral form:

$$C(u) = \int_{t_0}^{t_f} M(t, x, u) dt = C_0 ,$$

where  $C_0$  is a constant value and  $M$  is a given function of  $(t, x, u)$ .

For the radiation detection problem at hand, due to the limitation on the detection time window, this dissertation aims at optimizing detection performance over a specific bounded time period. Due to the structure of Chernoff bounds on probability of false alarm and miss, the cost function and optimization constraint only involve the running cost term. This type of optimization problem can be approached both numerically and analytically (see Chapter 3).

## 2.5 Motion Planning

To implement the optimal strategy on actual sensor platforms in cluttered environments, a navigation function, which constructs a virtual potential field that guides robot in cluttered environment, can be used to direct robots amongst obstacles. Alternative methods such as Rapidly exploring Random Tree (RRT), Probabilistic Road Map (PRM) are versatile in terms of workspace structure and relatively fast due to the use of sampling. To achieve real-time performance, however, these planners must be tailored with suitable heuristics, which makes performance guarantees difficult to obtain. On the contrary, at the price of limiting the workspace to sphere/star world topologies and sacrificing some optimality, navigation function methods provide smooth

motion plans that can be adapted to different robots dynamics. The explicit feedback based controller offers real-time performance with manageable computation cost.

The motion planner of Chapter 4 follows an artificial potential function approach [36]. Before jumping into the detailed modification on the potential function and the controller design, the environment setup is first introduced here. The workspace for the sensor nodes discussed in this dissertation is defined as a *sphere world*, where the outer boundary of the workspace is a sphere around the origin and all obstacles are spheres completely included in the workspace. These obstacles are sets  $\mathcal{O}_j$ , where  $j \in \{1, \dots, m\}$ , which are assumed to be open balls in the appropriate Euclidean space (here,  $\mathbb{R}^2$  or  $\mathbb{R}^3$ ) having radius  $\rho_j$  and center  $o_j$ . The boundary of obstacle  $j$ , for  $j \in \{1, \dots, m\}$ , is described by means of the function  $\beta_{ij} = \|x_i - o_j\|^2 - \rho_j^2$ , which vanishes on the obstacle’s boundary and is positive in the space surrounding it. Set  $\partial\mathcal{O}_0$  marks the outer workspace boundary, of radius  $\rho_0$ ; this boundary is expressed in the form  $\beta_{i0} = \rho_0^2 - \|x_i\|^2$ , for  $o_0 = 0$ . Then a single scalar function that serves as a metric of proximity to (any) obstacle boundary  $\beta_i = \prod_{j=0}^M \beta_{ij}$  can be defined.

Once the interior of workspace boundary is “punctured” with every obstacle, the *free* workspace  $\mathcal{P} = \mathcal{B}(\rho_0) \setminus \bigcup_{j=1}^m \mathcal{O}_j$  is obtained. Assume that  $\mathcal{O}_j$  for  $j = \{1 \dots m\}$  are isolated, static, sufficiently far away from the target location, and that this target location is sufficiently away from the workspace boundary  $\partial\mathcal{O}_0$ —these four requirements correspond to the collision-free workspace remaining *valid* [36]. It shall be shown in Chapter 4 that using our modified potential function and novel controller, our sensor nodes are able to track this time varying target set in a valid sphere world workspace, at least during the sensors’ integration window.

## 2.6 Vehicle Control

Due to the different kinematics and dynamics that come with different physical robot platforms, lower level controllers are developed to ensure all kinds of robot deployed can track the reference trajectory given by the motion planner. Feedback linearization and backstepping techniques are used to ensure convergence.

Since combining motion planning with realistic robot dynamics in the same feedback loop can be overly complicated, it may be more practical to find a reference trajectory first, and then develop a local controller that would track such a reference. In this dissertation, the motion planner of choice is based on potential function, and gives a reference velocity field that guides a single integrator point robot through a cluttered environment to a moving target set. However real robot dynamics are typically of higher order and nonlinear, requiring special treatment. The particular robot dynamics discussed in this dissertation include those of wheeled robots and quadrotors.

Through output feedback linearization, (with horizontal position being the output) the sensor mounted on a wheeled robot can be treated as a single integrator, which naturally fits the robot into our potential function based motion planning framework. The treatment for a quadrotor is a bit more complex [45]. Yet that system too can be controlled as a double integrator through inverse dynamics combined with backstepping techniques [35,37]. This approach enables the development of a controller for the quadrotor that ensures the robot's converge to the reference velocity commands as well as the target set. The controller design is detailed in Chapter 5.

## 2.7 Extremum Seeking

If the amount of prior information given is limited, and assume that no map nor global localization methods are available, the extremum seeking techniques for navigation should still be applicable. With single sensor and local readings, a robot can follow an average path converging to min/max points of signal field by randomly perturbing itself. Using a group of robots, better estimates of the gradient of the field can be obtained through accurate formation control and localization in local frames.

A wheeled robot can converge to the extremum of the signal field without global localization [77]. This approach employed periodic perturbation on the forward velocity of a wheeled robot that rotates at constant angular velocity. The periodically perturbed forward velocity includes a tunable bias term that is appropriately combined with

extremum seeking to produce a net effect of drifting towards the source:

$$v = cJ \sin(\omega t) + \alpha \omega \cos(\omega t) . \quad (2.6)$$

This velocity controller uses measurements of the signal field  $J$  at the robot's location to execute extremum seeking. Provided that  $\omega$  in (2.6) is more than three times the angular velocity of the wheeled robot, the local convergence of such controller is proved via averaging. Instead of perturbing the forward velocity deterministically as above, a stochastic version of similar extremum seeking controller has also been constructed [41]. One limitation in these methods is that the controller's convergence is only guaranteed in open space. In case collisions are not always fatal to the robot, this dissertation studies the probability bound of convergence for such extremum seeking controller in the presence of obstacles.

## 2.8 Stochastic Hybrid System Modeling

When employing such randomized controller without localization or environment information, modeling the randomness in robot's dynamics as well as handling inevitable collisions are challenging.

To account for non-deterministic behavior in both robot's motion in free space—i.e., the stochastic perturbation in the forward velocity—and during collision events, a mathematical framework that can incorporate both continuous and discrete stochastic behavior is needed. The continuous flow of the robot can be modeled using Stochastic Differential Equations (SDEs); the reachability problem of SDE is studied [10, 12, 57] under different settings.

Collisions can be modeled based on a discrete time discrete state Markov process [27]. Let  $\{X_0, X_1, \dots\}$  be a sequence of random variables which take values in some countable set  $\mathcal{S}$ , called state space. A Markov process enjoys the Markov property:

$$P(X_n = s | X_0, X_1, X_{n-1}) = P(X_n = s | X_{n-1}) ,$$

for all  $n \geq 1$  and  $s \in \mathcal{S}$ . The problem at hand is to identify the probability of reaching specific state sets, without being absorbed in its complement.

## 2.9 Conclusion

In this chapter, an optimal binary hypotheses testing scheme [LRT](#) is introduced for deciding whether a potential target is radioactive or not. Probability bounds on the chance of making mistakes using this [LRT](#) is also presented, which can be utilized to formulate the optimization problem solved in [Chapter 3](#). The environmental configuration *sphere world* is introduced to clarify the workspace model used in this dissertation, which would be revisited in [Chapter 4](#). Preliminary evidence are provided on robot converging to signal field extremum, which validates the study based on Markov process in [Chapter 8](#).

## Chapter 3

### OPTIMAL STRATEGIES FOR RADIATION DETECTION

The first key aspect in using a team of mobile sensors to decide the radioactive nature of a mobile target is to determine the criterion for making such decision. As discussed in Chapter 2, an [LRT](#) provides optimal performance when making binary decisions about the radioactivity nature of a target. Yet the threshold in the [LRT](#) cannot be obtained analytically due to the intricate nature of the inhomogeneous Poisson processes involved. However the probability of the test arriving at erroneous conclusions can be bounded, which can help determining the sub-optimal threshold to use. Knowing that the underline Poisson process is influenced by the trajectories of the sensors, one can treat these bounds as functions of sensor trajectories.

This dependency between the test's performance bounds and the sensor trajectories can be used as a basis for an optimal control problem, which aims at minimizing the bounds on error probabilities through a choice of sensor trajectories. This optimal control problem can be solved numerically, or even analytically depending on the dynamics model assumed for the mobile sensors. Numerical solution to this optimization problem can be obtained using General Pseudospectral Optimal Control Software ([GPOPS](#)), a general purpose MATLAB software package specialized to nonlinear optimal control problems. The software uses a class of variable-order Gaussian quadrature methods, that approximates the continuous-time optimal control problem as a sparse Non-linear Programming ([NLP](#)) by expressing continuous functions as polynomials [6, 24–26, 54]. The numerical results provide insight into the solutions of the optimal control problem analytically, which is approached using necessary conditions for optimality with the optimal control problem posed within the framework of Pontryagin's Maximum Principle.

This chapter first provides a threshold selection method for LRT based on Chernoff bounds and then formulates an optimal control problem linking the sensor trajectories with the detection performance. First an example optimal control problem is solved numerically, and then a more general case is solved analytically under assumptions on the simplified vehicle dynamics, using the intuition gained from the numerical solution. The analytic solution provides us a guideline as how to improve detection performance using sensor mobility.

### 3.1 Problem Statement

Given the LRT described in Theorem 2.2.1, find a suitable threshold  $\gamma$  that ensures the probability of false alarm  $P_{FA} = \mathbb{P}_0(L_T \geq \gamma) \leq \alpha$  for a given  $\alpha \in (0, 1)$ . Assume the sensors (radiation counters) are controllable and their trajectories subject to  $\dot{x}_i = f(t, x_i, u_i)$ , for  $i \in \{1, \dots, k\}$ , search for optimal  $u_i^*$  that minimizes the Chernoff bounds (2.4b) on  $P_M = \mathbb{P}_1(L_T < \gamma)$ .

### 3.2 Threshold Selection for Radiation Detection

Imagine a mobile vehicle which could be carrying a radioactive point source of activity  $a$ . The trajectory of this target is denoted  $x_t(t) \in \mathbb{R}^3$ , assuming that  $\|\dot{x}_t\| \leq V_t$  for  $t \in [0, T]$ . In the specific setting considered in this dissertation, the target is to be classified as non-radioactive or radioactive within a time period of  $T$  seconds using a collection of  $k$  mobile sensors (radiation counters). The motion of the radiation sensors is controllable, and the trajectory of sensor  $i$  for  $i \in \{1, \dots, k\}$  is denoted  $x_i(t) \in \mathbb{R}^3$ .

This dissertation assumes that the source intensity is comparable to background. The background radiation intensity at the location of sensor  $i$  is denoted  $b_i > 0$  and will be considered constant, which is valid so long as the spatial variations and detection task duration  $T$  are relatively small during the detection process.

Although background intensity can be assumed constant, the *perceived* source intensity by sensor  $i$  changes with the distance between the source and sensor  $i$ . Specifically, the closer the sensor is to the source, the more radiation from the source it is

likely to detect. If, for the sake of simplicity, sensors are assumed identical having a cross section coefficient  $\chi$ , then it is generally accepted [46] that the mean count rate  $\nu_i$  measured by sensor  $i$  follows an inverse square law with respect to the distance between sensor and source. This inverse square relationship is adopted as the sensor model in this dissertation:

$$\nu_i \triangleq \frac{\chi^a}{2\chi + \|x_i - x_t\|^2} . \quad (3.1)$$

Thus, when  $\|x_i - x_t\| = 0$ , the source is touching the surface of the sensor, and the latter measures exactly half of source's emitted rays. With the perceived radiation sensor model  $\nu$  and background radiation level  $b_i$  defined, mathematical tools described in Sections 2.1, 2.2, and 2.3 can be utilized to establish a likelihood ratio test for deciding whether the mobile target is radioactive or not.

Theorem 2.2.1 describes an **LRT** which is optimal when making binary hypotheses testing, namely for deciding whether the source is radioactive or not. By performing the described **LRT**, the minimum  $P_M$  can be achieved while  $P_{FA}$  is constrained. However, the threshold value  $\gamma$  needs to be decided first to perform the test. To determine the threshold  $\gamma$  used in **LRT**, the equation  $P_{FA} = P_0(L_T > \gamma) = \alpha$  needs to be solved for  $\gamma$ . Then  $P_M$  can be used to evaluate how well the test is in detecting radioactive sources. However obtaining the closed form of these error probabilities is mathematically intractable and a performance measure for the **LRT** can be obtained by using upper bounds on error probabilities Theorem 2.3.1 [50].

As shown in Theorem 2.3.1,  $P_{FA}$  and  $P_M$  are upper bounded by functionals of both  $\mu_i$  and a scalar parameter  $p$ . With some algebraic manipulation on (2.4a), for any given scalar  $p > 0$ ,

$$P_{FA} \leq \exp \left( \inf_{p>0} \left[ \sum_{i=1}^k \int_0^T [\mu_i(s)^p - p\mu_i(s) + p - 1] \beta_i(s) ds - p \log \gamma \right] \right) .$$

To achieve the infimum, the first and second order derivatives of the right hand side are taken with respect to  $p$ . At the point  $p^*$  where the expression attains its minimum, the

first order derivative should be zero and the second order derivative should be positive:

$$\sum_{i=1}^k \int_0^T \left[ \mu_i(s)^{p^*} \log \mu_i(s) - \mu_i(s) + 1 \right] \beta_i(s) ds - \log \gamma = 0 \quad (3.2)$$

$$\sum_{i=1}^k \int_0^T \left[ \mu_i(s)^{p^*} (\log \mu_i(s))^2 \right] \beta_i(s) ds > 0 . \quad (3.3)$$

The inequality in (3.3) is satisfied for any value  $p^* \in (0, 1)$ . (3.2) offers a equality constraint governing  $p^*$  and the threshold  $\gamma$  used in the LRT.

In practice, it is normally required that  $P_{FA}$  must be bounded by a constant value  $\alpha > 0$ . This constant  $\alpha$  is taken to be very small, because if the detection system produces too many false alarms, the user will tend to ignore it. To understand the need for this constraint on  $P_{FA}$ , consider the following illustrative problem: assume the real probability of the target being radioactive is  $P_R$  (usually a small number reflecting our expectation that there is little chance of nuclear contamination under normal conditions.), when the likelihood ratio is greater than the chosen threshold, what is the chance that the source is indeed radioactive? The answer is

$$\frac{P_R(1 - P_M)}{(1 - P_R)P_{FA} + P_R(1 - P_M)} = \frac{1 - P_M}{1 - P_M + (\frac{1}{P_R} - 1)P_{FA}} .$$

Now that to have a reasonable large chance of accurate detection,  $P_{FA}$  must be at least comparable to  $P_R$ , otherwise the denominator is dominated by the value of  $P_{FA}/P_R$ .

Now to enforce  $P_{FA} < \alpha$ , take (2.4) and substitute  $\gamma$  from (3.2) to obtain:

$$\begin{aligned} P_{FA} &\leq \exp \left( \left[ \sum_{i=1}^k \int_0^T \left[ \mu_i(s)^{p^*} - p^* \mu_i(s) + p^* - 1 \right] \beta_i(s) ds - p^* \log \gamma \right] \right) \\ &= \exp \left( \left[ \sum_{i=1}^k \int_0^T \left[ \mu_i(s)^{p^*} - p^* \mu_i(s)^{p^*} \log \mu_i(s) - 1 \right] \beta_i(s) ds \right] \right) = \alpha . \quad (3.4) \end{aligned}$$

Equations (3.2) and (3.4) together can be used for computing the right threshold  $\gamma$  for LRT as well as the parameter  $p^*$  for the Chernoff bounds of Theorem 2.3.1.

Now recall that from (2.4b),  $p^*$  needs to be less than 1, to ensure the bound on  $P_M$  is less than one. With  $p^* < 1$  as an additional constraint, there may not be

a solution to (3.2) and (3.4). This signifies that the available measurements, given sensor trajectories, and target trajectory, do not give enough information to make a valid decision on whether target is radioactive or not, under the false alarm constraint. When there is no valid threshold for a given false alarm constraint and detection setup, one may consider one or more of the following alternatives, including optimize sensor trajectories, increase the number of sensors used, extend the detection period and relax the false alarm constraint. Among these options, optimizing sensor trajectories can be performed without extra burden on the detection task and thus this is the direction chosen in this dissertation, while all other options will either increase the cost of the radiation detection system by adding sensors or affect the performance of the system by relaxing the constraint on time and accuracy.

### 3.3 Minimize Error Bounds by Optimal Control

#### 3.3.1 Optimization Problem Formulation

An optimization problem is defined by the cost and constraints functions. In this case the constraint is that  $P_{FA} < \alpha$ . The cost will be defined to be the Chernoff bound on  $P_M$ , a value closely tied to the false alarm rate and a natural performance metric candidate for assessing how successful the radiation detection task is. Assuming that the measurement statistic is sufficient to satisfy the false alarm constraint, investigation into the bound on  $P_M$  starts by taking (2.4b), substituting  $\gamma$  by  $p^*$  as given in (3.2), and incorporating the false alarm constraint (3.4):

$$\begin{aligned}
P_M &\leq \exp \left( \sum_{i=1}^k \int_0^T [\mu_i(s)^p - p\mu_i(s) + p - 1] \beta_i(s) ds + (1 - p) \log \gamma \right) \\
&= \exp \left( \sum_{i=1}^k \int_0^T [\mu_i(s)^p - p\mu_i(s)^p \log \mu_i(s) - 1 + \mu_i(s)^p \log \mu_i(s) - \mu_i(s) + 1] \beta_i(s) ds \right) \\
&= \exp \left( \sum_{i=1}^k \int_0^T [\mu_i(s)^p + (1 - p)\mu_i(s)^p \log \mu_i(s) - \mu_i(s)] \beta_i(s) ds \right)
\end{aligned}$$

$$= \alpha \exp \left( \sum_{i=1}^k \int_0^T [\mu_i(s)^p \log \mu_i(s) - \mu_i(s) + 1] \beta_i(s) ds \right) .$$

Now to perform a test on a mobile source, multiple mobile sensors are deployed to collect radiation counts for a limited period of time  $T$  and the likelihood ratio is computed as stated in the Theorem 2.2.1 using  $\mu_i$  as defined in (2.3) as a function of  $\nu_i$ , which is in turn function of sensor poses as suggested by (3.1). This chain of reasoning establishes the connection between the trajectories of sensors and the test's statistic. Similar reasoning applies to Theorem 2.3.1, showing that the probability bounds on  $P_{FA}$  and  $P_M$  are also functions of the sensors' poses. To formally reveal the dependency between the bounds on  $P_{FA}$ ,  $P_M$  and sensor trajectory  $x_i$ , the governing equation for  $x_i$  needs to be introduced first, which in general can be stated as ODE.

Assume that the trajectory  $x_i$  of sensor  $i$  is controlled through input  $u_i(t)$  as in

$$\dot{x}_i = f(x_i, u_i) , \quad (3.5)$$

where the function  $f(\cdot)$  is Lipschitz continuous. Also assume that constraints are imposed on control actuation in the form  $\|u_i\| \leq u_{\max}$  for some constant  $u_{\max}$ . All sensor motion control inputs are collected in a stack vector  $\mathbf{u} = (u_1, \dots, u_{k_s})$ . Recall (3.1), and note that since  $x_i$  is implicitly determined by  $u_i$ , and  $\nu_i$  is a function of  $x_i$ ,  $\nu_i$  is a functional operating on  $u_i$ ; we thus write  $\nu_i(u_i)$ , or more generally  $\nu_i(\mathbf{u})$ .

Following (2.3), and treating  $\nu_i$  as function of  $\mathbf{u}$ , we write:

$$\mu_i(\mathbf{u}) \triangleq 1 + \frac{\nu_i(\mathbf{u})}{b_i} . \quad (3.6)$$

Now it is apparent that the logarithm of an upper bound on the probability of miss  $P_M$  for the network of sensors is analytically expressed as

$$J_{PM}(\mathbf{u}, p) \triangleq \sum_{i=1}^{k_s} \int_0^T [\mu_i(\mathbf{u})^p + (1-p)\mu_i(\mathbf{u})^p \log \mu_i(\mathbf{u}) - \mu_i(\mathbf{u})] b_i ds , \quad (3.7)$$

while the probability of false alarm is upper bounded by a constant  $\alpha \in (0, 1)$ , i.e.  $P_{FA} \leq \alpha$ , if

$$F_{FA}(\mathbf{u}, p) \triangleq \sum_{i=1}^{k_s} \int_0^T [p\mu_i(\mathbf{u})^p \log \mu_i(\mathbf{u}) - \mu_i(\mathbf{u})^p + 1] b_i ds = -\log \alpha . \quad (3.8)$$

The equation (3.7) is also rewritten by plugging in the equality constraint (3.8):

$$J_{\text{PM}}(\mathbf{u}, p) \triangleq \log \alpha + \sum_{i=1}^{k_s} \int_0^T [\mu_i(\mathbf{u})^p \log \mu_i(\mathbf{u}) - \mu_i(\mathbf{u}) + 1] b_i \, ds . \quad (3.9)$$

It is therefore natural to formulate an optimal control problem where  $J_{\text{PM}}$  is the cost to be optimized with respect to  $\mathbf{u}$  and  $p$  under constraint (3.8)—with  $\log \alpha$  as a constant. In this problem, the state of the dynamical system is  $\boldsymbol{\mu} \triangleq (\mu_1, \dots, \mu_{k_s})$ , implicitly determined by  $\mathbf{u}$  in (3.6) via (3.1) and (3.5).

### 3.3.2 Numerical Determination of Optimal Sensor Trajectories

Optimal control theory is expected to suggest how sensor mobility can be exploited. However a first look at the optimal control problem (3.9)-(3.8) reveals that both the cost and constraint are integrals of highly complex nonlinear functions. To gain some insight, a specific problem is first solved numerically. This section is from [50] and the sensor model used in this section is in accordance with the one used in [50].

Consider an example where  $k_s = 5$  sensors are available, and sensors 1 and 5 are mobile. The five sensors are originally at locations  $(x_1, y_1) = (-3, 0)$ ,  $(x_2, y_2) = (-1, 0)$ ,  $(x_3, y_3) = (0, 0)$ ,  $(x_4, y_4) = (1, 0)$ ,  $(x_5, y_5) = (3, 0)$ . Set  $\mathbf{x} = (x_1, y_1, x_2, y_2, \dots, x_5, y_5)^\top$ , with  $(x_1(t), y_1(t))$ ,  $(x_5(t), y_5(t))$  evolving according to

$$\begin{aligned} \ddot{x}_1 &= u_1 \quad , \quad \ddot{y}_1 = u_2 \\ \ddot{x}_5 &= u_3 \quad , \quad \ddot{y}_5 = u_4 \end{aligned} \quad (3.10)$$

with initial conditions  $(x_1(0), y_1(0)) = (-3, 0)$ ,  $(x_5(0), y_5(0)) = (3, 0)$ , and  $\mathbf{u} = (u_1, \dots, u_4)^\top$ , which are the accelerations of sensors in x and y directions. Further assume that the velocity and control inputs of the mobile sensors are subject to the constraints

$$|\dot{x}_i| \leq 1 \quad , \quad |\dot{y}_i| \leq 1 \quad , \quad |u_i| \leq 5 \quad . \quad (3.11)$$

This set of constraints on sensor dynamics enforce the bounded control assumption raised in previous section and imposes velocity limit on sensor as well since sensors can not move arbitrarily fast.

The target now follows a circular trajectory of radius  $R = 0.5$  m centered at the point  $(0, 2)$ , with maximum velocity  $v_s^{\max} = 1.26$  m/s and maximum acceleration  $a_s^{\max} = 3.16$  m/s<sup>2</sup>:

$$x_s(t) = 0.5 \cos\left(\frac{4\pi t}{5}\right) \quad , \quad y_s(t) = 2 + 0.5 \sin\left(\frac{4\pi t}{5}\right) \quad . \quad (3.12)$$

To emphasize the effectiveness of mobility in improving decision accuracy in this example, the source intensity is reduced to be less than the background radiation level even when observed at zero distance. Assume that the target is indeed a source of radiation with activity  $a = 480$  counts per minute (cpm), while background is at a level of  $\beta = 780$  cpm. It is required that a decision on source's radioactivity should be made based on the sensor measurements within 10 seconds.

The optimal control laws  $\mathbf{u}$  are numerically computed using the **GPOPS** software. Figure 3.1 presents the closed-loop paths for the mobile sensors 1 and 5 under the direction of the optimal control  $\mathbf{u}$ . Under the optimal control input  $\mathbf{u}$ , sensors 1 and 5 move so as to minimize their instantaneous distance from the target, but due to their velocity bounds they cannot follow exactly the target's circular path, which can also be seen in Figure 3.2, that shows the history of the horizontal speeds of sensor 1 and the target (the source). While the sensor's speed is confined in the  $[-1, 1]$  interval, the target's speed periodically exceeds that limit, forcing the sensor to cut its circular reference path trying to keep up with the faster source. With sensors 1 and 5 chasing the target along paths generated by the optimal control  $\mathbf{u}^*$ , the optimal value for the optimization cost turns out to be

$$J_{PM}^* = -2.07 \quad ,$$

with the probability of false alarm being constrained to remain below<sup>1</sup>  $\alpha = 10^{-3}$ . This amounts to having  $\eta(\mathbf{u}^*) = -2.07$ , yielding an upper bound on the probability of missed detection of  $1.26 \times 10^{-4} = \exp(J_{PM}^*) \times \alpha$ .

---

<sup>1</sup> Approximate current nuisance alarm rate at U.S. border crossings is reported as  $10^{-4}$  [76].

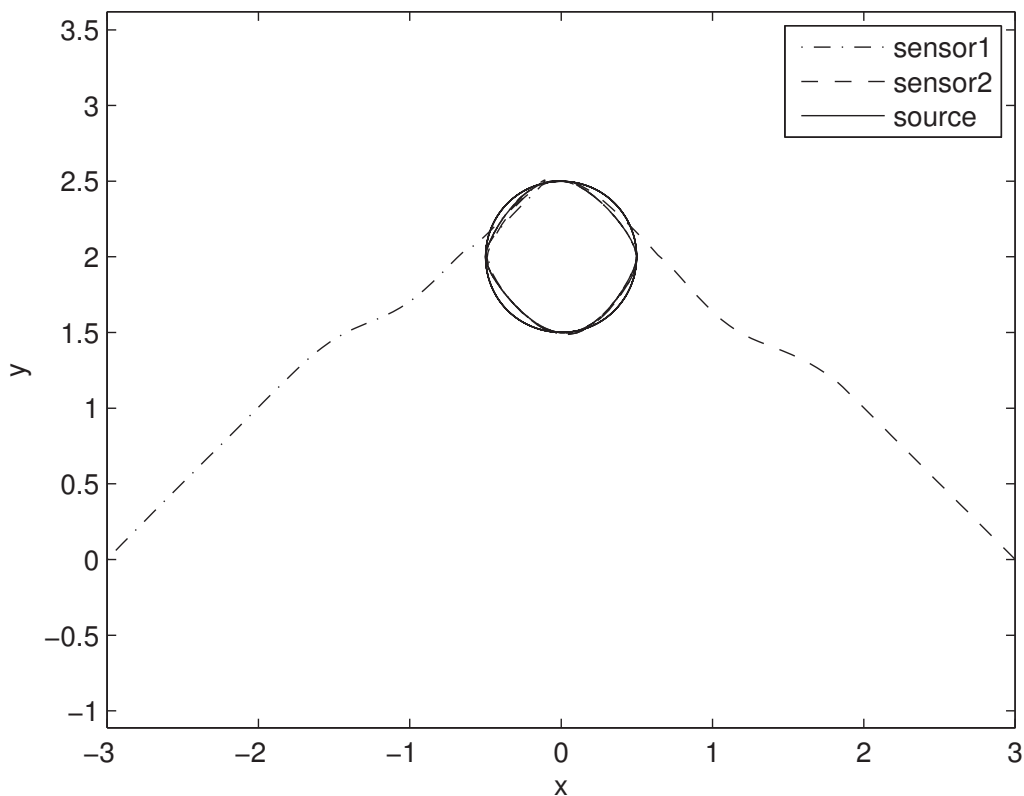


**Figure 3.1:** Source path and optimal paths for mobile sensors 1 and 5. The source is circling at a radius of 0.5 around point (0,2), and is approached by sensor 1 from the left, and sensor 5 from the right. The two sensors cannot keep up with the source due to their motion constraints, so they “cut” the source’s circular path along rounded inscribed rectangles.

In this scenario, the sensors’ controlled mobility offered an order of magnitude improvement in their **SNR**. The **SNR** is computed using the expression  $\frac{S}{\sqrt{S+B}}$ , where  $S$  denotes the (estimated) integrated source count rate, and  $B$  is the integrated background count rate [47]. Had all sensors remained stationary during the 10 second time window, the **SNR** for detectors 1, . . . , 5 would have been 0.4980, 1.1434, 1.3617, 1.1434, and 0.4980, respectively. With sensors 1 and 5 chasing the target, they improve their **SNR** from 0.4980 to 4.6843.

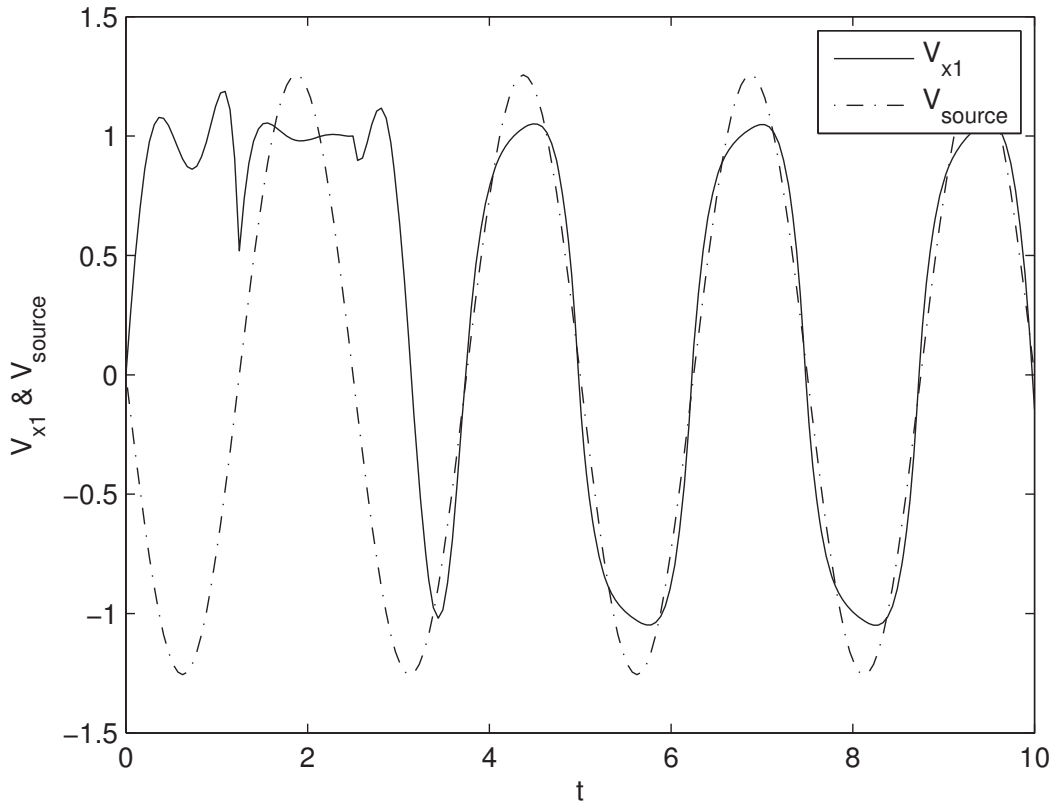


**Figure 3.2:** Horizontal velocity of target (source) and sensor 1 over time. The sensor’s absolute speed is upper bounded by 1, while the target’s periodically exceeds that bound. The sensor cannot track the motion of the faster source perfectly.

Not surprisingly, the optimal solution to the sensor trajectories verifies our original hypotheses: it is beneficial to have sensors moving close to the target for as long as possible during the detection period. Still, this needs to be formally proven.

### 3.3.3 Analytic Determination of Optimal Sensor Trajectories

For simplicity, assume that the position trajectory of sensor  $i$  is controlled through input  $u_i(t)$  as in

$$\dot{x}_i = u_i . \tag{3.13}$$

and that the constraints on control actuation are of the form  $\|u_i\| \leq u_{\max}$  for some constant  $u_{\max} > V_t = \max_{t \in [0, t]} \|x_t(t)\|$ . Collect all sensor motion control inputs in a stack vector  $\mathbf{u} = (u_1, \dots, u_{k_s})$ .

In this problem, the state of the dynamical system is  $\boldsymbol{\mu} \triangleq (\mu_1, \dots, \mu_{k_s})$ , implicitly determined by  $\mathbf{u}$  in (3.6) via (3.1) and (3.13); specifically,

$$\dot{\mu}_i = \frac{2\chi_i a(x_t - x_i)}{b_i(2\chi_i + \|x_t - x_i\|^2)^2} (u_i - \dot{x}_t) . \quad (3.14)$$

The path to an analytic solution starts with transforming the constrained optimal control problem (3.7)–(3.8) into an unconstrained one. The first partial result establishes the monotonicity of functional  $F_{FA}$  in (3.8) with respect to the positive parameter  $p$ .

**Lemma 3.3.1** *Fix  $\mathbf{u}$ .  $F_{FA}$  is strictly increasing with  $p$ .*

**Proof** Write  $\frac{\partial F_{FA}}{\partial p} = \sum_{i=1}^{k_s} \int_0^T p \mu_i^p (\log \mu_i)^2 b_i dt$ , and note that it is strictly positive since  $\mu_i > 1, p \in (0, 1)$ . ■

**Lemma 3.3.2** *Fix  $p$ .  $F_{FA}$  is strictly increasing with positive needle perturbations on  $\mu_i$ .*

**Proof** Consider first a needle perturbation of the form  $\epsilon \delta(t - t_1)$  on coordinate  $i$  of  $\boldsymbol{\mu}$ , yielding a perturbed  $\tilde{\boldsymbol{\mu}}$  with component  $\mu_i(t) + \epsilon \delta(t - t_1)$ ; here,  $\delta(t - t_1)$  is the Dirac function offset at  $t_1$  and  $\epsilon > 0$  a small parameter. The Taylor expansion on the integrand of  $F_{FA}(\boldsymbol{\mu}, p)$  shows that

$$F_{FA}(\tilde{\boldsymbol{\mu}}, p) \approx F_{FA}(\boldsymbol{\mu}, p) + b_i \epsilon p^2 \mu_i(t_1)^{p-1} \log \mu_i(t_1) ,$$

Notice that the perturbed  $F_{FA}$  is strictly increasing with respect to the perturbation  $\epsilon$  in the control  $\mu_i$  at time  $t_1$  with  $\delta(t - t_1)$  duration given  $p^2 \mu_i(t_1)^{p-1} \log \mu_i(t_1) > 0$ . ■

Apply the Maximum Principle and extract the optimal motion coordination strategy for each sensor:

**Proposition 3.3.3** *The solution for sensor  $i \in \{1, \dots, k_s\}$  to the optimal control problem (3.7)–(3.8)–(3.14) within the feasible set  $\mathcal{U} = \{\mathbf{u} \in \mathbb{R}^{3k_s} : \|\mathbf{u}_i\| \leq u_{\max}\}$  is*

$$u_i = \begin{cases} \frac{x_t - x_i}{\|x_t - x_i\|} u_{\max} & x_i \neq x_t \\ \dot{x}_t & x_i = x_t \end{cases} .$$

**Proof** Given (3.7)–(3.8), the cost function is:

$$J_{\text{PM}} = \sum_{i=1}^{k_s} \int_0^T [\mu_i^p + (1-p)\mu_i^p \log \mu_i - \mu_i] b_i \, ds .$$

Since  $J_{\text{PM}}$  is always finite, by Fubini's theorem,

$$J_{\text{PM}} = \int_0^T \sum_{i=1}^{k_s} [\mu_i^p + (1-p)\mu_i^p \log \mu_i - \mu_i] b_i \, ds ,$$

To find the necessary condition for optimal control policy, the unconstrained problem is first solved, that is to minimize  $J_{\text{PM}}$  without considering the constraint (3.8). In order to do so, start with the following Lagrangian:

$$L = \sum_{i=1}^{k_s} [\mu_i^p + (1-p)\mu_i^p \log \mu_i - \mu_i] b_i . \quad (3.15)$$

Here the states of optimization problem are  $\mu_i$ 's whereas  $p \in (0, 1)$  is a constant.

Now the Hamiltonian can be represented as

$$H = \sum_{i=1}^{k_s} \lambda_i \dot{\mu}_i(u_i) - \sum_{i=1}^{k_s} [\mu_i^p + (1-p)\mu_i^p \log \mu_i(s) - \mu_i(s)] b_i , \quad (3.16)$$

and dynamics of the costates  $\lambda_i$ 's, which correspond to  $\mu_i$ 's, are written as

$$\dot{\lambda}_i = -\frac{\partial H}{\partial \mu_i} = \left[ (1-p)p\mu_i^{p-1} \log \mu_i + \mu_i^{p-1} - 1 \right] b_i .$$

To solve for the optimal costate  $\lambda_i$ , the sign of the  $\dot{\lambda}_i$  and  $\lambda_i$  are analyzed first. Knowing that  $b_i > 0$ , the sign of the terms within the square bracket, denoted  $I_{\text{PM}}(p, \mu_i)$ , determines the sign of  $\dot{\lambda}_i$ :

$$I_{\text{PM}}(p, \mu_i) \triangleq (1-p)p\mu_i^{p-1} \log \mu_i + \mu_i^{p-1} - 1 .$$

Notice that  $I_{PM}(p, 1) = 0$  for any  $p \in (0, 1)$ , and it is monotonically decreasing with respect to  $\mu_i$ :

$$\begin{aligned}\frac{\partial I_{PM}}{\partial \mu_i} &= -(1-p)^2 p \mu_i^{p-2} \log \mu_i + (1-p) p \mu_i^{p-2} + (p-1) \mu_i^{p-2} \\ &= -\mu^{p-2} (1-p)^2 (p \log \mu_i + 1) < 0 .\end{aligned}$$

It can now be concluded that  $I_{PM}(\mu_i) < 0$  for  $\mu_i > 1$ . Thus it is guaranteed that  $\dot{\lambda}_i < 0$  for any  $\mu_i > 1, p \in (0, 1)$ .

Now since  $\mu_i^*(T)$  can take any value in  $(1, 1 + \frac{a}{2b_i}]$ , there are two mutually exclusive and exhaustive cases: either  $\mu_i^*(T) \in (1, 1 + \frac{a}{2b_i})$ , or  $\mu_i^*(T) = \mu_{i_{max}} = 1 + \frac{a}{2b_i}$ . If  $\mu_i^*(T) \in (1, 1 + \frac{a}{2b_i})$ , the transversality condition requires  $\lambda_i(T) = 0$ . Thus, given  $\dot{\lambda}_i < 0$ , it is  $\lambda_i(t) > 0 \quad \forall t \in (0, T]$ . In light of this, and given (3.14), the Hamiltonian maximization condition  $H(\boldsymbol{\mu}^*, \mathbf{u}^*, \boldsymbol{\lambda}^*) = \max_{\mathbf{u} \in \mathcal{U}} H(\boldsymbol{\mu}^*, \mathbf{u}^*, \boldsymbol{\lambda}^*)$  applied on (3.16) requires that

$$u_i^* = \frac{x_t - x_i}{\|x_t - x_i\|} u_{\max} , \quad (3.17)$$

that is, it suggests the maximal control effort to close the distance between sensor and source as close as possible. Using such a controller, eventually (given big enough  $T$ ) it will be  $\mu_i^*(T) = \mu_{i_{max}}$ . At this point, the second case is in effect. Denote  $T_s$  the switching time. Now  $t \in [T_s, T]$  with boundary condition  $\mu_i(T_s) = \mu_i(T) = \mu_{i_{max}}$  and  $\left. \frac{\partial J_{PM}}{\partial \mu_i} \right|_t = \dot{\lambda}_i(t) < 0$ . To minimize  $J_{PM}$  when  $t \in [T_s, T]$ ,  $\mu_i$  should once again be kept at its maximum value.

Since the unconstrained optimal control strategy is always at least as good as of the constrained optimal strategy, proving that the unconstrained strategy is equivalent to the constrained strategy can be done by showing that the constrained optimal strategy is also at least as good as the unconstrained strategy, which shall be true if unconstrained optimal strategy  $u^*$  always satisfies the constraint when the constraint is feasible.

Given that the  $F_{FA}(\boldsymbol{\mu}, p)$  is monotonically increasing with respect to  $p$  and  $F_{FA}(\boldsymbol{\mu}, 0) = 0$ , it can be asserted that for  $\boldsymbol{\mu}^*$ , one can always find a  $p$  that satisfies

the constraint (3.8) if  $F_{FA}(\boldsymbol{\mu}^*, 1) \geq -\log \alpha$ . On the other hand, for cases that  $F_{FA}(\boldsymbol{\mu}^*, 1) < -\log \alpha$ , the unconstrained optimal trajectory  $\boldsymbol{\mu}^*$  would fail to satisfy the constraint, and this is because the constraint is infeasible for any control inputs in the feasible set  $\mathcal{U}$ , which is proven by the following reasoning:

According to Lemma 3.3.2,  $F_{FA}$  is monotonically increasing with respect to perturbations in  $\boldsymbol{\mu}$ . Given that following the proposed optimal trajectory  $\boldsymbol{\mu}^*$  derived from unconstrained case, the maximum possible value of  $\boldsymbol{\mu}$  over time is already obtained. So  $F_{FA}(\boldsymbol{\mu}^*, 1)$  already reaches the maximum possible value over all possible trajectories of  $\boldsymbol{\mu}$ . Thus if  $F_{FA}(\boldsymbol{\mu}^*, 1)$  is still less than  $-\log \alpha$ , the constraint  $F_{FA}(\boldsymbol{\mu}^*(\mathbf{u}^*), p^*) = -\log \alpha$  is infeasible for  $\mathbf{u}^* \in \mathcal{U}$  and  $p \in (0, 1)$ . ■

Essentially what Proposition 3.3.3 dictates is for the sensor platforms to close the gap between themselves and the suspected target as fast as possible.

### 3.4 Conclusion

This chapter has laid out the complete procedure one would need to follow to decide whether a mobile target is radioactive or not. How the LRT is connected to sensor trajectories is shown, and the Chernoff bound on probability of miss is minimized while constraining the probability of false alarm by optimizing sensor trajectories using both numerical optimization and analytic proofs under sensor dynamics constraints. Here is a summary of the methodology introduced in this chapter and used throughout this dissertation for radiation detection using mobile sensor networks.

#### Radiation detection procedure outline:

1. Drive the mobile sensors adhere to the optimal control guidance  $\mathbf{u}^*$ , that is to catch up with the target and keep a close distance for as long as possible;
2. Collect radiation counts and the time at which the counts are received at each sensor. Record the trajectories of each sensor and the target at the fusion center;
3. Compute the partial likelihood ratio  $L_T(i)$  defined in Theorem 2.2.1 at each sensor;

4. Collect all  $L_T(i)$  from all sensors and get the total likelihood ratio  $L_T = \prod_{i=1}^k L_T(i)$  at fusion center;
5. Compute the threshold for the **LRT** at fusion center using (3.2) and (3.4) where  $\mu_i$  are computed based on the trajectories of sensors and target;
6. Compare likelihood ratio  $L_T$  to threshold, and if  $L_T$  is higher than the threshold, conclude that the target is radioactive. Otherwise, declare the target benign.

In the next Chapter 4 and Chapter 5, the implementation of the this radiation detection procedure in physical world will be discussed.

## Chapter 4

### ROBOT NAVIGATION

Chapter 3 provided a complete procedure summarized in Section 3.4 to decide whether a moving target is radioactive. However, it should be pointed out that the control strategy obtained by solving the optimal control problem (3.7)–(3.8)–(3.14) is still under the assumption of an ideal world where the robot’s dynamics is simplified to single integrator and spatial constraints of the workspace are omitted.

Limiting the feasible workspace positions that sensors can attain augments the set of constraints in the optimal control problem formulation of Chapter 3. In the general case, the resulting optimal control problem may not admit analytic solutions. Even if treated numerically, the solver may fail to provide reasonable results as these constraints could be highly nonlinear and ill conditioned at the boundary. For example,  $\log(x)$  or  $1/x$  are often used as barrier functions to prevent solution crossing the obstacle boundaries. Yet, their values and derivatives all tend to infinity when  $x$  approaches zero, which makes it difficult for an optimization solver to converge to a solution. These considerations motivate an alternative, albeit sub-optimal, approach to sensor management, which—while adhering to the same strategy introduced by solving the optimal radiation detection problem—is likely to trade-off some performance for safety and analytically established convergence properties.

Given that our goal is to move the sensor towards the target as fast as possible while avoiding collisions, a well-chosen motion planner that suits this purpose needs to be formulated. One option could be optimal sampling based controller represented by PRM\* and RRT\*. However, these methods rely on relatively large amounts of computation, especially so when online path modification or re-generation is required, which is necessary when the goal is moving. Real time performance could be challenging

considering the limitation on the onboard computation power that a mobile robot can offer. Even though these methods provides asymptotically optimality, in real time application, there would always be a compromise between the computation cost and path optimality.

On the other hand, this dissertation decides to take a different approach. Using the insight obtained from the unconstrained case, a sensor management strategy is developed for navigation amongst obstacles in the context of navigation functions. The sensor platforms are not allowed to physically touch and collide with their target; they are to keep a minimum safe distance  $r_t$  away from it. The destination for the sensors thus becomes a *set*, the surface of a sphere centered at the moving target. Instead of running at full speed toward the target, sensors will now perform steepest descent over a smooth artificial landscape in which obstacles are regions of high elevation and the target sits surrounded by an area of depression. This approach—while adhering to the same principle of closing the distance as quickly as possible—is likely to trade-off some performance for safety and analytically established convergence properties. Yet this path planner is able to provide analytic feedback controller that provides smooth trajectory towards the moving target while avoiding obstacles. This chapter shall show how to construct such controller, why the controller is applicable to real robot and why it guarantees obstacle avoidance.

#### 4.1 Problem Statement

Let the trajectory of sensor  $i$ , denote  $x_i \in \mathbb{R}^n$ ,  $n \in \{2, 3\}$ , be governed by the single integrator model:  $\dot{x}_i = u_i$ ,  $u_i \in \mathbb{R}^n$ . In a *sphere world* introduced in Section 2.5, find a controller  $u_i$  that guarantees the sensor  $i$  converge to a set  $\|x_i - x_t(t)\| = r_t$ , where  $x_t(t)$  is a smooth time varying trajectory in  $\mathbb{R}^n$ , from almost everywhere in the *sphere world*.

## 4.2 Navigation Function Construction

For sensor  $i$  at position  $x_i$ , the goal function that the potential field attempts to minimize takes the form

$$J_i(x_i, t) = (\|x_i - x_t(t)\|^2 - r_t^2)^2 .$$

It can be shown that  $J_i$  has two distinct sets of critical points, one isolated point at  $x_t$  which is a local maximum, and a manifold of local minima on the boundary of the sphere  $\mathcal{B}_{x_t}(r_t)$  defined by  $\|x_i - x_t(t)\|^2 - r_t^2 = 0$ . Define  $\mathcal{B}_{x_t}(\delta_t)$  as a (small) ball around  $x_t$  with radius  $0 < \delta_t < r_t$ . It shall be shown later that as long as initial conditions are  $r_t$  away from  $x_t$ , the stated controller provides convergence to  $\partial\mathcal{B}_{x_t}(r_t)$ .

So far the sensors have been treated as point masses (negligible volume); the possibility of them colliding with each other is therefore ignored and steering them away from environment obstacles is the main focus of the motion planner design.

With obstacle function  $\beta$  introduced in Section 2.5 and the objective function  $J$  defined above, the following navigation function is constructed with tuning constant  $k > 0$ :

$$\varphi_i(x_i, x_t) = \frac{J_i(x_i, x_t)}{(J_i(x_i, x_t)^k + \beta_i(x_i))^{1/k}} . \quad (4.1)$$

The next section shows that using this potential function, a feedback controller can be constructed to drive any robot with single integrator dynamics to our moving goal set.

## 4.3 Navigation Function Controller: Convergence

The proposed controller can drive a single integrator robot to the time varying set from within workspace except starting inside the zero measure attraction region of saddles.

**Theorem 4.3.1** *Given that the workspace is  $\mathcal{P}$  valid, for any  $x_t$ , there exists a positive value  $N(x_t)$  such that for every  $k \geq N(x_t)$ , the function*

$$\varphi_i(x_i, x_t) = \frac{J_i(x_i, x_t)}{(J_i(x_i, x_t)^k + \beta_i(x_i))^{1/k}} \quad (4.2)$$

is such that all critical points other than those in  $\partial\mathcal{B}_{x_t}(r_t)$  are either nondegenerate with attraction regions of measure zero or in  $\mathcal{B}_{x_t}(\delta_t)$ , and the gradient field generated by  $\nabla_{x_i}\varphi_i$  has  $\partial\mathcal{B}_{x_t}(r_t)$  as the only limit set with non-zero measure attraction region outside  $\mathcal{B}_{x_t}(\delta_t)$ .

**Proof** The fact that outside  $\mathcal{B}_{x_t}(\delta_t)$ ,  $\varphi_i$  has only local minima on target set  $\partial\mathcal{B}_{x_t}(r_t)$ , and that all other critical points are non-degenerate (saddle) with measure zero attraction, is established through the series of Propositions A.0.1 through A.0.7 stated and proven in the Appendix. ■

There are some practical considerations related with the application of a bang-bang controller like (3.17) within a constrained environment, especially when it is undesirable for sensor platforms to collide with their target at maximum speed. Even when the system's manifold of attractors is set at a safe distance  $r_t$  away from the target, flowing along the direction of the negated gradient of (4.2) at full speed is certain to result in overshoot and oscillatory behavior in the neighborhood of the attracting set. The sensors' approach to this goal set needs to be fast but gradual. For these reasons, given Theorem 4.3.1, a relaxation on (3.17) for implementation in constrained environments in the following form is proposed

$$u_i^\circ = -c \frac{\nabla_{x_i}\varphi_i}{\|\nabla_{x_i}\varphi_i\| + \xi} - (\nabla_{x_t}\varphi_i^\top \dot{x}_t) \frac{\nabla_{x_i}\varphi_i}{\|\nabla_{x_i}\varphi_i\|^2}, \quad (4.3)$$

for some constants  $c < u_{\max}$ , and  $\xi > 0$ .

**Theorem 4.3.2** *The closed loop system (3.13)–(4.3) converges to the set  $\{x_i \in \mathbb{R}^3 : J_i(x_i, x_t) = 0\}$ , from almost everywhere in  $\{x_i \in \mathbb{R}^3 : \beta_i(x_i) > 0, x_i \notin \mathcal{B}_{x_t}(r_t), \|x_i\| < \rho_0\}$  given that in (4.2),  $k > \sup_{x_t} N(x_t)$ , where supremum is taken over all possible values of  $x_t$ .*

**Proof** The closed loop system is time-varying due to  $x_t(t)$ . The proof is thus based on Barbalat's lemma using function  $\varphi_i$ . The aim is to show that  $\lim_{t \rightarrow \infty} \dot{\varphi}_i = 0$ .

First note that  $\varphi_i \geq 0$ . Then expand  $\dot{\varphi}_i$  and plug (4.3) to verify that

$$\dot{\varphi}_i = -c \frac{\|\nabla_{x_i} \varphi_i\|^2}{\|\nabla_{x_i} \varphi_i\| + \xi} \leq 0 . \quad (4.4)$$

So  $\lim_{t \rightarrow \infty} \varphi_i$  exists and bounded. Thus according to Barbalat's lemma, proving that  $\lim_{t \rightarrow \infty} \dot{\varphi}_i = 0$  reduces to showing that  $\dot{\varphi}_i$  is uniformly continuous in  $t$ , which can be ensured if  $\ddot{\varphi}_i$  is bounded. Toward this end note that

$$\ddot{\varphi}_i = -c \frac{\xi + \frac{1}{2} \|\nabla_{x_i} \varphi_i\|}{(\|\nabla_{x_i} \varphi_i\| + \xi)^2} \frac{d\|\nabla_{x_i} \varphi_i\|^2}{dt} ,$$

and is bounded if  $\frac{d\|\nabla_{x_i} \varphi_i\|^2}{dt}$  is. Indeed,

$$\begin{aligned} \frac{d\|\nabla_{x_i} \varphi_i\|^2}{dt} = & -2 \frac{\nabla_{x_i} \varphi_i^\top \nabla_{x_i}^2 \varphi_i \nabla_{x_i} \varphi_i}{\|\nabla_{x_i} \varphi_i\| + \xi} - 2 \frac{\nabla_{x_t} \varphi_i^\top \dot{x}_t}{\|\nabla_{x_i} \varphi_i\|^2} \nabla_{x_i} \varphi_i^\top \nabla_{x_i}^2 \varphi_i \nabla_{x_i} \varphi_i \\ & + 2 \nabla_{x_i} \varphi_i^\top \nabla_{x_i} (\nabla_{x_t} \varphi_i) \dot{x}_t . \end{aligned}$$

With  $\varphi_i$  being a smooth function, its first and second partial derivatives are bounded on the compact subset of  $\mathbb{R}^3$  where  $\beta_i \geq 0$ . The second term does not explode because the expression  $\left| \frac{\nabla_{x_i} \varphi_i^\top [\nabla_{x_i}^2 \varphi_i] \nabla_{x_i} \varphi_i}{\|\nabla_{x_i} \varphi_i\|^2} \right|$  admits an upper bound equal to the maximum eigenvalue of the Hessian of  $\varphi_i$ —which is finite. Therefore, since  $\|\dot{x}_t\| < V_t$ ,  $\frac{d\|\nabla_{x_i} \varphi_i\|^2}{dt}$  is bounded, and  $\dot{\varphi}_i$  is uniformly continuous, it follows that  $\lim_{t \rightarrow \infty} \dot{\varphi}_i = 0$ . Then (4.4) implies that  $\lim_{t \rightarrow \infty} \|\nabla_{x_i} \varphi_i\| = 0$ , which in turns suggests—based on Theorem 4.3.1 and  $k > \sup_{x_t} N(x_t)$ —that with time  $x_i \rightarrow \{x \in \mathbb{R}^3 : J_i(x, x_t) = 0\}$  from almost all initial conditions in  $\{x_i \in \mathbb{R}^3 : \beta_i(x_i) > 0, x_i \notin \mathcal{B}_{x_t}(r_t), \|x_i\| < \rho_0\}$ , notice that as long as  $x_i(0) \notin \mathcal{B}_{x_t(0)}(r_t)$ , it will always be  $x_i(t) \notin \mathcal{B}_{x_t(t)}(r_t)$  due to  $\dot{\varphi} \leq 0$  and  $\varphi$  reaches minimum at  $\partial \mathcal{B}_{x_t(t)}(r_t)$ . Since the workspace is valid,  $\sup_{x_t} N(x_t)$  is always finite. ■

#### 4.4 Navigation Function Controller: Boundedness

The navigation function controller is proved to be bounded when the robot is away from unstable critical points. Control law (4.3) is essentially a modulated (negated) gradient following tracking controller with a feedforward to compensate for target motion. It can be shown that if  $\sup_{t \geq 0} \|\dot{x}_t(t)\|$  is sufficiently small compared to

$u_{\max}$ , then  $(c, \xi, \epsilon)$  can be always be chosen so that both (a)  $\|u_i^\circ\| \leq u_{\max}$  for all positions that  $\beta_i(x_i) > 0$  except for a small region around saddle points, and (b) (gradual) convergence to the surface of the ball of radius  $r_t$  around the target is analytically established. The former claim on the boundedness of (4.3), relates to lower bounding  $\|\nabla_{x_i}\varphi_i\|$  which appears in the denominator of the second term. This term vanishes as  $x_i$  approaches one of the critical points of  $\varphi_i$ . For a properly tuned navigation function, those critical points can be expected to be in a set  $\bigcup_{j=0}^m \{x_i | \beta_{ij}(x_i) < \epsilon\} \cup \partial\mathcal{B}_{x_t}(r_t) \cup \mathcal{B}_{x_t}(\delta_t)$ . Notice that the critical point in  $B_{x_t}(\delta_t)$  is not reachable from outside  $B_{x_t}(r_t)$  since the robot would converge to  $\partial B_{x_t}(r_t)$  before reaching into  $B_{x_t}(\delta_t)$ . Under reasonable assumptions<sup>1</sup> the magnitude of the control input is proved to be upper bounded.

**Lemma 4.4.1** *For  $x_i$  sufficiently far from unstable critical points,  $u_i^\circ$  is bounded.*

**Proof** Bound  $\|u_i^\circ\|$  as

$$\begin{aligned}
\|u_i^\circ\| &= \left\| -c \frac{\nabla_{x_i}\varphi_i}{\|\nabla_{x_i}\varphi_i\| + \xi} - (\nabla_{x_t}\varphi_i^T \dot{x}_t) \frac{\nabla_{x_i}\varphi_i}{\|\nabla_{x_i}\varphi_i\|^2} \right\| \\
&\leq c \left\| \frac{\nabla_{x_i}\varphi_i}{\|\nabla_{x_i}\varphi_i\| + \xi} \right\| + |\nabla_{x_t}\varphi_i^T \dot{x}_t| \left\| \frac{\nabla_{x_i}\varphi_i}{\|\nabla_{x_i}\varphi_i\|^2} \right\| \\
&< c + \frac{\|\nabla_{x_t}\varphi_i\|}{\|\nabla_{x_i}\varphi_i\|} \|\dot{x}_t\| \\
&= c + \frac{\|k\beta_i \nabla_{x_i} J_i\|}{\|k\beta_i \nabla_{x_i} J_i - J_i \nabla_{x_i} \beta_i\|} \|\dot{x}_t\| \\
&= c + \left( 1 + \frac{\|k\beta_i \nabla_{x_i} J_i\| - \|k\beta_i \nabla_{x_i} J_i - J_i \nabla_{x_i} \beta_i\|}{\|k\beta_i \nabla_{x_i} J_i - J_i \nabla_{x_i} \beta_i\|} \right) \|\dot{x}_t\| \\
&\leq c + \left( 1 + \frac{\|J_i \nabla_{x_i} \beta_i\|}{\|k\beta_i \nabla_{x_i} J_i - J_i \nabla_{x_i} \beta_i\|} \right) \|\dot{x}_t\|.
\end{aligned}$$

The denominator  $\|k\beta_i \nabla_{x_i} J_i - J_i \nabla_{x_i} \beta_i\|$  vanishes at critical points, i.e., unstable critical points and the target set.

---

<sup>1</sup> We need to note, however, that requiring  $x_i$  to be away from saddle points cannot be guaranteed a priori for all initial conditions; there will be a set of initial conditions around the attraction regions of the unstable critical points of  $\varphi_i$  that generate trajectories which cross into  $\{x_i : 1 + \frac{\|J_i \nabla_{x_i} \beta_i\|}{\|k\beta_i \nabla_{x_i} J_i - J_i \nabla_{x_i} \beta_i\|} \geq \frac{u_{\max} - c}{\max\{\|\dot{x}_t\|\}}\}$ .

As  $x_r$  is converging to the target set  $\partial\mathcal{B}_{x_t}(r_t)$ , the upper bound of  $\|u_i^\circ\|$  becomes:

$$\|u_i^\circ\| < c + \left( 1 + \frac{\|\frac{\nabla_{x_i}\beta}{\beta}\|}{\|k\frac{\nabla_{x_i}J_i}{J_i} - \frac{\nabla_{x_i}\beta}{\beta}\|} \right) \|\dot{x}_t\| ,$$

and since, by valid workspace assumption, any point in the target set  $\partial\mathcal{B}_{x_t}(r_t)$  is always at least  $\epsilon_t$  away from obstacles,  $\|\frac{\nabla_{x_i}\beta}{\beta}\|$  is upper bounded. Therefore,

$$\frac{\|\nabla_{x_i}J_i\|}{J_i} = \frac{4\|x_i - x_t\|}{\|x_i - x_t\|^2 - r_t^2} \xrightarrow{x_i \rightarrow \partial\mathcal{B}_{x_t}(r_t)} +\infty ,$$

bounding  $\|u_i^\circ\|$  around the target set and making it converge to  $c + \|\dot{x}_t\|$ .

If now  $x_i$  is close to a unstable critical point, the control input is still bounded by  $u_{max}$  as long as  $x_i$  satisfies

$$x_i \in \left\{ x_i : 1 + \frac{\|J_i \nabla_{x_i} \beta\|}{\|k\beta \nabla_{x_i} J_i - J_i \nabla_{x_i} \beta\|} \leq \frac{u_{max} - c}{\max\{\|\dot{x}_t\|\}} \right\} .$$

The above can be relaxed to

$$\left\{ x_i : \|k\beta \nabla_{x_i} J_i - J_i \nabla_{x_i} \beta\| \geq \frac{\max\{\|\dot{x}_t\|\}}{u_{max} - c - \max\{\|\dot{x}_t\|\}} \sup (J_i \nabla_{x_i} \beta) \right\} ,$$

where the supremum is taken over  $\{x_i : \beta_i(x_i) > 0\}$ . Thus, as long as  $x_i$  stays sufficiently far away from unstable critical points, the control input is bounded.

## 4.5 Conclusion

Equipped with navigation function based motion planner, a point mass sensor can effectively track its intended target using the reference trajectory provided by (4.3). But sensor platforms are not point masses, which leads to the next challenge discussed in Chapter 5: to implement a low level trajectory tracking controller that adapts to different dynamics while ensuring the convergence property of the motion planner.

## Chapter 5

### ROBOTIC PLATFORM INTERFACES

Theorem 4.3.2 establishes the convergence properties of the motion controller for platform dynamics (3.13) in the form of a single integrator. A natural question that arises is what can be said about more complicated sensor platform dynamics. This chapter demonstrates how the control inputs designed for the single integrator case (4.3) can be adapted to different physical sensor platforms. In this dissertation, this is achieved through application of standard nonlinear system analysis techniques, including full state, or output, feedback linearization and backstepping.

In this chapter, the quadrotor model and the wheeled robot model are used to show that with proper controller design, these two types of robot are guaranteed to converge to the reference trajectory given by navigation function based motion planner.

#### 5.1 Problem Statement

The quadrotor's state dynamics is governed by (5.1). The wheeled robot's state dynamics is governed by (5.6). The goal is to design controllers for the quadrotor and the wheeled robot so that the onboard sensor's planar velocity  $(\dot{x}, \dot{y})$  converges to the reference velocity described by  $(\dot{x}_{des}, \dot{y}_{des}) \triangleq u_i^o \in \mathbb{R}^2$ , where  $u_i^o$  is defined in (4.3).

#### 5.2 Quadrotor

##### 5.2.1 Dynamics Model

The quadrotor used in our experiments is an AscTec Hummingbird, which comes with a thrust power controller that takes in unitless numerical commands that range from 0 to 1 representing the power output of the Hummingbird's rotors, with 1 corresponds to maximum rotor speed. Yet the actual force generated is more relevant to

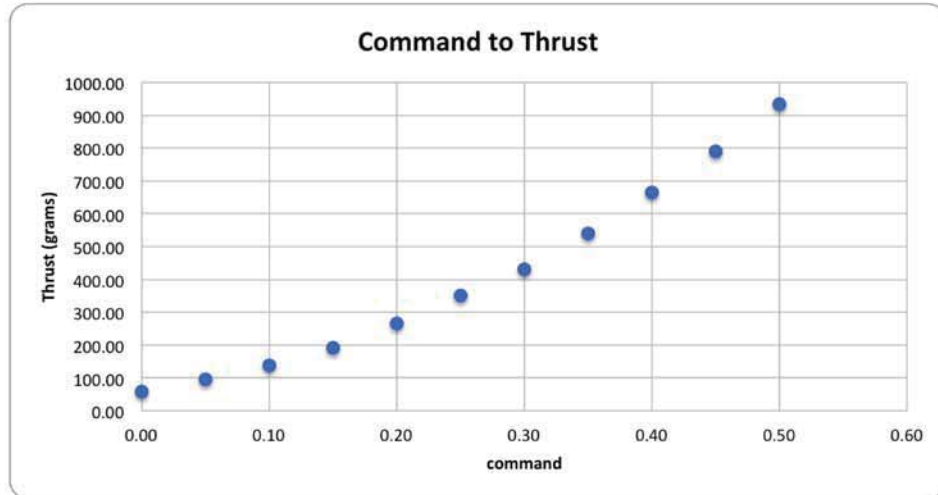


**Figure 5.1:** This command-to-thrust look up chart can be used to determine the unitless command needed to generate desired thrust.

controlling the quadrotor and has to be calibrated. As it turns out, the force supplied by the quadrotor is not quite linearly proportional to the 0 – 1 control commands. A look-up table (Figure 5.1) is created to determine what input should be supplied the thrust power controller so that desired thrust force will be generated. The supplied thrust force is constrained to below 932.3 grams to ensure the quadrotor will not fly too aggressively during the experiment.

The quadrotor is equipped with a manufacturer-provided attitude controller designed to adjust the quadrotor’s rotation along  $Z_b$ ,  $Y_b$ ,  $X_b$  axes using  $Z - Y - X$  Euler angle conversion (Figure 5.2) following the commanded yaw ( $\psi$ ), pitch ( $\theta$ ), roll ( $\phi$ ) angles. This attitude controller is configured to take roll, pitch angles that are smaller than 10 degrees in order to ensure stable and safe flight. When roll, pitch angles are too large, the quadrotor’s propellers may not be able to produce enough lifting force to balance the weight of the quadrotor. In our case, with sensor payload, the quadrotor’s total weight will be around 752 grams, which is slightly less than the 932.3 grams maximum allowable thrust force. So to ensure that the thrust force in the  $Z_w$  direction balances the quadrotor’s weight, the maximum angle between the

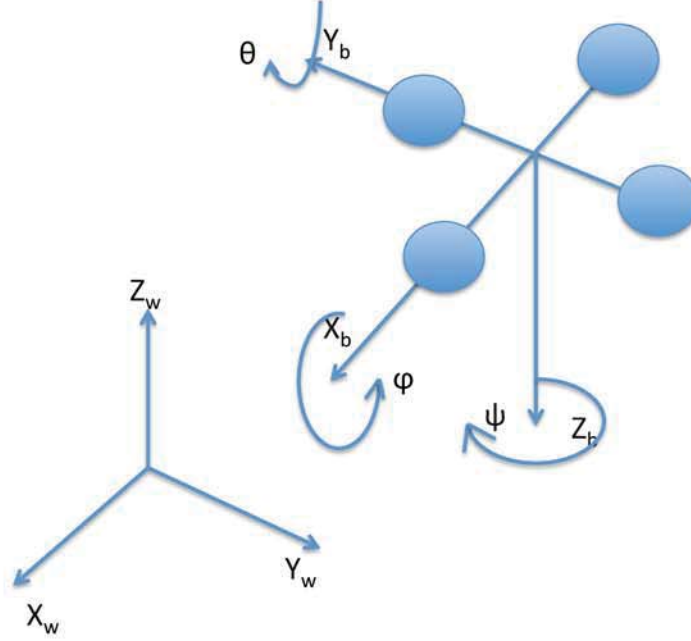


**Figure 5.2:** The coordinates system used by AscTec Hummingbird attitude controller.  $X_b - Y_b - Z_b$  represents the quadrotor's body coordinates with  $X_b$  being the forward direction.  $X_w - Y_w - Z_w$  represents the world coordinates with  $Z_w$  being upward direction. The quadrotor's rotation is represented by rotating the quadrotor by  $\psi, \theta, \phi$  along axes in the order of  $Z_b, Y_b, X_b$ .

quadrotor's body frame and the horizontal plane should be  $\cos^{-1}(752/932.3) \approx 36.2^\circ$ . Consider the battery voltage drop effect on the thrust force during flight, and allowing for some safety margin, the  $10^\circ$  limit on roll, pitch angles is not too conservative.

Let  $(x, y, z)$  denote the quadrotor's position in the world coordinates. The quadrotor's dynamics can be written as:

$$m \begin{bmatrix} \ddot{x} \\ \ddot{y} \\ \ddot{z} \end{bmatrix} = R \begin{bmatrix} 0 \\ 0 \\ F \end{bmatrix} + \begin{bmatrix} 0 \\ 0 \\ -mg \end{bmatrix} \quad (5.1)$$

where  $R$  is the rotation matrix represented by  $\phi, \theta, \psi$  following  $Z - Y - X$  Euler angle conversion.  $R$  converts vector from the Hummingbird body coordinates system to the

world coordinates, as shown in Figure 5.2.

$$R = \begin{bmatrix} \cos \psi \cos \theta & -\sin \phi \cos \psi \sin \theta + \cos \phi \sin \psi & -\cos \psi \sin \theta \cos \phi - \sin \phi \sin \psi \\ -\cos \theta \sin \psi & \sin \phi \sin \psi \sin \theta + \cos \phi \cos \psi & \sin \psi \sin \theta \cos \phi - \sin \phi \cos \psi \\ \sin \theta & \cos \theta \sin \phi & \cos \phi \cos \theta \end{bmatrix} .$$

### 5.2.2 Acceleration Controller Design

The linear acceleration controller that controls the quadrotor's acceleration in  $X_w$ ,  $Y_w$ , and  $Z_w$  directions through changing its attitude and thrust force can be obtained by first rearranging the (5.1):

$$\begin{bmatrix} -F \sin \theta \cos \phi \\ F \sin \phi \\ F \cos \theta \cos \phi \end{bmatrix} = \begin{bmatrix} m\ddot{x} \cos \psi - m\ddot{y} \sin \psi \\ -m\ddot{x} \sin \psi - m\ddot{y} \cos \psi \\ m\ddot{z} + mg \end{bmatrix} . \quad (5.2)$$

Then the linear acceleration controller (5.3) can be solved from (5.2). It supplies Euler rotation angles  $(\phi, \theta, \psi)$  and thrust force  $F$  to the quadrotor's position dynamics (5.1) to achieve desired  $(\ddot{x}, \ddot{y}, \ddot{z})$  in world coordinates, assuming that the factory-shipped attitude controller realizes the attitude and thrust fast enough so that  $(\phi, \theta, \psi, F)$  are achieved almost instantaneously:

$$F = m\sqrt{(\ddot{z} + g)^2 + \ddot{x}^2 + \ddot{y}^2} , \quad (5.3a)$$

$$\theta = \arctan 2(-\ddot{x} \cos \psi + \ddot{y} \sin \psi, \ddot{z} + g) , \quad (5.3b)$$

$$\phi = \arctan 2((-\ddot{x} \sin \psi - \ddot{y} \cos \psi) \cos \theta, \ddot{z} + g) . \quad (5.3c)$$

Notice that there is no need to control the yaw angle  $\psi$  if only the accelerations in  $X_w, Y_w, Z_w$  directions need to be regulated. Thus the rotation rate  $\dot{\psi}$  is fixed to be zero, and the in flight measurement of  $\psi$  is used to complete the controller (5.3).

### 5.2.3 Planar Trajectory Controller

In this section, only the planar motion of the quadrotor is considered while the quadrotor's motion in  $Z$  direction is controlled independently. Using linear acceleration controller (5.3a), (5.3b), the planar position dynamics  $x_i \in \mathbb{R}^2$  of the quadrotor platform  $i$  can be controlled in the form of a double integrator with input  $w_i \in \mathbb{R}^2$

$$\ddot{x}_i = w_i \quad , \quad (5.4)$$

with  $w_i = (\ddot{w}_{x_i}, \ddot{w}_{y_i})$  is supplied to (5.3a), (5.3b). A backstepping controller is then designed to ensure  $\dot{x}_i$  converge to a desired velocity reference  $u_i^\circ = u_i^\circ(x_i, x_t, \dot{x}_t)$  given by the potential field gradient (4.3) constructed in Chapter 4. (Note that similar control architectures have been used for convergence to fixed points [3, 35].) It follows that for a choice of parameter  $k_d > 0$ , the input to (5.4) can be set as

$$w_i = \dot{u}_i^\circ - \nabla_{x_i} \varphi_i - k_d [\dot{x}_i - u_i^\circ] \quad . \quad (5.5)$$

**Proposition 5.2.1** *For the closed-loop system (5.4)–(5.5), convergence of  $\dot{x}_i$  to  $u_i^\circ$  is guaranteed.*

**Proof** First write the error in the reference velocity as  $e_v = \dot{x}_i - u_i^\circ$ , and express the closed-loop system in the form

$$\begin{aligned} \dot{x}_i &= u_i^\circ + e_v \quad , \\ \dot{e}_v &= w_i - \dot{u}_i^\circ \quad . \end{aligned}$$

Consider now the (time-varying) function

$$V(x_i, x_t, e_v) = \varphi_i(x_i, x_t) + \frac{1}{2} e_v^\top e_v$$

and compute

$$\begin{aligned} \dot{V} &= \nabla_{x_i} \varphi_i^\top (u_i^\circ + e_v) + \nabla_{x_t} \varphi_i^\top \dot{x}_t + e_v^\top (w_i - \dot{u}_i^\circ) \\ &= -c \frac{\|\nabla_{x_i} \varphi_i\|^2}{\|\nabla_{x_i} \varphi_i\| + \xi} + (\nabla_{x_i} \varphi_i + w_i - \dot{u}_i^\circ)^\top e_v \quad . \end{aligned}$$

Let the control input  $w_i$  to (5.5) yields

$$\dot{V} = -c \frac{\|\nabla_{x_i} \varphi_i\|^2}{\|\nabla_{x_i} \varphi_i\| + \xi} - k_d e_v^\top e_v .$$

Application of Barbalat's lemma along lines parallel to those in Chapter 4 completes the proof by showing that  $\nabla_{x_i} \varphi_i$  and  $e_v$  converge to zero with time. The only requirement additional to the treatment of Chapter 4 is that  $e_v$  has to be bounded; this is however, ensured from the negative semidefiniteness of  $\dot{V}$  and the positive definiteness of  $V$  with respect to  $x_i$  and  $e_v$ .

## 5.3 Wheeled Robot

### 5.3.1 Kinematic Model

The iCreate is a wheeled ground mobile robot manufactured by iRobot<sup>TM</sup> (Figure 5.3). It is essentially a differential drive robot that can be modeled using unicycle kinematic constraints taking linear velocity  $v$  and angular velocity  $\omega$  as input:

$$\dot{x}_r = v \cos \theta_r , \quad \dot{y}_r = v \sin \theta_r , \quad \dot{\theta}_r = \omega . \quad (5.6)$$

### 5.3.2 Position Controller

A Geiger counter is mounted on top of the robot to collect radiation measurements. It is the position of this sensor that should be driven towards the target. The geometric setup between the sensor and robot is shown in Figure 5.4.

The sensor position can be described as  $x_s = r_s \cos \theta_r + x_r$  and  $y_s = r_s \sin \theta_r + y_r$ , Its kinematics is governed by:

$$\begin{aligned} \dot{x}_s &= v \cos \theta_r - r_s \omega \sin \theta_r , \\ \dot{y}_s &= v \sin \theta_r + r_s \omega \cos \theta_r . \end{aligned}$$

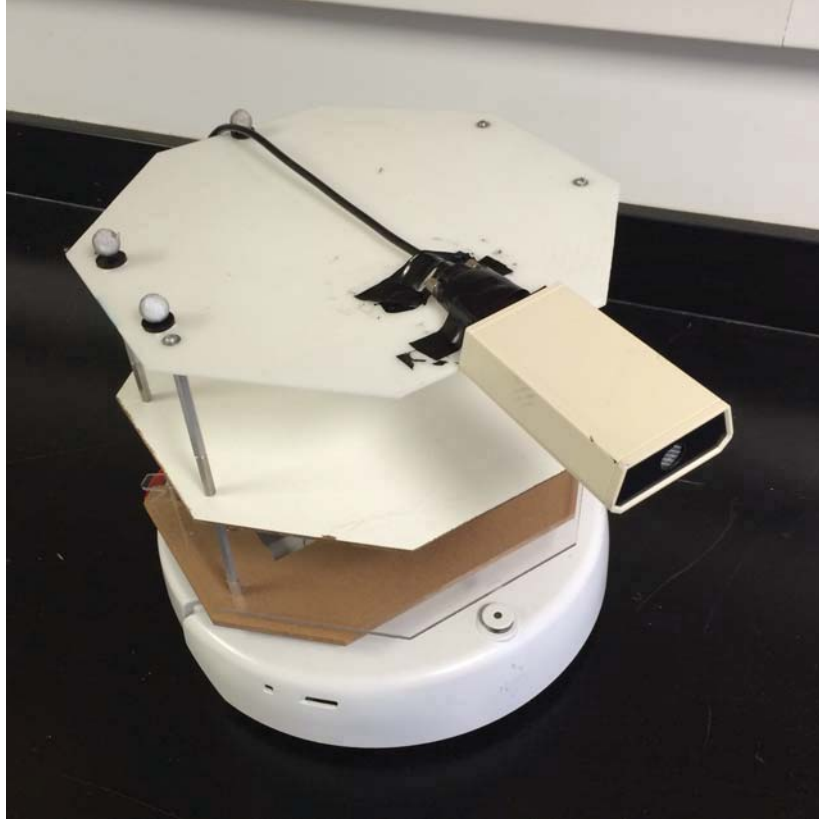


**Figure 5.3:** The iCreate robot with a Geiger counter mounted on top of it.

Thus in order to drive the sensor at a specific speed described by  $(\dot{x}_{des}, \dot{y}_{des})$ , iCreate should be driven with velocity  $(v, \omega)$ :

$$\begin{aligned} v &= \dot{x}_{des} \cos \theta_r + \dot{y}_{des} \sin \theta_r \ , \\ \omega &= \frac{1}{r_s} (-\dot{x}_{des} \sin \theta_r + \dot{y}_{des} \cos \theta_r) \ . \end{aligned} \tag{5.7}$$

Using controller (5.7), the sensor can be driven as if it was a single integrator. Thus the navigation controller (4.3) can be directly applied.

#### 5.4 Conclusions

By designing the lower-level controllers (5.3), (5.5) and (5.7), the navigation function based motion planner proposed in Chapter 4 can be implemented on robots

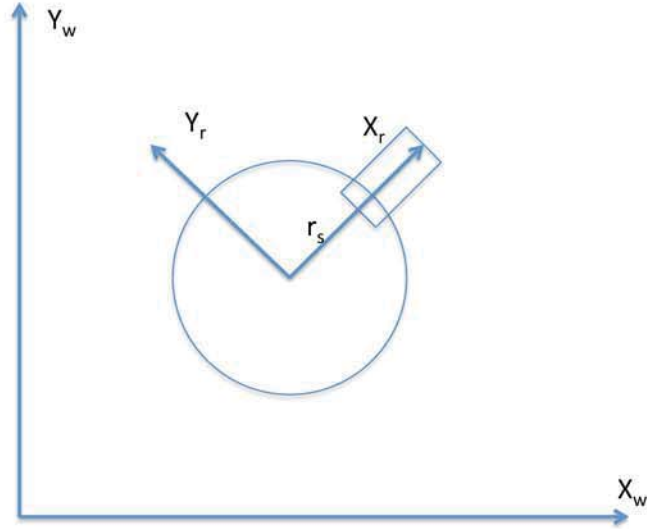


**Figure 5.4:** The geometric model of the iCreate. The sensor is mounted along the  $x_r$ -axis, which is the forward direction of iCreate. The distance between the sensor and the iCreate's body center is denoted  $r_s$ .

including quadrotors and wheeled robots. With this complete control framework including both the high level motion planner based on navigation function and the low level platform interface introduced in this chapter, simulations and experiments can be performed to show the advantage of using mobile sensors in radiation detection.

## Chapter 6

### SIMULATION RESULTS

Under certain simplifying assumptions, sensor mobility can be optimally utilized in the context of networks of radiation counters to boost detection performance in low-rate radiation activity detection scenarios. In the problem at hand, the suspected source is mobile, and sensors have knowledge of its position and velocity. Analytic optimal control solutions point to motion coordination strategies that tend to minimize the distance between sensor and suspected source as quickly as possible, resembling bang-bang minimum-time solutions to optimal control problems.

This optimal radiation detection strategy proposed in Chapter 3 uses the Chernoff bounds on error probabilities to evaluate the performance of radiation detection, which is due to the difficulty in obtaining the analytic expression for  $P_{FA}$  and  $P_M$ . Yet these values can be numerically estimated using Monte-Carlo simulations. In this chapter, a comparison between the Chernoff bounds and Monte-Carlo estimates reveals that the slopes of the curves of both bounds and Monte Carlo probability estimates are consistent, indicating that using the bounds as a proxy for the true—but unknown—error probabilities may not significantly affect the performance of optimal controllers.

Taking the analytic, closed-form solutions obtained for sensor motion in unconstrained environments, motion planning strategies are developed for sensor coordination and navigation in obstacle environments with bounds on actuation effort in Chapter 4. The motion planning methodology is based on gradient descent along potential fields generated by a special type of time-varying navigation functions. The resulting control laws are feedback-based and reactive to the source’s motion, ensuring asymptotic tracking of the mobile source in addition to obstacle avoidance. The control strategy is tested in simulation on a two-dimensional detection scenario regarding its

boundedness in Section 6.2, and the detection efficiency is confirmed through Monte Carlo analysis in Section 6.3.

### 6.1 Chernoff Bounds: Monte Carlo Validation

To provide some indication regarding the ability of the bounds derived in (3.8) and (3.7) to capture the corresponding error probabilities, this section compares these bounds against Monte-Carlo estimates of  $P_{FA}$  and  $P_M$  defined by (2.1). The comparison is performed in the context of the following example. This example is from [50].

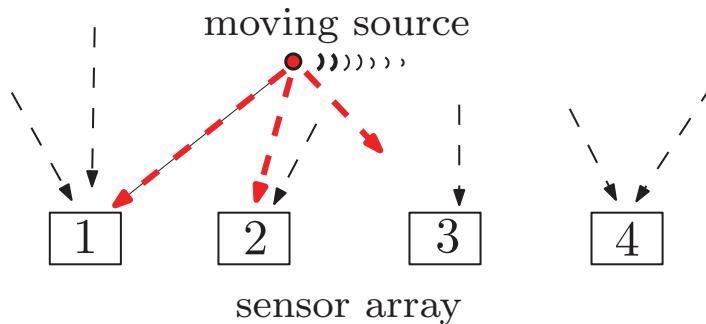


**Figure 6.1:** A planar sensor array detecting a moving source. Thick dashed arrows mark gamma rays emitted by the source, while thin dashed arrows are background.

Consider  $k = 4$  identical sensors (see Figure 6.1). The sensors, stationary at planar coordinates (in m)  $(0, 0)$ ,  $(0.5, 0)$ ,  $(1.5, 0)$ ,  $(2.5, 0)$ , are labeled 1 through 4 respectively. A source of intensity  $a = 120$  cpm is initialized at coordinates  $(3.0, 0.5)$  m, and starts moving parallel to the  $x$  axis, in a negative direction, from sensor 4 toward sensor 1, with a constant speed of  $0.03$  m/s. The background is  $\beta = 10$  cpm and the decision time is  $T = 100$  s<sup>1</sup>.

<sup>1</sup> The values for these calculations are chosen to match the experimental parameters of Section 7.5; they are not to be understood in themselves as typical in a real nuclear detection scenario, although their relative scale can produce computational results that are—see [29].

To generate samples of a inhomogeneous Poisson process, the method of *thinning* [39, 51] is used. In more detail, to simulate a Poisson process with time-dependent intensity  $\lambda(t)$ , a constant intensity  $\lambda_d > 0$  which dominates  $\lambda(t)$  should be set first so that  $0 \leq \lambda(t) \leq \lambda_d$  for all  $t \in [0, T]$ . Assumptions 2.1.2 and 2.1.3 ensure that a suitable  $\lambda_d$  can be found. Thus a sample path of a homogeneous Poisson process with intensity  $\lambda_d$  can be generated. Suppose that  $T_1^*, T_2^*, \dots, T_n^*$  are the event times (corresponding to jumps of the Poisson process) over  $(0, T]$ . Each event time  $T_j^*$  is retained with probability  $\lambda(T_j^*)/\lambda_d$  and deleted with probability  $1 - \lambda(T_j^*)/\lambda_d$ . The retained event times now correspond to a sample path of a Poisson process with time-dependent intensity  $\lambda(t)$  [39], [51, Theorem 3]. Notice that in our problem,  $\lambda(t)$  will be of one of the two forms  $\beta_i(t)$  and  $\mu_i(t)\beta_i(t)$ .

With this procedure at hand for generating samples of inhomogeneous Poisson processes,  $P_{FA} = \mathbb{P}_0(L_T \geq \gamma)$  and  $P_M = \mathbb{P}_1(L_T < \gamma)$  for  $L_T$  computed as in Theorem 2.2.1 can be estimated for different values of the threshold  $\gamma > 0$ . To estimate the probability of false alarm  $P_{FA}$ , let

$$A_\gamma \triangleq \{\omega \in \Omega : L_T(\omega) \geq \gamma\} .$$

$n$  samples  $\omega_1, \omega_2, \dots, \omega_n$  are drawn from  $\Omega$  according to the probability measure  $\mathbb{P}_0$ . This corresponds to generating  $n$  realizations of the ( $k$ -dimensional) process  $\mathbf{N}_t = (N_t(1), \dots, N_t(k))$  over time  $t \in [0, T]$ , where the  $N_t(i)$ 's are independent Poisson processes with intensities given by  $\beta$ . For each such realization, the likelihood ratio  $L_T = L_T(\omega_i)$  can be computed as in Theorem 2.2.1 and the probability  $P_{FA} = \mathbb{P}_0(A_\gamma)$  can be approximated by

$$\frac{1}{n} \sum_{i=1}^n 1_{A_\gamma}(\omega_i) . \tag{6.1}$$

Similarly, to estimate the probability of miss let

$$A_\gamma^c \triangleq \Omega \setminus A_\gamma = \{\omega \in \Omega : L_T(\omega) < \gamma\} .$$

$n$  samples  $\omega_1, \omega_2, \dots, \omega_n$  are drawn from  $\Omega$ , now according to the probability measure  $\mathbb{P}_1$ . Equivalently,  $n$  realizations of  $\mathbf{N}_t = (N_t(1), \dots, N_t(k))$  over  $t \in [0, T]$  are generated, where the  $N_t(i)$ 's are independent Poisson process with intensities  $\mu_i(t)\beta_i(t)$ . Computing  $L_T = L_T(\omega_i)$  for each realization,  $P_M = \mathbb{P}_1(A_\gamma^c)$  is estimated by

$$\frac{1}{n} \sum_{i=1}^n 1_{A_\gamma^c}(\omega_i) . \quad (6.2)$$

To ensure that the estimates in (6.1), (6.2) are sufficiently close to  $\mathbb{P}_0(A_\gamma)$ ,  $\mathbb{P}_1(A_\gamma^c)$  with high enough probability,  $n$  (number of samples) should be large enough. Indeed, for  $\varepsilon, \delta \in (0, 1)$ , taking  $n \geq \frac{1}{2\varepsilon^2} \ln \frac{2}{\delta}$  ensures [73] that the quantities in (6.1), (6.2) estimate the corresponding probabilities to accuracy  $\varepsilon > 0$  and confidence  $1 - \delta$ :

$$\mathbb{P}_0 \left( \left| \frac{1}{n} \sum_{i=1}^n 1_{A_\gamma}(\omega_i) - \mathbb{P}_0(A_\gamma) \right| \leq \varepsilon \right) \geq 1 - \delta ,$$

$$\mathbb{P}_1 \left( \left| \frac{1}{n} \sum_{i=1}^n 1_{A_\gamma^c}(\omega_i) - \mathbb{P}_1(A_\gamma^c) \right| \leq \varepsilon \right) \geq 1 - \delta .$$

For instance, to approximate the probabilities to within 1% (corresponding to  $\varepsilon = 0.01$ ), with a confidence of 95% (corresponding to  $\delta = 0.05$ ) 18 445 runs are needed.

Figure 6.2 compares (the Monte Carlo estimates of) the error probabilities  $P_{FA}$  and  $P_M$  with the corresponding Chernoff upper bounds, for various values of the threshold. For example, based on Figure 6.2, and for an acceptable false alarm rate of less than 5%, one can choose a threshold  $\gamma$  by interpolating the ‘‘Monte Carlo PF’’ line between  $\log_{10} \gamma = -2$  and  $\log_{10} \gamma = 0$  and the error in approximating this probability using the Chernoff bound for the same threshold is in the order of 20%. Clearly, for both  $P_{FA}$  and  $P_M$ , the Chernoff bounds and Monte Carlo estimates tend to agree around the values of 0 and 1 (the two ends of the horizontal axis). Due to the constraint imposed on the probability of false alarm (typically, far below 0.1), realistic instantiations of these bounds are more likely to occur at values of  $P_{FA}$  close to zero, suggesting large thresholds, further to the right than the depicted scale in Figure 6.2. Due to numerical difficulties in obtaining reasonable estimates using the Monte-Carlo method,

the probability estimates could not be easily extended to this part of the threshold domain. Yet extrapolating from the graphs of the figure indicates that the Chernoff bound for the probability of false alarm will further close the distance between itself and the actual false alarm probability while maintaining its decreasing trend. But, what is more important in the context of sensor mobility optimization is the fact that the slopes of the curves of both bounds and Monte Carlo probability estimates are consistent, indicating that using the bounds as a proxy for the true—but unknown—error

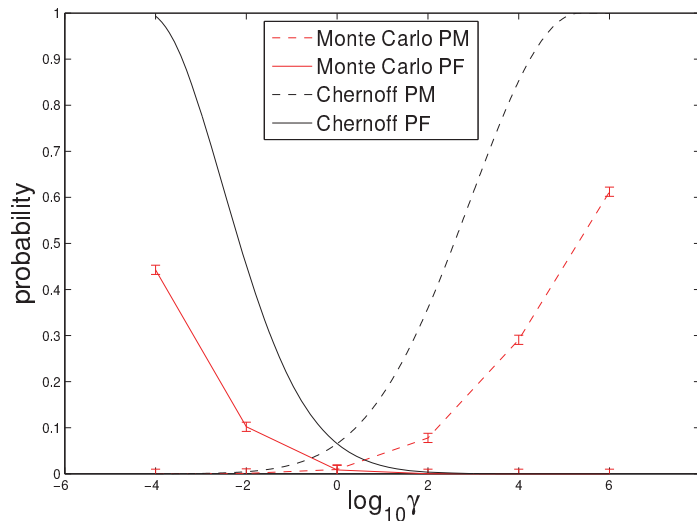


**Figure 6.2:** Comparison between our Chernoff bounds and Monte Carlo simulation estimates of the error probabilities —false alarm (PF), and probability of miss (PM)—for a range of different likelihood ratio thresholds. The Monte Carlo probability estimates are shown in piece-wise linear curves, while Chernoff bounds curves are smooth. Solid curves denote estimates on the probability of false alarm, and dashed curves correspond to probability of miss estimates. The 95% confidence intervals are marked over Monte Carlo estimate points. The emission rates for source and background are taken equal to the ones used in Section 7.5:  $a = 120$  cpm for the source, and  $\beta = 10$  cpm for background. These activity numbers may be artificial, selected to match our (slow) emission rates of our emulation apparatus of Section 7.5, but their ratio matches the order of magnitude of intensities in real-life detection scenarios [22].

probabilities may not significantly affect the performance of optimal controllers.

## 6.2 Boundedness of the Navigation Function Based Motion Planner

Consider a 2-and-a-half dimensional environment, the projection of which on the 2 dimensional horizontal plane gives the planar workspace topology of Figure 6.3. In this environment, a simulated point quadrotor is steered to track a point target moving counterclockwise along a circular path around the origin with angular velocity  $\frac{\pi}{5}$  rad per second. The thin solid (blue) path in Figure 6.3 corresponds to the simulated quadrotor's trajectory. The target initially starts at point  $(x, y) = (0.15, 0)$  m, and in the scenarios shown in Figure 6.3, it is assumed that the target's position and velocity are known exactly. The minimum safe distance is 0.05m.

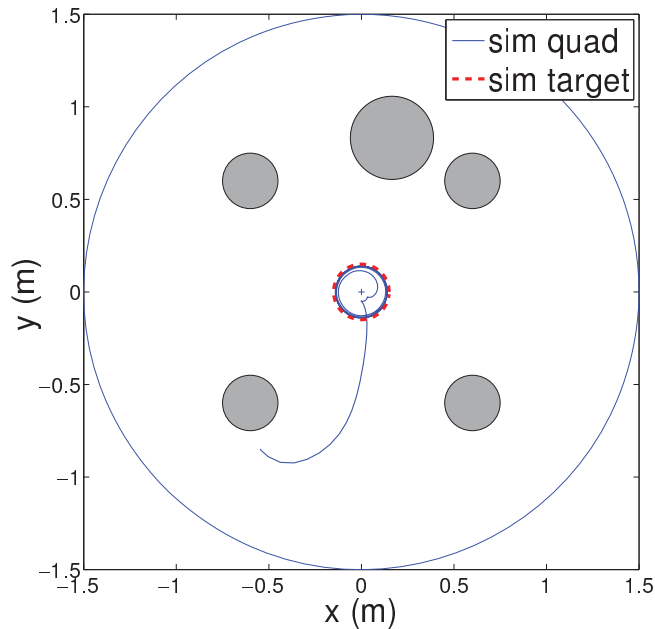


**Figure 6.3:** Simulation: a target is circling the origin along a thick red dashed path, and a quadrotor starting from behind an obstacle follows a thin blue solid path as it converges to its target and follows it around in circles. Here, the path of the quadrotor is marked with a thin solid blue line, while the motion of its target is shown in thick dashed red.

Lemma 4.4.1 warns about the existence of trajectories attracted to a neighborhood of saddles, which is illustrated in Figure 6.4, showing that the attraction basin is typically of small measure. Indeed, Figure 6.4 marks initial positions from which trajectories cross into

$$\left\{ x_i : 1 + \frac{\|J_i \nabla_{x_i} \beta\|}{\|k_i \beta \nabla_{x_i} J_i - J_i \nabla_{x_i} \beta\|} \geq \frac{u_{max} - c}{\max\{\|\dot{x}_t\|\}} = 10 \right\} .$$

The marked region shrinks as  $u_{max}$  is increased.

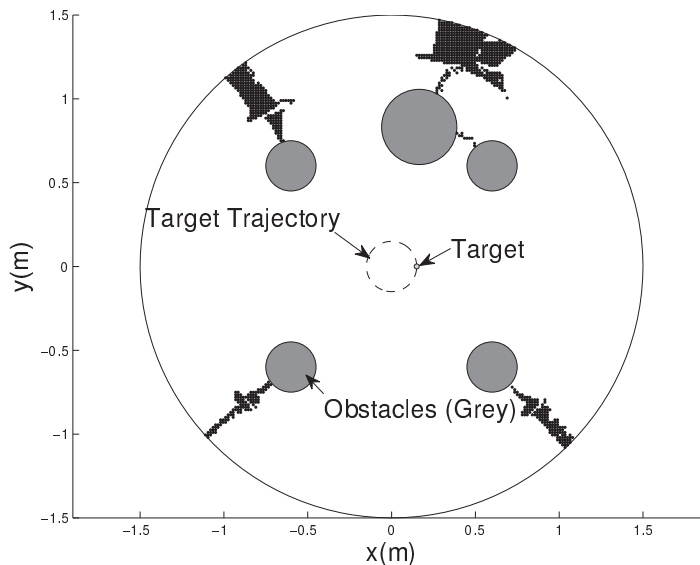


**Figure 6.4:** A graph showing the feasible region (white) and regions requiring velocity references that are 10 times higher than target velocity (black) inside the workspace for a point target following circular trajectory centered at origin with radius  $r = 0.15$  and angular velocity  $\omega = \pi/5$  that starts at point  $(0.15, 0)$ .

### 6.3 Simulated Radiation Detection With Mobile Sensors

A  $2\frac{1}{2}$  dimensional space simulation scenario (the environment geometry is invariant along the third spatial coordinate) is used to test the control law. Its two-dimensional projection is depicted in Figure 6.5. Sensor and source physical volumes are neglected. The target is following a sinusoid trajectory starting initially at point

$(x, y) = (15, 0)$ (m). Its  $x$  velocity is constantly  $0.3\pi$ (m/s) and  $y$  velocity is given as  $0.3\pi \cos(\frac{\pi}{50}t)$ (m/s). It is assumed that the target's position and velocity is known to all sensors.

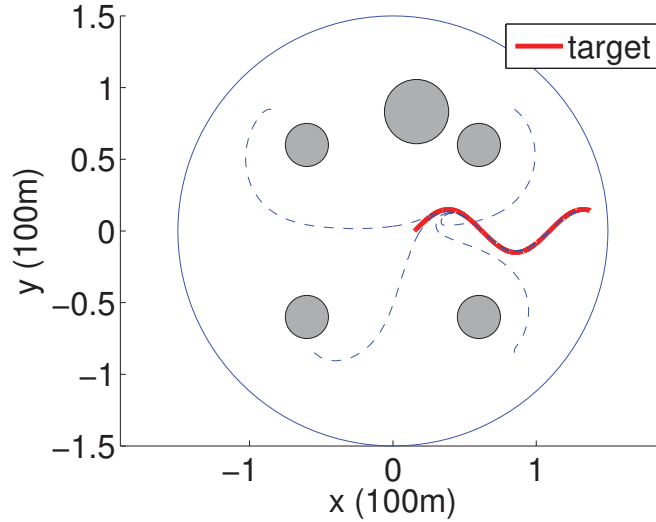


**Figure 6.5:** A 2D simulation scenario. A source carrying target is circling the origin and its path is shown as a thick (red) curve. Four mobile sensors start moving from initial positions behind disk-shaped obstacles, and navigate along the dashed-line paths toward the source's neighborhood following the gradient field of a time-varying navigation function. Sensors collect measurements for a time window of two minutes before they make a decision as to whether the target is radioactive.

Applying control law (4.3) to each sensor dynamics (3.13), results in the motion behavior shown in Figure 6.5. By closing the distance between themselves and the target while navigating their cluttered workspace, they increase their SNR of their radiation measurements. A detection time window  $T = 130$  s is considered, after which sensors are called to make a decision based on their measurements as to whether the target they were tracking was radioactive.

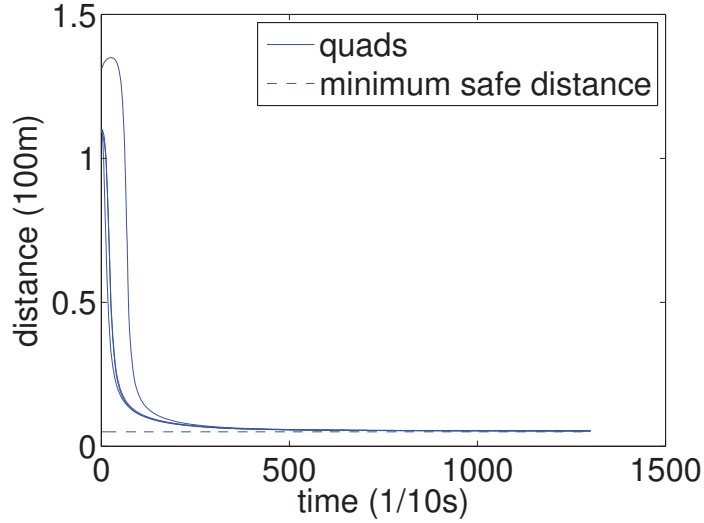


**Figure 6.6:** Distance between sensors and target. Our simulation test bed refers to mobile sensors as quads, envisioning quadrotors equipped with Geiger counters.

The target is indeed radioactive, with an activity of  $a = 2.4 \times 10^6$  (Poisson mean) counts per minute, while the background radiation is taken to be at a level of  $b = 10$  counts per minute. Despite this large difference, the sensor geometric characteristics as expressed by the cross-section coefficient  $\chi = 10^{-4} m^2$  combined with the inverse square distance effect render the average *perceived* source activity  $\nu_i$  (see (3.1)) at the sensor's location comparable to background.

Along these paths, 2 sample sets of 73 778 i.i.d. two-minute histories of simulated radiation measurements are recorded. The target is set to be radioactive in one set and benign in the other. For each sample, a binary hypothesis test 2.2.1 is performed with a threshold of  $\gamma = 3.4$ , designed to guarantee a false alarm rate of less than 1 % [50]. Monte Carlo methods empirically estimate the probability of false alarms and correct detection at an accuracy level of  $\varepsilon = 0.005$  and confidence of 95 % [74]. These estimates

are 0.12% for the false alarm, and 99.42% for the detection rate.

#### **6.4 Conclusion**

The numerical difference between the Chernoff bounds and the actual probability of errors in [LRT](#) is shown in [Section 6.1](#), which suggests that in the region of low probability of false alarm rate, the value difference between Chernoff bounds and Monte Carlo estimated probability of errors is not large. It is also convinced that except for a limited set of initial conditions, the proposed navigation function based controller is always bounded and converge to the desired target set. The simulated radiation detection task is also a success, which paves way for conducting such experiment on physical platforms with real Geiger counters and radioactive source.

## Chapter 7

### EXPERIMENTAL VALIDATION

The theory for optimal radiation detection, and the controllers that are adaptable to different robot platforms are proposed in the previous chapters. The effectiveness of the optimal strategy, the stability and the boundedness of our controllers are shown in simulation. In this chapter, it is validated through experiments that using mobile sensors enables detecting mobile weak sources that would otherwise pass stationary radiation counters unnoticed.

The robot control system that supports our experiments with radiation detection using mobile sensors is first introduced. The overview of the experiment system is provided to give a big picture on how different components including robots and sensors are bind together. Then a deeper look into the quadrotor controller's state transitions explains the switching logic between navigation function controller and Proportional-Integral-Derivative (PID) controller, which helps achieving better flight performance in terms of stability and accuracy.

The effectiveness of mobile sensors in radiation detection tasks is demonstrated by two sets of experiments. The laser emulated radiation detection experiment is designed to compare the difference between using static sensors and mobile sensors. In this experiment, a laser device is used to emulate radiation emission process. With this laser device, experiments can be safely conducted to validate our radiation detection method while avoiding the usage of strongly radioactive materials that may be hazardous. The detection performance of using four static sensors is compared to that of using three static sensors combined with one mobile sensor. It is shown that the additional mobile sensor greatly improves detection rate by significantly increasing the signal to noise ratio. Convinced that mobile sensor is the key to detecting low intensity

radioactive materials, an experiment is designed to detect Vaseline beads using mobile robots carrying Geiger counters, which are extremely weak radioactive sources. Our tests showed that the radiation intensity read from these beads using Geiger counter drop to 10% of background radiation level when observed 15 cm away. Yet detecting the presence of these beads mounted on a crawler robot is made possible using one ground robot and one aerial robot.

## 7.1 Robot Control System

The radiation detection experiment described in Section 7.6 validates that even a weak mobile source can be detected using mobile sensors. Two robots are used in that experiment: one ground wheeled robot iCreate from iRobot, one aerial quadrotor Hummingbird from AscTec. Previous chapters cover the theoretical side of the controller design that drives these two robots towards the target set while avoiding obstacles. This section covers the actual implementation of these controllers on physical platforms, which requires integration of multiple software and hardware systems.

The experiments are conducted indoor without GPS guidance. Thus the localization task is taken care of by Vicon motion capture system, which provides feedback terms to our navigation controller implementation. Extra sensors including a camera and a Geiger counter are mounted on Hummingbird to enable vision based target tracking and collecting radiations counts respectively. A portable computer, Raspberry Pi, is loaded on Hummingbird to process and transmit these sensory data. iCreate carries another Geiger counter to gather more radiation statistics along with the Hummingbird during the detection period, which would allow more accurate determination of the target's radioactive nature.

The expected experiment procedure would be:

1. Hummingbird starts tracking the target and shares the target position with iCreate.

2. With target information, both robots can get into close range of target while avoiding obstacles using navigation function-based controller.
3. Use Geiger counters mounted on the two robots to collect radiation readings during the detection period.
4. Record all necessary information for radiation detection procedure listed in the end of Chapter 3.
5. Run data processing after collecting all the data and decide whether the target is radioactive or not.

Now to bind all the hardware together to achieve this expected experiment procedure, a robot control system is developed, and its layout is illustrated in Figure 7.1. Looking at the structure of this system layout, it is apparent that the Robot Operating System (ROS) nodes (green blocks) are the main structures that support communication between software and hardware, and between different subsystems such as robots, PC, Vicon motion tracking system, etc. A quick introduction to ROS will show the advantage brought by adopting it as the foundation of our robot control system.

ROS is a widely used open source robot operating system that provides hardware-to-software interfaces for commonly used robots and sensor systems, and communication infrastructure between distributed processes deployed on multiple platforms. The basic elements in ROS are nodes, which can be considered as individual programs. A ROS network consists multiple ROS node and a ROS master-node. The ROS master-node provides basic functions in ROS and must be initialized before any other nodes are created. For our application, the master node is created on the Master PC. All the green blocks in the Figure 7.1 are customized ROS nodes that are running in its own thread.

The ROS system provides multiple methods for these nodes to exchange information with each other. One of the most commonly used interfaces is “topic”. This is a powerful tool that enables us to easily link different components of the robot

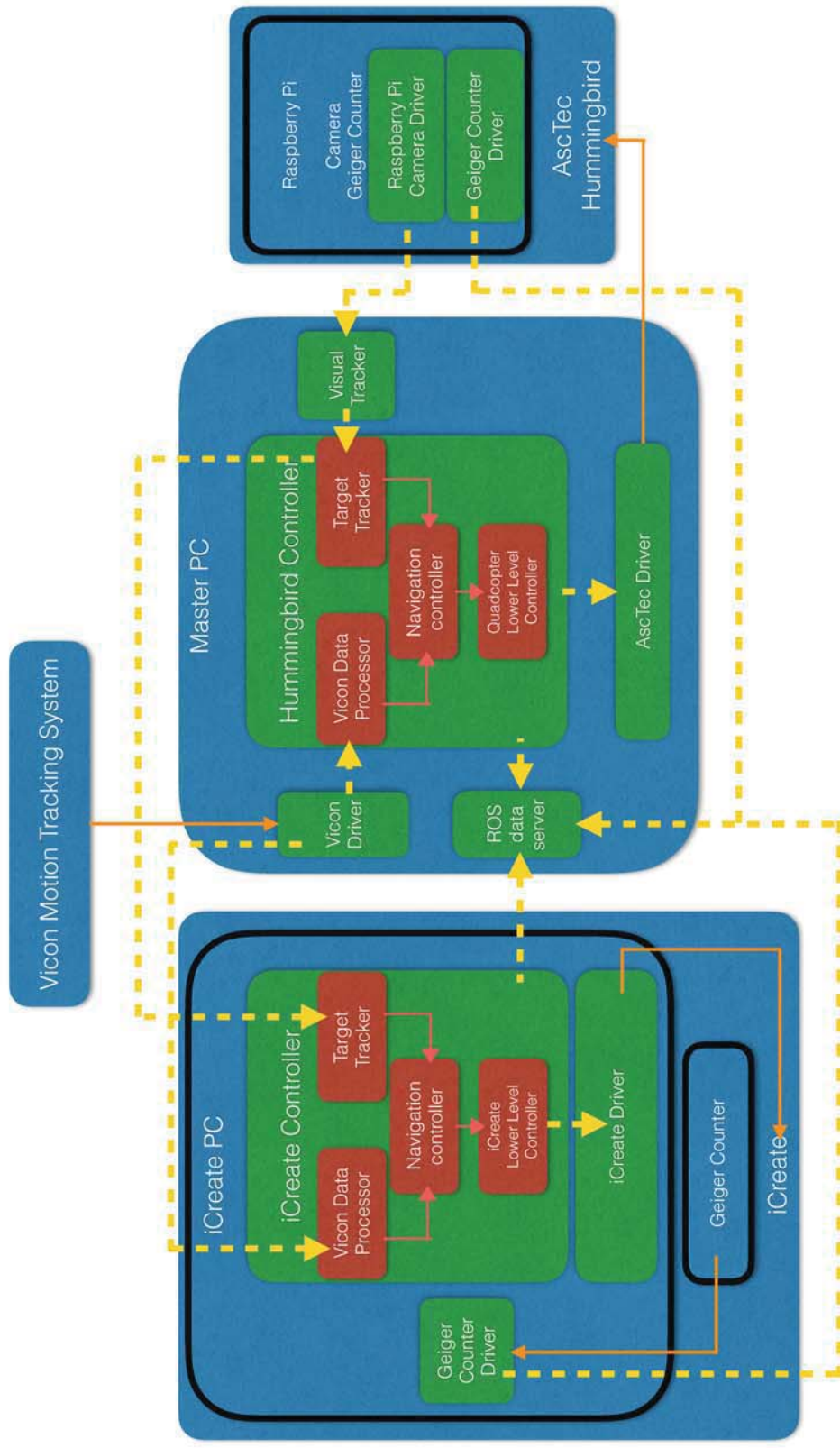


**Figure 7.1:** The overview of the hardware-software system that enables target tracking using a ground robot iCreate and an aerial robot Hummingbird. The blue blocks are hardware used in experiment. The green blocks are ROS nodes created. The red blocks are core controller system components. Communication between hardware and software is marked by orange links. Communication between ROS nodes are marked by yellow dashed links. The 'block contains block' relation translates to a 'physically contains' between the hardware blocks or 'hosts software' relation between the hardware blocks and the software blocks. Take the leftmost iCreate block as an example: the iCreate robot contains a Geiger Counter and a iCreate PC. The iCreate PC hosts several ROS nodes that link the iCreate robot with the rest of the robot control system.

system together without worrying about the network configurations or data transmission protocols. For example: in our application, the *Visual Tracker* node needs to obtain the pictures taken by the camera from the *Raspberry Pi Camera Driver* node through remote communication. So the *Raspberry Pi Camera Driver* node publishes a topic called */camera/image/compressed* and the *Visual Tracker* node subscribes to the same topic. The ROS master node will then connect the publisher (*Raspberry Pi Camera Driver* node) with the subscriber (*Visual Tracker* node) and image data can be transmitted through this topic using network interface (in this case, WIFI). ROS also allows multiple nodes publishing and subscribing the same topic simultaneously, a feature that enables information sharing among several nodes.

Another great advantage of using ROS is that it has a widely spread user base due to its open source nature. Researchers and engineers all over the world are contributing to the ROS environment, providing numerous off-the-shelf software packages that can be utilized in our application. Specifically in our system layout, the *iCreate Driver*, the *Hummingbird Driver*, the *Raspberry Pi Camera Driver*, and the *Vicon Driver* are all available as open source packages. Then the only hardware driver I need to develop myself is the *Geiger Counter Driver*. This advantage of using ROS packages saves a huge amount of development time and allows us to focus on our interest: the *iCreate Controller*, the *Hummingbird Controller* and the *Visual Tracker*.

If one looks closely at the robot controller nodes, it will be clear that the *iCreate* controller and the *Hummingbird* controller have a lot in common. This reflects the advantage of our navigation controller design: Our higher level navigation controller can be easily adopted by different robots through their lower level controller layer. Yet, controlling *Hummingbird* still requires slightly more sophisticated control logic that was not shown in the system layout for the sake of compactness of the layout. For a quadrotor like *Hummingbird*, the Navigation Controller is more suitable for tracking continuous trajectory, whereas PID controller provides better stability when the quadrotor is driven from point to point, which are close to each other. In order to achieve successful flight mission, a combination of Navigation Controller and PID

controller is necessary. In the next section, the state transitions during a flight mission is introduced, explaining how to utilize these two types of controllers.

## 7.2 State Transitions in Quadrotor Controller

The overview of the state transitions during one quadrotor flight mission is shown in Figure 7.2.

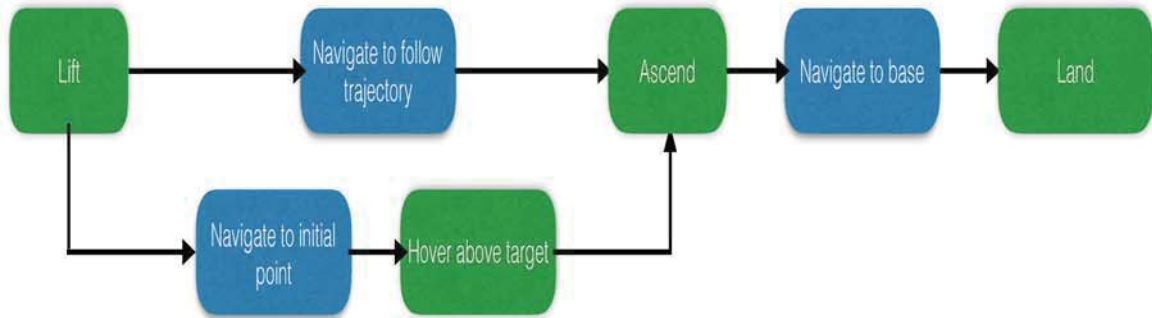


**Figure 7.2:** The state transitions during quadrotor flight missions. The green blocks invoke **PID** controller for point to point motion. The blue blocks invoke Navigation Controller for tracking trajectory while avoiding obstacles.

The combination of Navigation Controller and **PID** controller allows us to track the target using two different paths illustrated in Figure 7.2. The upper route shown in the flow diagram is to solely use Navigation Controller for target tracking. This method allows obstacle avoidance while tracking the target. However, due to the limitations of the Navigation function based controller, the quadrotor would tend to oscillate when its very close to the target set. Also due to the limitation on the AscTec proprietary attitude controller installed on Hummingbird, the quadrotor sometimes cannot reach the desired attitude given by the navigation controller instantaneously. These limitations are shown in the next section by a comparison between ideal simulated flight and real flight using Hummingbird to track a circular trajectory.

The lower route shown in the flow chart use Navigation Controller to get close to target's initial point while avoiding obstacles and then switch to **PID** controller to

keep hovering over target. This strategy provides relatively more stable motion but it does not consider obstacle avoidance during tracking. Yet assuming that the target will not run into obstacles by itself, the quadrotor can be allowed to keep tracking target without worrying about collisions. This route is taken for our radiation detection using multiple mobile robots experiment in Section 7.6 for its better flight stability.

The landing schedule for the quadrotor consists three blocks: *Ascend*, *Navigate to base*, and *Land*. During the tracking mission, the quadrotor usually operates at a very close range to other robots including the target robot and the other tracking robot iCreate. When the detection task comes to an end, it would be safer to first invoke the PID controller to lift the quadrotor to a higher altitude, which is done by the *Ascend* block, so that it has more space to maneuver. Once ascended, quadrotor is driven to the point above the landing base position using navigation controller (*Navigate to base* block). Upon reaching the flight area just above the base, the quadrotor would then lower itself using PID controller to a point  $< 5$  cm above ground, an altitude at which the quadrotor can then shutdown its motors and land safely (*Land* block).

### 7.3 Target Tracking Using Visual Feedback

As pointed out in our controller design, obtaining target position feedback is the prerequisite for close range radiation detection. In order to do so, a camera system is mounted on the quadrotor to take advantage of its overhead field of view. Each frame taken by the camera was sent back by the quadrotor's onboard computer Raspberry Pi and processed on the *Visual Tracker* ROS node hosted on Master PC. The *Visual Tracker* would figure out whether a target robot is in the field of view, where is the target with respect to the center of image frame and how much the target had moved from frame to frame. This refined information is then passed to the Hummingbird Controller. The Hummingbird Controller will deduce where the target is in the global frame and share this information with iCreate Controller.

### 7.3.1 Quadrotor Camera System

The onboard camera system consists of three components: a portable computer Raspberry Pi, a camera break out board, and a custom made landing support to provide mounting space for the Raspberry Pi and camera.

The red plastic parts in Figure 7.3 are components of the landing support. The joints between the landing supports and quadrotor are made into separate parts to connect the landing support to quadrotor base, instead of simply extend the quadrotor base to ground as a whole piece. Because these joints are constantly under impact during landing and require occasionally replacement. Instead of reproducing the whole extended landing support, only the broken joints need to be replaced.

The Raspberry Pi used here works as a transmitter that passes the camera images back to the more powerful workstation through wireless network. It is also used to gather gamma-ray counts from Geiger counter mounted along with the camera. The Raspberry Pi is powered through a 2-Cell Lithium Polymer (LiPo) battery and a 5V voltage regulator. The LiPo battery is favorable here for its high energy density and high current output, which are advantageous for our task since the payload on Hummingbird needs to be reduced as much as possible while being able to power up a small computer, a camera, a Geiger counter and a WIFI adapter. The wireless data transmission is especially power hungry when large amount of data such as compressed images are passed at relatively high frequency ( $\sim 10$  frames per second (FPS)).

The camera breakout board (Raspicam) is an off-the-shelf product designed to be used together with Raspberry Pi. It supports up to  $1920 \times 1080$  resolution image recording at speed up to 90 FPS. However to strike for a balance between the wireless network bandwidth and the image quality, images are captured with resolution  $320 \times 240$  pixels at 10 FPS in experiments. Also in Figure 7.4, Notice that since the camera is off center of the quadrotor with a 45 degree angle between the camera image coordinate's x axis and the quadrotor's body coordinate's x axis. When combining the local information from the camera and the global information from the Vicon system, the transform between the camera coordinate system and Hummingbird body

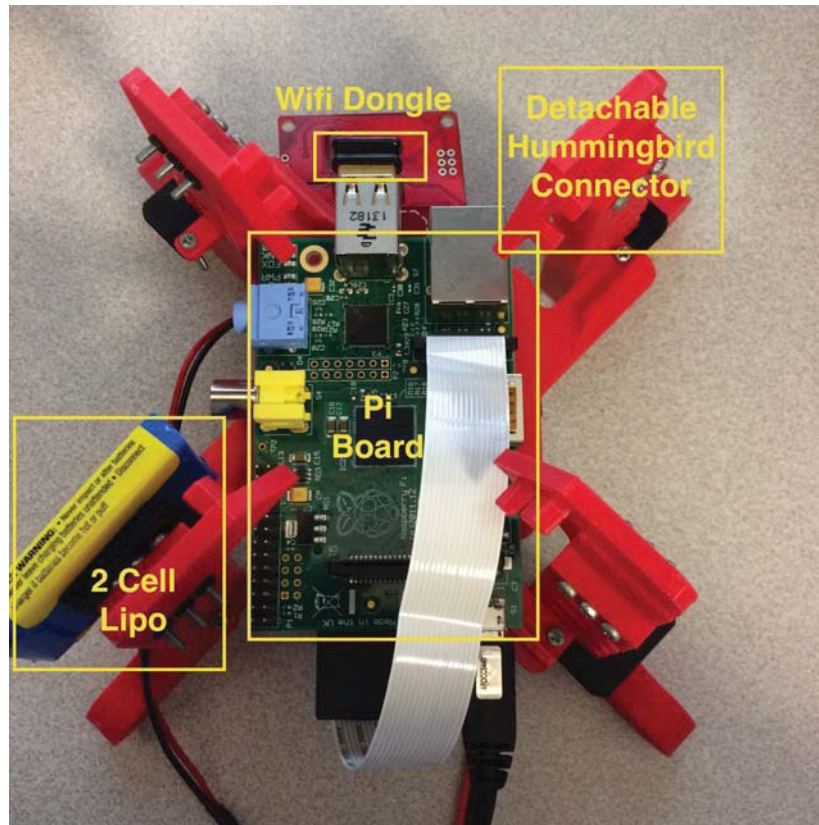


**Figure 7.3:** The sensor assembly is mounted on the customized 3D-printed landing support designed for Hummingbird. From the top side view, the Raspberry Pi, which is a miniature computer, is sitting in the center of the landing support. The Hummingbird carries a 2 cell LiPo battery to power up the Raspberry Pi and its attached sensors.

coordinate system must be treated carefully.

### 7.3.2 Image Transmission and Processing

The ROS Groovy is installed on Raspberry Pi along with a camera support ROS package. The camera support package extracts images frame by frame from the Raspicam and send them out using ROS topic interface through wireless network.

On the master computer, a *Visual Tracker* ROS node is created to process these incoming images. The ROS node stores an image of the target crawler robot a priori (Figure 7.5), which serves as a template of the target robot. Because the R-G-B values

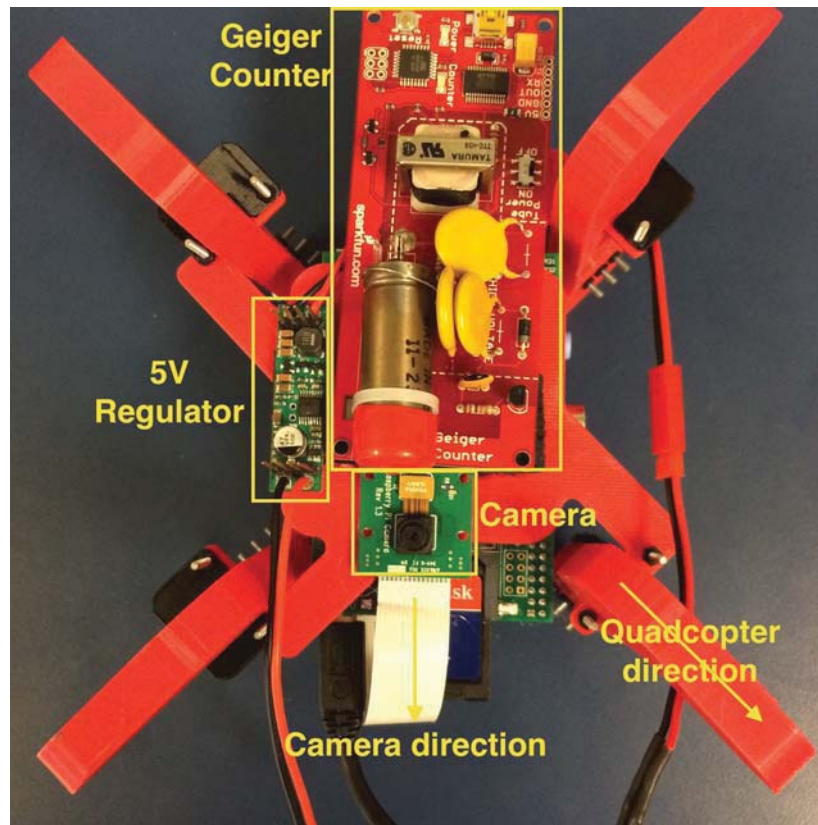


**Figure 7.4:** View on the bottom side of the landing support. The camera is fixed to the support to capture images looking downwards from the quadrotor. The Geiger counter's detection tube is placed next to the camera lens. 5 volts power regulator is used to regulate the voltage supplied by the [LiPo](#) battery (6.0 – 8.4 volts) and provide consistent 5 volts voltage to the Raspberry Pi board.

of the received image are all correlated with the amount of light hitting the object. its hue value is first extracted by converting RGB color to Hue Saturation Value ([HSV](#)) representation before processing the image for target tracking. This conversion can reduce the influence of lighting and saturation while keeping the color characteristics.

In the next step, the program would compare the received image ([Figure 7.6](#)) with the template to find out whether the target robot is in the current field of view. To perform such comparison in limited time period (0.1 second when images are coming in at 10 [FPS](#)), the incoming images are first shrank to  $160 \times 120$  pixels and then

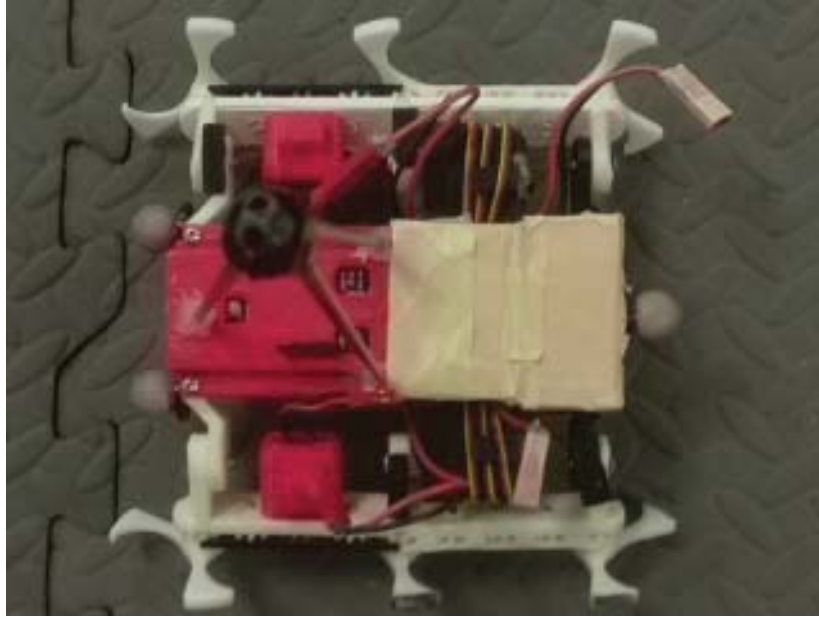


**Figure 7.5:** The template image pre-stored in the program, providing prior knowledge for detecting the presence of target robot.

the features in both template and incoming images are extracted and matched. The concept *image feature* intuitively corresponds to distinguishable region of an image that can be numerically detected and compared. The feature detector and extractor applied to these images is the Speeded Up Robust Feature ([SURF](#)) algorithm implemented in OpenCV library. [SURF](#) is the state-of-art image feature detector and extractor and it is invariant to scale and rotation, and sufficiently fast to handle our small size images at 10 [FPS](#).

The target robot is determined to be within the image frame if the matched features (linked dots in [Figure 7.7](#)) exceed a certain amount. The target's position in the camera coordinates is then computed as the center of mass of all matched feature points. Although there are quite a bit mis-alignment between the template and incoming frame, these mis-alignment won't affect our computation of target position because the matching transform are not used to calculate the pose of the target. The matching result are solely used to extract points in the incoming image that may belong



**Figure 7.6:** The raw image received by quadrotor during flight.



**Figure 7.7:** The hue part of the incoming frame (left) and the template image (right). The matched SURF features between two images are plotted as small dots linked by lines.

to part of the robot due to its visual similarities. This detection procedure is still coarse since it can not deal with the symmetry in the robot's geometric shape and the occlusion from other moving parts. These difficulties often lead to unavoidable false positives and misses in feature matching. In the experiment described in this dissertation, consistent gray floor mats are used to avoid false positives from background.

If the target is detected to be remaining in the field of view for consecutive frames, feature matching between two consecutive frames (Figure 7.8) is also performed to find out how much the target has moved within the image coordinate, which can be later transformed to global displacement given the pose of the quadrotor and camera at the times when these frames are taken.

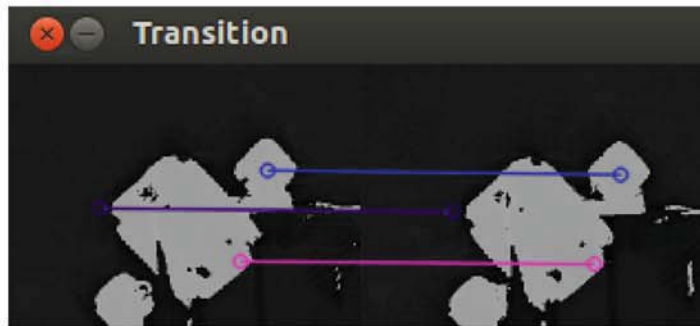


**Figure 7.8:** This figure shows the feature matching between two consecutive frames. Notice that the matching transform is much more consistent compared to Figure 7.7 since the two images have much more in common, which allows usage of a higher threshold to filter out false alarms. The similarity between frames is due to the fact that the robot's physical pose and the camera pose cannot change dramatically during the small time interval between frames, which is within 0.1 second in this application ignoring the network latency.

#### 7.4 Navigation Function Based Controller Performance

Consider a 2-and-a-half dimensional environment, the projection of which on the 2 dimensional horizontal plane gives the planar workspace topology of Figure 7.9. In this environment, a simulated point quadrotor is steered to track a point target

moving counterclockwise along a circular path around the origin with angular velocity  $\frac{\pi}{5}$  rad per second. Figure 7.9 compares the performance of this controller in simulation to the results of an experimental study that is discussed later in this section; at this stage we are interested in the thin solid (blue) path in Figure 7.9, which corresponds to the simulated vehicle’s trajectory. The target initially starts at point  $(x, y) = (0.15, 0)$  m, and in the scenarios shown in Figure 7.9, it is assumed that the target’s position and velocity are known exactly.

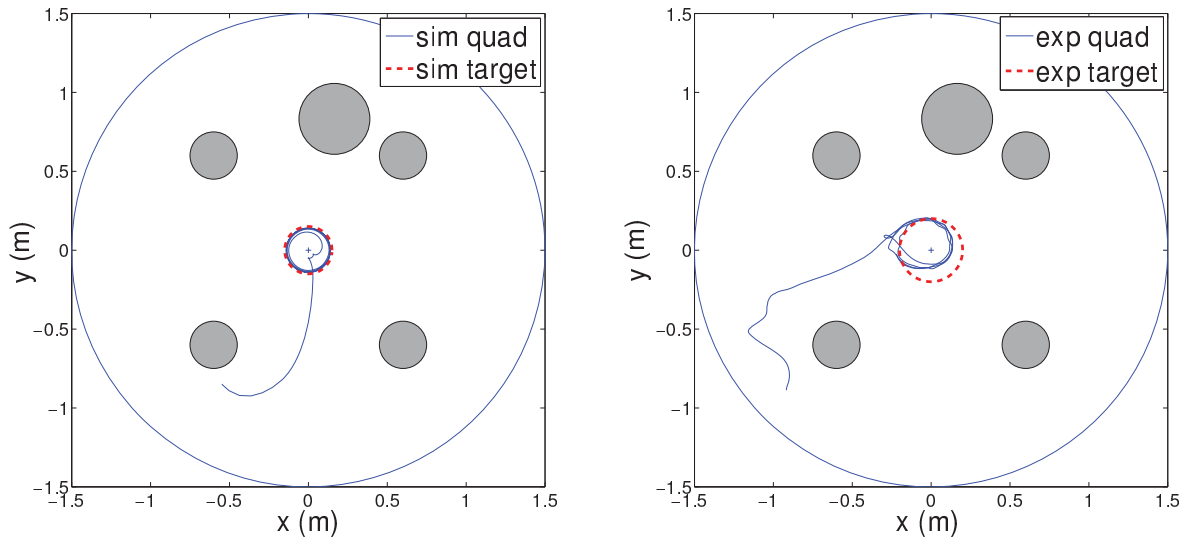


**Figure 7.9:** Simulation (left): a target is circling the origin along a thick red dashed path, and a quadrotor starting from behind an obstacle follows a thin blue solid path as it converges to its target and follows it around in circles. Experiment (right): the same scenario is repeated with a real quadrotor in an experiment where it tracks a simulated target following another circular path with slightly larger radius; here, the path of the quadrotor is marked with a thin solid blue line, while the motion of its target is shown in thick dashed red.

Now controller (5.5) is applied on an AscTec Hummingbird quadrotor, which is supposed to move in a physical environment identical to that of Figure 7.9, with the difference that obstacle boundaries are virtual. The target is now following a circular path of radius 0.2 m, with a linear speed of 0.1 m/s. The path followed by the real quadrotor as it tracks its target is shown in Figure 7.9 as a dashed-dot curve. While

not evident in Figure 7.9, the unmodeled (assumed very fast) attitude dynamics of the quadrotor, affect its tracking performance.<sup>1</sup> The difference in performance between simulation and experiment, attributed here to the unmodeled attitude dynamics, is shown more clearly in Figures 7.10 and 7.11. Figure 7.10 shows the distance between the sensor platform and its target over time, in dashed (red) curve for the simulated robot case, and in solid (blue) curve for the actual hardware. The desired distance (clearance) is set at 50 mm, and it is shown as a horizontal (blue) dashed line. Although in both cases, the distance converges to the desired one, the real quadrotor maintains a larger distance error.

The reason for the tracking discrepancy in the experimental tests is more apparent in Figure 7.11. By ignoring the attitude dynamics, one essentially assumes that the desired roll and pitch angles are attained instantaneously. Figure 7.11 shows that while the attitude dynamics may be indeed fast, their converging time is not infinitesimal compared to that of position dynamics. A lag in achieving the desired pitch angle, propagates into a lag in linear acceleration, which is then integrated into a velocity error.

## 7.5 Laser-emulated Radiation Emissions

The experiment detailed in this section validates the utility of the error probability bounds through experimentation with custom-built hardware that emulates radioactivity on the plane without imposing any health risks. In particular, the statistics of radioactive decay as perceived by a Geiger counter are emulated using a novel device that emits laser beams in random directions on a horizontal plane, triggered at random times that are exponentially distributed. Of course, nuclear emission is truly three-dimensional and a planar emulation system cannot fully and faithfully capture the nature of this phenomenon. It has been shown, however, that along a fixed plane

---

<sup>1</sup> In fact, the robot’s manufacturer does not give direct access to the attitude control loops; the roll-pitch-yaw angles are treated as control setpoints by the default firmware on this robot.

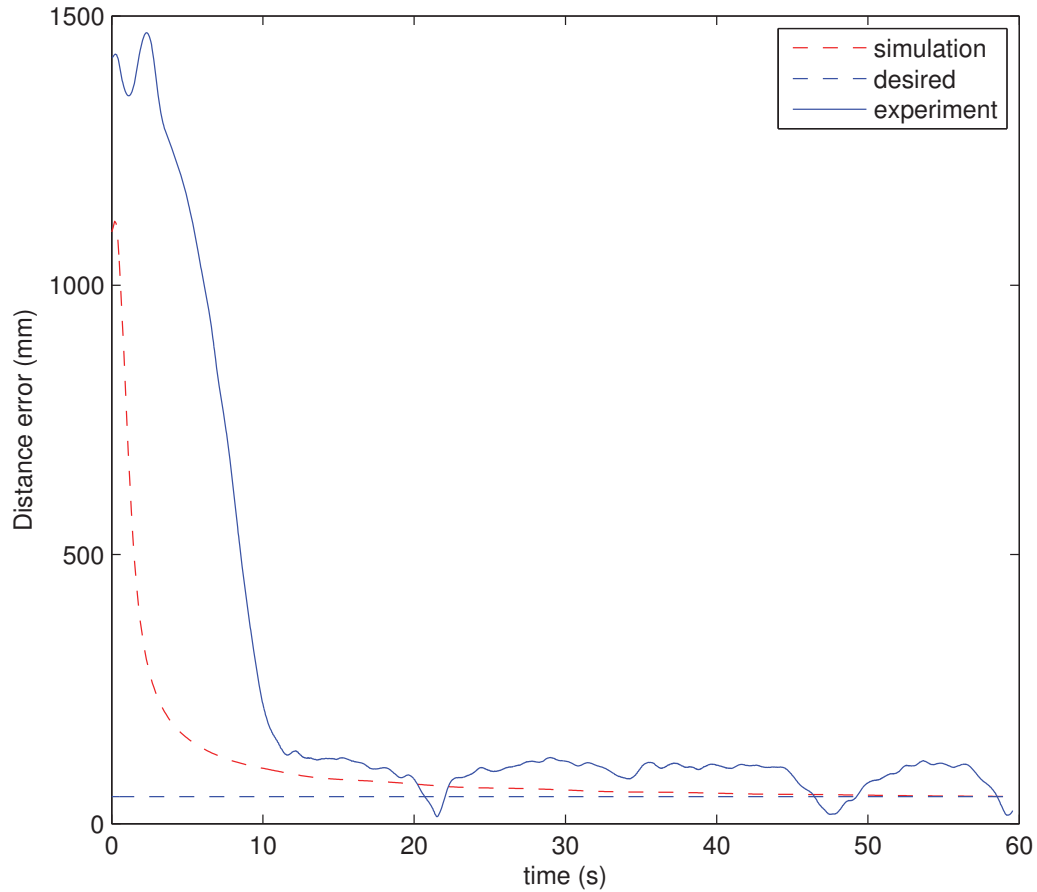


**Figure 7.10:** The distance between target and the quadrotor in the simulation and experimental cases. The horizontal (blue) dashed line is the desired distance to target, while the solid (blue) is the actual distance between target and quadrotor during experiment, and the (red) dashed curve is the distance to the simulated platform.

of motion for the detector, the statistics of the events incident to the sensor can be adequately approximated. Details of the emulation device design and validation against real radiation measurements from a Geiger counter are documented elsewhere [29].

### 7.5.1 Laser-emulation: Experimental Setup

The experimental setting is shown in Figure 7.12. In this setting, the laser device is mounted on top of the white round mobile robot, acting as a surrogate source

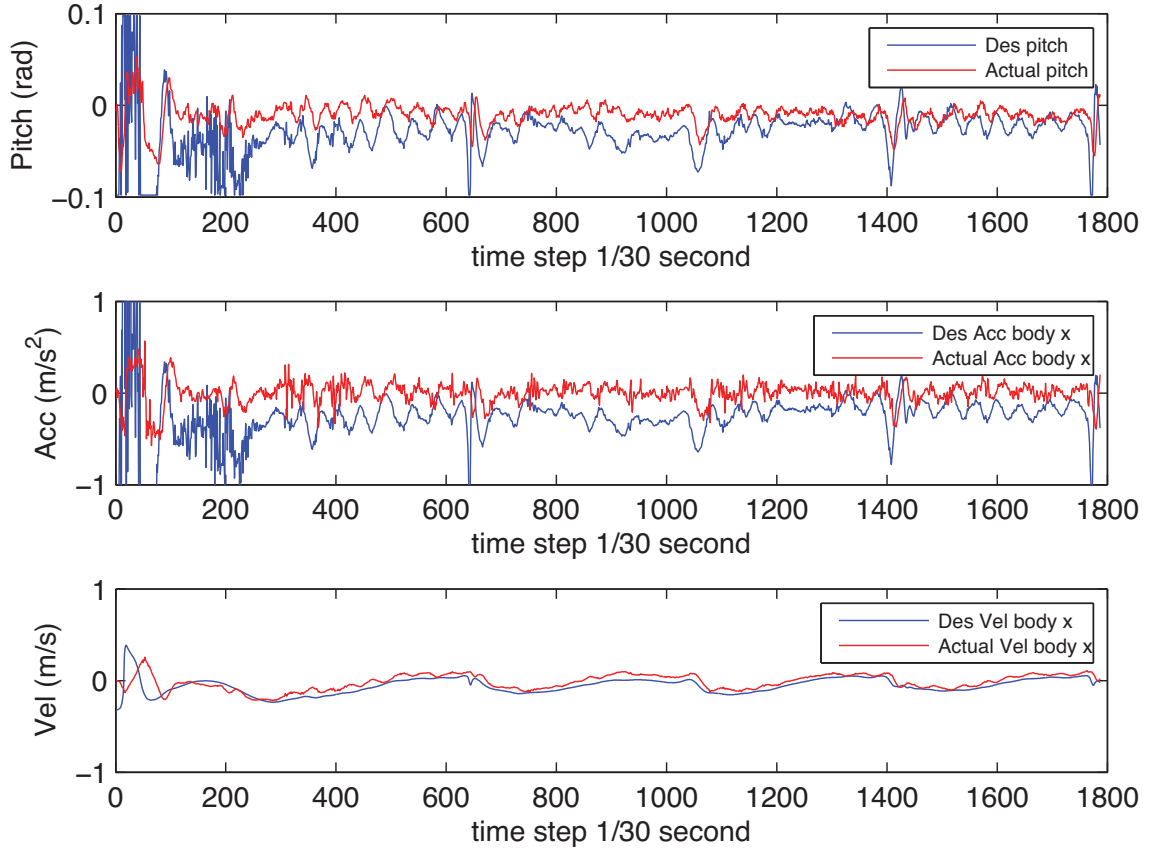


**Figure 7.11:** Comparison between the desired and the actual pitch angle during the flight, and its effect on linear position dynamics.

of radiation. The sensors are realized via long rectangular boxes containing light detectors, configured to pick up a laser emission. There are four static sensors, arranged along the same line at the edge of the gray floor mat, and a single mobile sensor, mounted on top of a black square mobile robot, which is steered along a line parallel to that of the static sensors, and at the same distance with respect to the target.

The stationary sensors 1, ..., 4 are located at spatial coordinates  $(0, 0)$ ,  $(0.5, 0)$ ,  $(1.5, 0)$ ,  $(2.5, 0)$ , respectively, with coordinates measured in m. In Figure 7.12, the leftmost sensor in the upper left corner is sensor 1. The mobile sensor, sensor 5, is initially at rest at location  $(3, 1)$ . The source is initialized at coordinates  $(3.0, 0.5)$ , and starts moving parallel to the  $x$  axis, in a negative direction, from sensor 4 toward

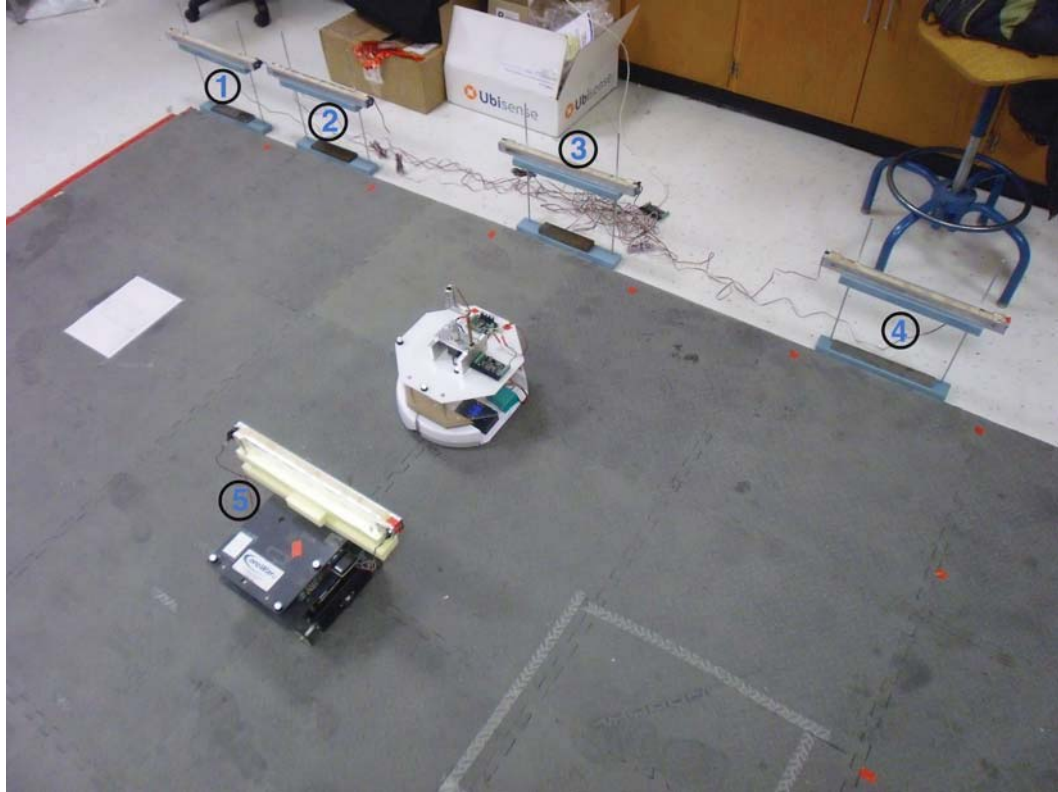


**Figure 7.12:** The experimental setup that realizes a one dimensional detection scenario. In the static network tests, only sensors 1, . . . , 4 are used, while in the mobile network tests we utilize the spatial symmetry of the configuration to replace the static sensor 1 with the mobile sensor 5. Sensor width is 0.4 m.

sensor 1, with a constant speed of 0.03 m/s. The source’s intensity is a constant  $a = 2$  cps, while the background rate is at  $\beta = 0.167$  cps. The time interval for the detection is a window of 100 s, and the acceptable probability of false alarm is set at  $\alpha = 10^{-3}$ .

Note that in the two dimensional setting of Figure 7.12, the source intensity as perceived by a sensor is no longer inversely proportional to the square of the distance, as typically considered for the three-dimensional case [47]. Now the solid angle in  $\chi$  scales linearly with the distance [29]; in both cases, the perceived intensity is in fact inversely proportional to the *solid angle* associated with the volume between the source and the sensor’s surface. This solid angle scales with the square of the radius in three dimensions, but linearly on the plane.

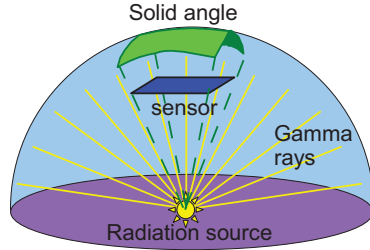


**Figure 7.13:** The perceived intensity at the sensor is inversely proportional to the solid angle. In 3D, this angle scales with the square of the distance; on the plane—as in the case of this experiment—it scales linearly with the distance.

In the planar case of Figure 7.12, the solid angle  $\phi$  is calculated as a function of the sensor’s instantaneous relative position with respect to the target, and then the perceived intensity  $\nu$  is obtained as  $\nu = \frac{a\phi}{2\pi}$ . This intensity varies between 0.007 cps and 0.24 cps, which is comparable to the background rate of  $\beta = 0.167$  cps.

To simulate that uniform background rate—it cannot be reproduced by the laser device, for it would experience the same attenuation as the source signal—the count output of each sensor is superimposed externally with a temporal sequence of samples drawn from a Poisson distribution with mean  $\beta$ . We can thus know what percentage of the total average count rate is attributed to the source, but the detection algorithm is unaware of this; instead, it is presented with the count sum, and this is what it uses to compute the likelihood ratios.

### 7.5.2 Results and Discussion

To assess the contribution of mobility to the accuracy of detection, experiments are conducted for two cases: one in which the data collected from four static sensors 1, . . . , 4 are utilized to make a decision, and one in which static sensor 1 is replaced with the mobile sensor 5 so that the total number of sensors is constant and equal to four in both cases; see Figure 7.12.

Thirty-two different runs are performed. For each run, finite-interval LRTs with a range of different threshold values, from  $10^{-4}$  to  $10^6$ , are conducted. The error

probabilities for each threshold value are estimated as empirical averages over the set of all 32 LRTs conducted with that same threshold value.

Figure 7.14 compares the empirical average of the probability of miss for LRTs conducted over a range of different threshold values for 32 different experimental trials with 4 static sensors, against Monte Carlo estimates of this probability, and the proposed Chernoff bound. Figure 7.14 indicates that empirical averages from the experiments with the static network remain close to Monte Carlo estimates, suggesting an agreement between experimental and simulation results. In this context, the Chernoff bounds are shown to be tight in the region of low thresholds, while becoming more conservative for higher threshold values.

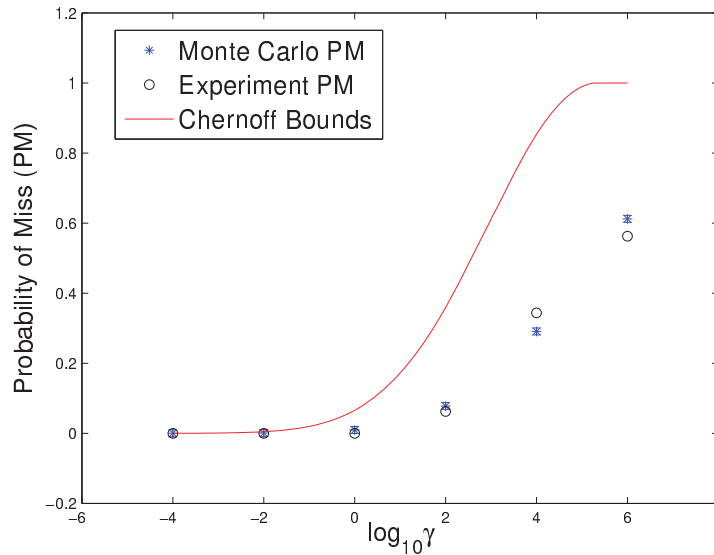


**Figure 7.14:** Comparison between Chernoff bound, Monte Carlo and Experiment estimates for probability of miss in cases when all sensors are static. The bars show the 95% confidence interval of estimates of probabilities using both Monte Carlo and experimental data.

Table 7.1 lists the detection results over a set of the 32 static and mobile sensor network configuration trials, when the optimal controls  $\mathbf{u}^*$ , and optimal thresholds  $\gamma(\mathbf{u}^*)$  are utilized. The third column in Table 7.1 lists the computed Chernoff bounds on the probability of missed detection, while the two rightmost columns document the

**Table 7.1:** Optimal LRT parameters, and detection results for the static and mobile sensor network configurations

network topology	optimal threshold	Chernoff bound	missed sources	empirical probability
static	540.70	0.541	4	0.125
mobile	27.98	0.028	0	–

frequency of missed detection errors. For the case of the mobile sensor, the resulting threshold is much smaller compared to that of the static case. The Chernoff bound on the probability of missed detection is lower than 3%, and agrees with experimental data where the source is detected in all 32 tests. In contrast, the static case Chernoff bound (54.1%) is conservative compared to the actual error probability results (12.5%), due to the inherent conservativeness of the bounds. Nonetheless, Table 7.2 that reports the SNR for the two cases computed using the same expression used in Chapter 3, suggests a clear three-fold improvement in the signal-to-noise ratio due to sensor mobility, corroborating the simulation results of Chapter 3.

**Table 7.2:** SNR of individual sensors in the experimental tests, for static and mobile sensor network configurations

network topology	SNR 1	SNR 2	SNR 3	SNR 4	SNR 5
static	<b>1.25</b>	1.79	2.03	1.78	–
mobile	–	1.79	2.03	1.78	<b>3.78</b>

## 7.6 Detection of Vaseline Beads Mounted on Mobile Robot

The setup of the experiment where physical sensor platforms are tracking and identifying radioactive sources is depicted in Figure 7.15. An AscTec Hummingbird quadrotor and an iCreate wheeled mobile robot are fitted with Geiger counters, and are tasked to detect the presence of a very weak radiation source composed of a small number of Vaseline glass (containing Uranium oxide) beads. This source is carried

around on a miniature 3D-printed wheg-leg crawling robot, remotely controlled by a human operator. This source is so weakly radioactive, that its perceived intensity drops at a level of less than 10% of ambient background just after 17 cm away. The background radiation level observed by our two sensors during the experiments, ranges from 9.5 to 12.5 counts per minute. In order for detection to be feasible within a time window of 3 minutes, the two sensor platforms have to get close to the target (source), at a distance of less than 10 cm.

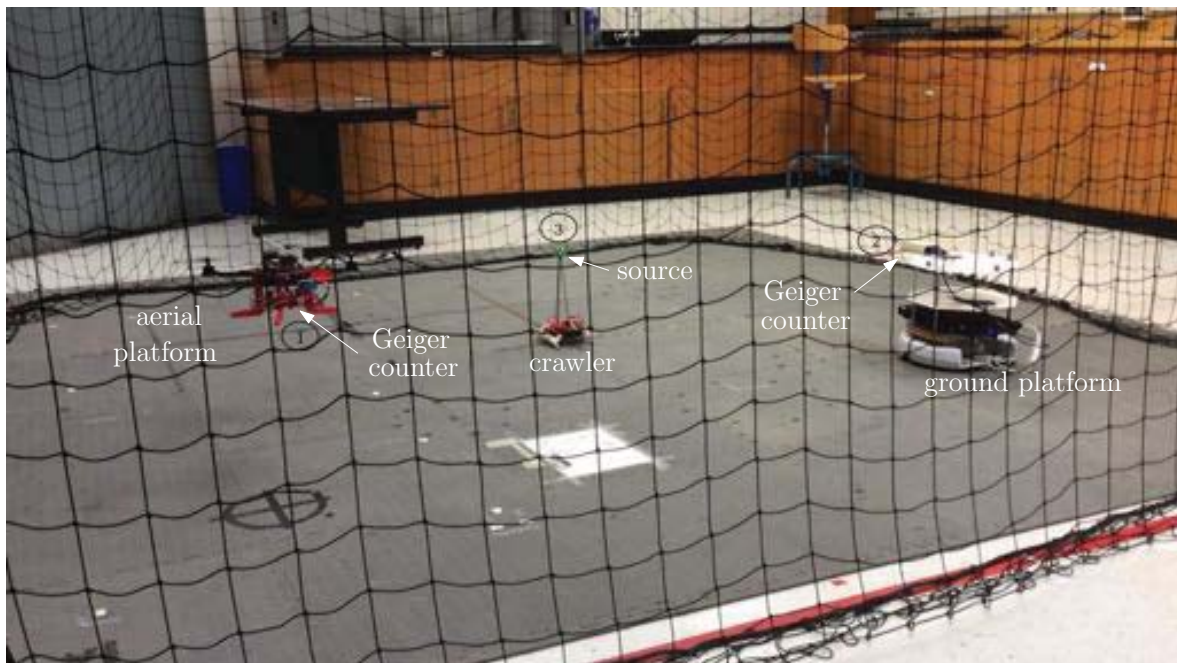


**Figure 7.15:** The radiation detection experiment. Geiger counters are carried by an aerial platform (1) and a ground platform (2), while the weak radiation source (3) moves with a remotely controlled crawling robot.

The experiment evolves in the same virtual obstacle workspace as the test shown in Figure 7.9. Here, the outer workspace boundary is at a radius of 150 cm around the origin of the inertial coordinate frame. The four small (virtual) interior obstacles have a radius of 15 cm, while the single bigger one is of 22.5 cm radius. During the detection task, the two mobile sensor platforms gather radiation count information using their on-board Geiger counters, and at the end of the 3 minute observation window, they

transmit wirelessly their computed statistics to a central computer that performs the likelihood ratio test. The outcome of this test is a decision as to whether the target is radioactive.

Given that for the particular sensor geometry utilized, the cross-section coefficient  $\chi_i$  is negligible compared to the distance between sensor and source, the perceived source intensity can confidently be approximated as  $\nu_i = \frac{\chi_i a}{2\chi_i + r_i^2} \approx \frac{a_i}{r_i^2}$ , so that the actual value of the sensor cross-section coefficient is no longer required, and the average of the counts recorded in the unit of time becomes  $b_i + \frac{a_i}{r_i^2}$ . Figure 7.16 confirms the validity of this approximation, and illustrates why it is impractical to attempt detection of weak moving radiation sources using stationary counter networks.

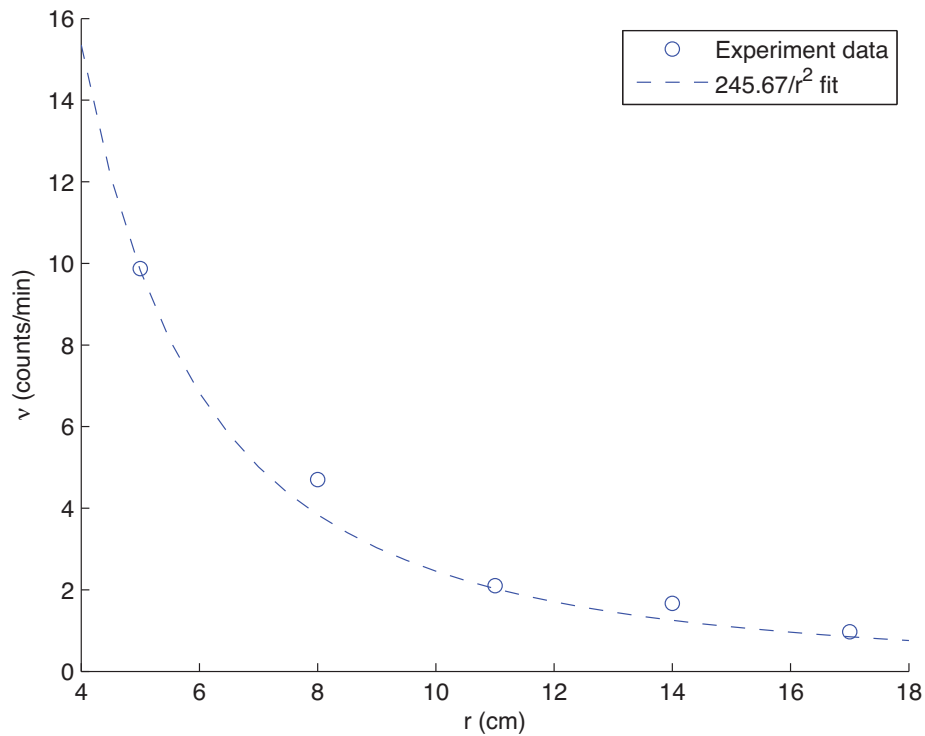


**Figure 7.16:** The perceived source intensity  $\nu_i$  follows an  $r^2$  fall-off. Circles mark radiation measurements made by the Geiger counter mounted on the quadrotor, and the dashed curve corresponds to a  $\frac{a_i}{r_i^2}$  fit.

Thus coming as close to the target as possible is key to being able to detect weak

radioactive material in motion. The controller constructed closes the distance between sensor and source and maintains it at a desired small set-point during the detection time window. A motion capture system is used to obtain ground truth information and provide initial target position information to the sensor platforms, while a camera on board the quadrotor uses visual feedback to localize the target while in motion. The target trajectory information obtained through the on-board sensors contains a significant amount of noise; however, the noise in the signal does not prevent the platforms from tracking their target reasonably well (Figure 7.17).

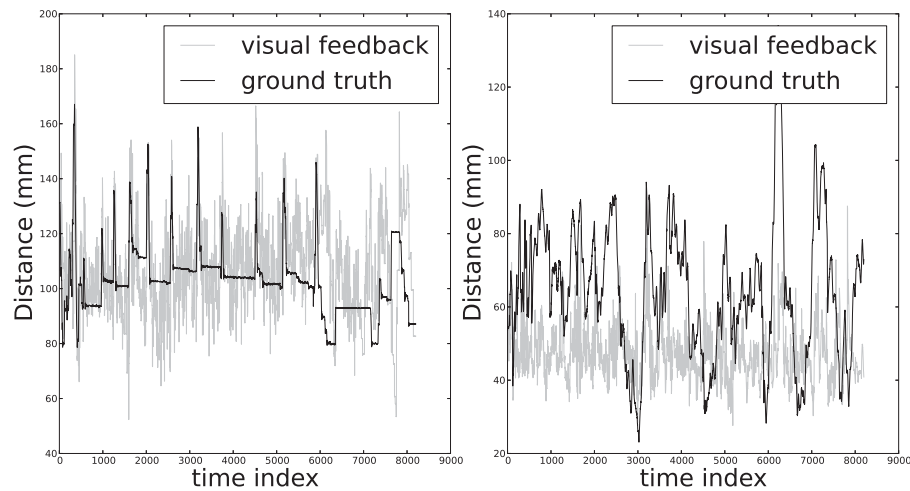


**Figure 7.17:** Distance between sensor platforms—Left ground, Right aerial—and target maintained based on visual feedback against ground truth. The unit of measurement on the time index axis is 0.02 seconds.

Figure 7.18 shows the paths of the two platforms and their target, moving amidst the virtual obstacles during one of the radiation detection experiments. The dashed (blue) line corresponds to the (projected on the horizontal plane) path of the aerial platform, which returns to the initial landing spot at the end of the 3 minute tracking window. The dotted (red) curve marks the path of the wheeled ground platform, while the solid (green) quivering path is that of the source, which wavers somewhat being at the end of a pole fixed on the crawling legged vehicle. Due to the noisy nature of the visual target motion feedback information and the sensitivity of any potential

field reference close to an equilibrium configuration, once the platforms achieved the 10 mm target distance objective using (5.5), they switched to a local PID controller for tracking.

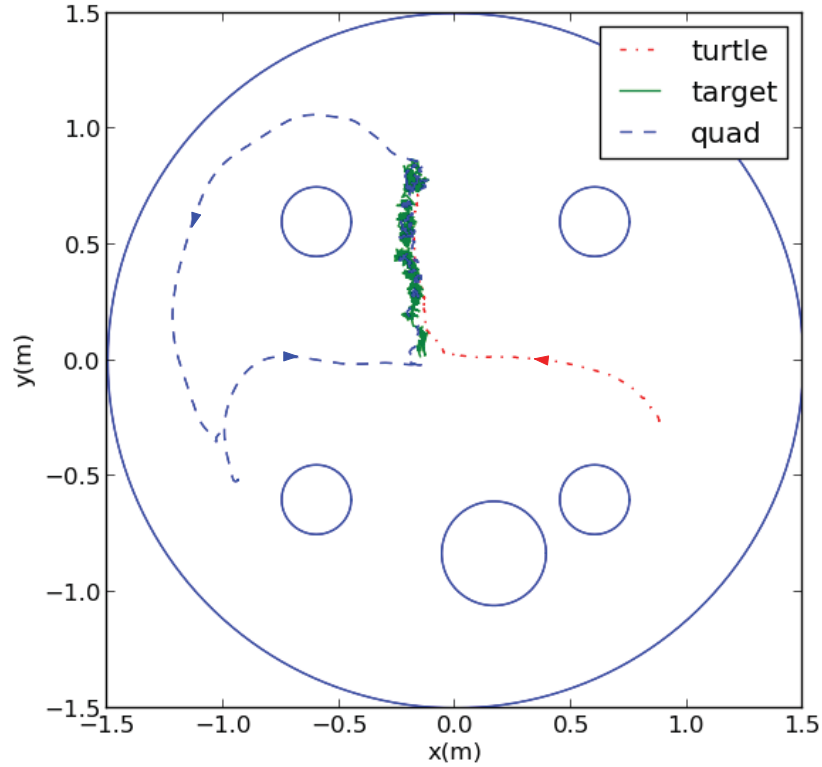


**Figure 7.18:** Superimposed paths of sensor platforms and target during a single radiation detection trial

Fifty radiation detection trials like the one shown in Figure 7.18 were conducted, and likelihood ratio tests were performed for a maximum false alarm rate of 1.2 %. Out of the 50 different trials, half were performed with a radiation source on the target, and the other half without it. In all cases where the source was not present on the target, the likelihood ratio test concluded correctly that the target was benign. Out of the 25 cases where the target was carrying a source, one was reported as a false negative, while in the remaining 24 the target was classified correctly.<sup>2</sup>

<sup>2</sup> This type of behavior is expected, since detection tests of this nature are skewed conservatively on the side of keeping false alarm rates low. The rationale is that if this

## 7.7 Conclusion

This chapter demonstrates the advantage of having mobile sensor in detecting weak mobile radioactive sources. It is also evident that the navigation function based controller can drive the quadrotor and the wheeled robot in cluttered environments with the help of the low level controllers designed for these two platforms. Yet, conducting these experiments requires comprehensive sensory feedback, such as Vicon motion capturing and camera visual feedback that are introduced in the Section 7.1. As a possible extension, the possibility of driving robots to field extremum with limited sensory feedback in next chapter.

---

is not the case, then human operators will tend to ignore the detection systems' report.

## Chapter 8

### SOURCE SEEKING WITH LIMITED SENSOR INFORMATION

In this dissertation, techniques for improving radiation detection performance by exploiting sensor mobility are presented. Yet, to implement our proposed strategy in practice as shown in Chapter 7, a comprehensive sensory system is required including both global localization (motion capture, GPS, etc) and optical feedback (camera, laser, etc). A possible extension to the work presented in this dissertation is to explore the possibility of source seeking with limited sensory information.

Assume a ground wheeled robot is available; it is capable of measuring its forward and turning velocity using encoders, and its heading direction using compass. This robot carries a sensor which measures the strength of some signal field, such as light intensity, radio signal strength, or radiation intensity. Consider now this mobile sensor platform deployed in an environment filled with obstacles.

If the robot follows the gradient of the field deterministically, it may be easily trapped in some non-convex boundary of obstacles. But if some randomness is injected into both the motion of the robot and its interaction with obstacle boundaries, there should be a chance for the robot to get away from such trapped position by drifting and bouncing randomly. In this chapter, such randomness behavior is modeled and preliminary study is performed to find the bounds on the probability of the sensor platform reaching field extremum.

#### 8.1 Modeling Boundary Reflection Events

Let the robot move in a constrained space  $\mathcal{W} \subset \mathbb{R}^2$ . The state space representation of the robot consists of  $(x, y, \theta)$ , where  $(x, y)$  represents the robot's position in  $\mathbb{R}^2$ ,

and  $\theta$  represents the robot's heading angle between its forward direction and global  $x$  axis.

Assume that when the robot is operating in the interior of  $\mathcal{W}$ , its kinematics is adequately described in the form of (5.6):

$$\dot{x} = v \cos \theta \quad , \quad \dot{y} = v \sin \theta \quad , \quad \dot{\theta} = \omega \quad .$$

The robot may come into contact with the free space boundaries. Assume that each time the robot hits the boundary of  $\mathcal{W}$ , the robot will break with probability  $P_b$ . If the robot doesn't break, it will bounce back to a state that is no further than  $\epsilon$  away from the hit point  $x_h \in \partial\mathcal{W}$  while remaining in  $\mathcal{W}$ . The set of possible bounce back positions can be written as  $B_{x_h}(\epsilon) \cap \overset{\circ}{\mathcal{W}}$ . Since our goal is to reach certain closed subset  $\mathcal{S}_G \subset \overset{\circ}{\mathcal{W}}$ , the robot will terminate its motion once it hits the boundary of  $\mathcal{S}_G$ . Now the system can be modeled as a stochastic hybrid system:

Let  $Q = \{1, 2, 3, 4\}$  be the discrete states of the hybrid system. The state 1 means the robot is in the normal operation mode subject to unicycle kinematics (5.6). State 2 means a collision event occurs and the robot is broken after colliding with workspace boundary. State 3 is associated to a collision event in which the robot remains intact after colliding with workspace boundary. State 4 means the robot reaches the goal set.

Let  $\mathcal{X} = \{\mathcal{X}_1, \mathcal{X}_2, \mathcal{X}_3\}$  be a partition of the continuous state space of the hybrid system. Set  $\mathcal{X}_1 = W \setminus \overset{\circ}{\mathcal{S}}_G$ , represents the workspace excluding the interior of the goal set.  $\mathcal{X}_2 = \partial\mathcal{W}$ , represents the workspace boundary.  $\mathcal{X}_3 = \partial\mathcal{S}_G$ , represents the goal set boundary.

Then state space of the stochastic hybrid system can be represented as a tuple  $\bar{\mathcal{X}} = Q \times \mathcal{X}$  with its flow and jump transitions defined as following:

- When the robot's discrete state is 1:
  - If  $(1, x) \in (1, \mathcal{X}_1)$ , the free space away from the boundaries, the system evolves according to (5.6).

- If  $(1, x) \in (1, \mathcal{X}_2)$ , meaning that it collides with the boundary, it may either break and the hybrid state jumps to  $(2, x)$  with probability  $P_b$ , or remain intact, in which case the hybrid state jumps to  $(3, x)$ .
- If  $(1, x) \in (1, \mathcal{X}_3)$ , which means the robot reaches goal boundary, the hybrid state jumps to  $(4, x)$  with probability 1.
- When the system is at  $(2, x) \in (2, \mathcal{X}_2)$ , it immediately jumps back to  $(2, x)$  with probability 1, making  $(2, x)$  an absorbing state.  $(2, x)$  models the robot's failure state.
- When the system is at  $(3, x) \in (3, \mathcal{X}_2)$ , it immediately jumps to a random point that's distributed over the set  $(1, \mathcal{B}_x(\epsilon) \cap \mathring{\mathcal{W}})$  with probability 1.  $(3, x)$  models the robot bounce state.
- When the system is at  $(4, x) \in (4, \mathcal{X}_3)$ , it immediately jumps to  $(4, x)$  again with probability 1, making  $(4, x)$  an absorbing state.  $(4, x)$  models the robot's success in reaching the goal.
- All states in  $(\{2, 3\} \times \{\mathcal{X}_1, \mathcal{X}_3\}) \cup (4 \times \{\mathcal{X}_1, \mathcal{X}_2\})$  are not reachable.

Thus the jump transition probability  $R$  is:

$$\begin{aligned}
R((1, x \in \mathcal{X}_2), (2, x)) &= P_b \\
R((1, x \in \mathcal{X}_2), (3, x)) &= 1 - P_b \\
R((1, x \in \mathcal{X}_3), (4, x)) &= 1 \\
R((2, x \in \mathcal{X}_2), (2, x)) &= 1 \\
R((3, x \in \mathcal{X}_2), (1, y \in \mathcal{B}_x(\epsilon) \cap \mathring{\mathcal{W}})) &= f_{\text{bounce}}(y \in \mathcal{B}_x(\epsilon) \cap \mathring{\mathcal{W}}) \\
R((4, x \in \mathcal{X}_3), (4, x)) &= 1
\end{aligned}$$

where the  $f_{\text{bounce}}$  is a probability density function over the set  $B_x(\epsilon) \cap \mathring{\mathcal{W}}$ , and the jumps always happen at  $\partial\mathcal{X}_i, i \in Q$ . The underlying Markov Chain that represents the transition between different discrete states is illustrated in Figure (8.1). Notice

that the transition probability from discrete state 2 to discrete state 1 is 1 because the integration of  $f_{\text{bounce}}$  over  $B_x(\epsilon) \cap \mathring{\mathcal{W}}$  is 1.

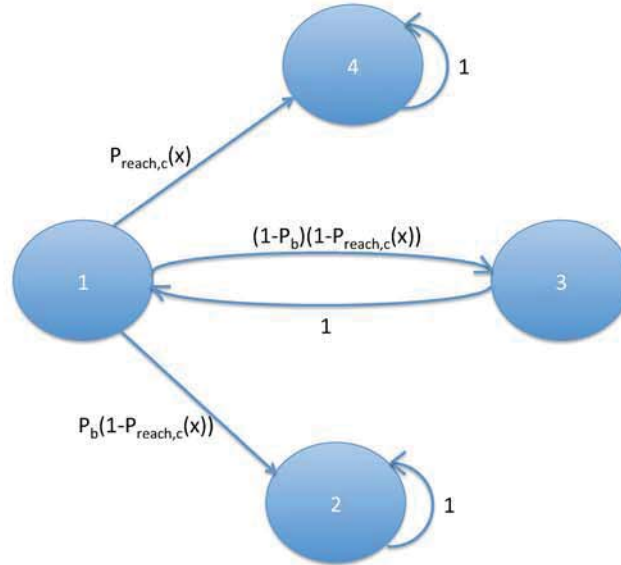


**Figure 8.1:** Markov Chain for Boundary Bouncing Robot Mode.  $x$  is the robot's continuous state when starting in  $(1, \mathcal{X}_1)$ . The jumps from  $(1, \mathcal{X}_1)$  always happen on  $\partial\mathcal{X}_1 = \mathcal{X}_2 \cup \mathcal{X}_3$ .

## 8.2 Lower Bound on Probability of Reaching Field Extremum

Our goal is to localize a source at  $\mathcal{S}_G$  within workspace  $\mathcal{W}$ . Thus it becomes a reachability problem where one seeks to estimate  $P_{\text{reach}}(x_0)$ : the probability of the robot being absorbed on the boundary of  $\mathcal{S}_G$  when starting from  $(1, x_0) \in (1, \mathcal{W})$ .

Let the probability  $P_{\text{reach},c}(x)$  denote the probability that starting from  $x \in \mathcal{X}_1$ , robot reaches  $\mathcal{X}_3$  without jumps.

**Assumption 8.2.1** *There exists lower and upper bound  $P_{s_l}, P_{s_u} \in (0, 1)$  for  $P_{\text{reach},c}(x)$ ,  $x \in (\cup_{p \in \partial\mathcal{W}} \mathcal{B}_p(\epsilon)) \cap \mathring{\mathcal{W}}$ .*

**Assumption 8.2.2**  $\mathcal{S}_G \cap \left( \left( \cup_{x \in \partial \mathcal{W}} \mathcal{B}_x(\epsilon) \right) \cap \mathring{\mathcal{W}} \right) = \emptyset$ , meaning that the goal set is not directly reachable by bouncing off workspace boundaries.

**Proposition 8.2.3** *If Assumptions 8.2.1 and 8.2.2 hold and the evolution of the hybrid system observes Markov property, that is the conditional evolution of the future states of the process only depends on present state,  $P_{\text{reach}}(x_0)$  is lower bounded by*

$$P_{\text{reach,c}}(x_0) + \frac{P_{s_l}(1 - P_b)}{1 - (1 - P_{s_u})(1 - P_b)}(1 - P_{\text{reach,c}}(x_0)) .$$

**Proof** Define the set near the boundary in the workspace:  $\mathcal{F}(\epsilon) = \left( \cup_{x \in \partial \mathcal{W}} \mathcal{B}_x(\epsilon) \right) \cap \mathring{\mathcal{W}}$ . Let  $f_{x_0}(x)$  be the probability density function that describes the distribution of points in  $\mathcal{F}(\epsilon)$  where the sample paths starting at  $x_0$  bounce off at, after hitting the boundary  $\partial \mathcal{W}$  once.

$$\begin{aligned} & P_{\text{reach}}(x_0) \\ &= P_{\text{reach}}(x_0, \text{without collisions}) + P_{\text{reach}}(x_0, \text{with collisions}) \\ &= P_{\text{reach,c}}(x_0) + [1 - P_{\text{reach,c}}(x_0)](1 - P_b)P_{\text{reach}}(x_0 | \text{intact after 1 collision}) \\ &= P_{\text{reach,c}}(x_0) + \\ & \quad [1 - P_{\text{reach,c}}(x_0)](1 - P_b) \int_{\mathcal{F}(\epsilon)} P_{\text{reach}}(x | \text{after bouncing once}) f_{x_0}(x) dx \\ & \stackrel{\text{Markov Property}}{=} P_{\text{reach,c}}(x_0) + [1 - P_{\text{reach,c}}(x_0)](1 - P_b) \int_{\mathcal{F}(\epsilon)} P_{\text{reach}}(x) f_{x_0}(x) dx \quad (8.1) \end{aligned}$$

$f_{x_0}(x)$  is determined by both the flow dynamics in the hybrid system that determines where the robot hits the boundary, and the jump transition that determines where the robot would bounce to after the collision. In general, obtaining the explicit closed-form of  $f_{x_0}(x)$  is intractable.

Yet, with Assumption 8.2.1, the integrand in the integral term in (8.1) can be lower bounded. For  $x_b \in \mathcal{F}(\epsilon)$ :

$$P_{\text{reach}}(x_b) = P_{\text{reach,c}}(x_b) + [1 - P_{\text{reach,c}}(x_b)](1 - P_b) \int_{\mathcal{F}(\epsilon)} P_{\text{reach}}(x) f_{x_b}(x) dx \quad (8.2)$$

$$\geq P_{s_l} + (1 - P_{s_u})(1 - P_b) \int_{\mathcal{F}(\epsilon)} P_{\text{reach}}(x) f_{x_b}(x) dx . \quad (8.3)$$

Now plug (8.3) into (8.1), we can obtain:

$$\begin{aligned}
P_{\text{reach}}(x_0) &\stackrel{(8.3)}{\geq} P_{\text{reach,c}}(x_0) + [1 - P_{\text{reach,c}}(x_0)](1 - P_b) \\
&\quad \int_{\mathcal{F}(\epsilon)} \left[ P_{s_l} + (1 - P_{s_u})(1 - P_b) \int_{\mathcal{F}(\epsilon)} P_{\text{reach}}(s) f_{x_b}(s) \, ds \right] f_{x_0}(x) \, dx \\
&= P_{\text{reach,c}}(x_0) + [1 - P_{\text{reach,c}}(x_0)](1 - P_b) P_{s_l} + \\
&\quad [1 - P_{\text{reach,c}}(x_0)](1 - P_b)^2 (1 - P_{s_u}) \int_{\mathcal{F}(\epsilon)} \left[ \int_{\mathcal{F}(\epsilon)} P_{\text{reach}}(s) f_{x_b}(s) \, ds \right] f_{x_0}(x) \, dx \\
&\stackrel{\text{repeat}(8.3)}{\geq} P_{\text{reach,c}}(x_0) + [1 - P_{\text{reach,c}}(x_0)](1 - P_b) P_{s_l} \\
&\quad [1 + (1 - P_b)(1 - P_{s_u}) + (1 - P_b)^2 (1 - P_{s_u})^2 + \dots] \\
&= P_{\text{reach,c}}(x_0) + \frac{P_{s_l}(1 - P_b)}{1 - (1 - P_{s_u})(1 - P_b)} (1 - P_{\text{reach,c}}(x_0))
\end{aligned} \tag{8.4}$$

### 8.3 Conclusion and Next Steps

With Proposition 8.2.3, a lower bound on the  $P_{\text{reach}}$  can be obtained without finding the probability distribution  $f_{x_b}(x)$ , or solving (8.1) and (8.2) explicitly. The only prerequisite for finding such lower bound is to find the lower and upper bounds  $P_{s_l}$  and  $P_{s_u}$ . This corresponds to solving a reachability problem for the continuous part of the hybrid system (flow dynamics). Yet, the result may not always be very informative, as the  $P_{s_l}$  is likely to be zero if the environment contains convex shapes—this cancels the bouncing related terms  $(P_b, P_{s_l}, P_{s_u})$  in the lower bound (8.4).

A more interesting scenario arises when the robot's kinematics [57] or the controller [40, 41] are randomized [40, 41]. The next step would be solving the reachability problem with these stochastic process and possibly compare the bound given in Proposition 8.2.3 with the reachability result that from analyzing the SHS that includes both stochastic flow dynamics and random jumps [10, 62, 63].

## Chapter 9

### CONCLUSIONS AND FUTURE DIRECTIONS

This dissertation targets the problem of improving the reliability of the decision making process by exploiting sensor mobility, when testing whether a target in transit is radioactive or not.

Thanks to the existing analytic bounds on the probabilities of making mistakes during the test, an optimal control problem can be formulated to minimize these bounds. This problem is subsequently solved to obtain the optimal control policy as well as the threshold for the testing process, both numerically and analytically using Pontryagin’s Maximum Principle. Solving this optimal control problem establishes explicit connections between sensor trajectories and radiation testing performance.

The analytic solutions reveal that the best strategy is to move the sensors towards the target as fast as possible. Thus when planning sensor motions, instead of minimizing the error bounds, which are complex functions of sensor trajectories, the goal is simplified to reaching the target in shortest time possible. Yet in a cluttered environment, tracking a mobile target without collision with both obstacles and the target still present challenges that may involve rapid replanning and compromising optimality. In this dissertation, a modified navigation function based controller is proposed, which—instead of rushing the robot towards the target at maximum speed and likely leading to collisions or overshoots—follows a more gradual gradient of a virtual potential functions. This controller suits the purpose of bringing sensors towards the target in practice and guarantees obstacle avoidance as well as convergence to time-varying target set.

Thanks to its analytic structure, the navigation function based controller can be tailored to different robot platforms easily, regardless that it is originally designed

for single integrator model. This dissertation designs two adaptive controllers for the quadrotor and the wheeled robot respectively, and demonstrates that these controllers combined with navigation function based planner is well behaved on physical platforms with much more complex dynamics compared to single integrator model through simulations and experiments.

In a laser-emulated radiation detection experiment, a comparison between using solely static sensors, and a combination of static and mobile sensors indicates that the addition of sensor mobility could greatly improve the detecting performance in terms of reducing error probabilities. In subsequent experiments, sensor platforms including one quadrotor and one wheeled robot were used to track a mobile crawling robot and decide whether it contained the extremely weak radioactive source (Vaseline beads). The promising results validates the previously proved detection strategy.

The limitation of the proposed radiation detection methodology is that although it is shown that a fast gradient descend type controller is suitable for the task, it requires localization information of both the mobile sensor platforms and the target. Yet in some cases, there might be difficulty in obtaining these information and a possible solution is to conduct a gradient descend on the signal strength field rather than the virtual potential field. It is probably that in cluttered environments, collisions would be unavoidable when this type of gradient descend controller is in effect. These collision events can be captured using stochastic hybrid system model, and by analyzing the underlying Markov process, preliminary results on the success rate of the converging to field extremum shows relation between the success rate and the randomness of the sensor motion. The accurate estimation of the success rate of a single experiment can help deciding the total number of repetitions needed to guarantee the success rate above given level. Thus one can decide how many robots would be needed to cover certain space so that reliable detection result can be obtained. This is of practical importance and can be a direction to future research.

## BIBLIOGRAPHY

- [1] X. Alameda-Pineda and R. Horaud. A geometric approach to sound source localization from time-delay estimates. *IEEE/ACM Transactions on Audio, Speech, and Language Processing*, 22(6):1082–1095, June 2014.
- [2] Randal C. Archibold and R. Gladstone. Truck With Lethal Load Is Recovered in Mexico. *The New York Times*, 2013 Dec. 5 pp. A12, Dec. 5 2013.
- [3] N. Ayanian, V. Kallem, and V. Kumar. Synthesis of feedback controllers for multiple aerial robots with geometric constraints. In *IEEE/RSJ International Conference on Intelligent Robots and Systems*, pages 3126–3131, San Francisco, California, Sept. 2011.
- [4] S. Azrad, F. Kendoul, D. Perbrianti, and K. Nonami. Visual servoing of an autonomous micro air vehicle for ground object tracking. In *IEEE/RSJ International Conference on Intelligent Robots and Systems*, pages 5321–5326, St. Louis, USA, 2009. ID: 1.
- [5] S. Azuma, Mahmut Selman Sakar, and G.J. Pappas. Stochastic source seeking by mobile robots. *IEEE Transactions on Automatic Control*, 57(9):2308–2321, Sept 2012.
- [6] David A. Benson, Geoffrey T. Huntington, Tom P. Thorvaldsen, and Anil V. Rao. Direct trajectory optimization and costate estimation via an orthogonal collocation method. *Journal of Guidance Control and Dynamics*, 29(6):1435–1440, 2006.
- [7] Pierre Brémaud. *Point Processes and Queues*. Springer-Verlag, 1981.
- [8] S.M. Brennan, A.M. Mielke, and D.C. Torney. Radioactive source detection by sensor networks. *IEEE Transactions on Nuclear Science*, 52:813–819, 2005.
- [9] W. J. Broad. The Nun Who Broke Into the Nuclear Sanctum. *The New York Times*, 2012 Aug. 11 pp. A1, Aug. 11 2012.
- [10] Manuela L. Bujorianu. Extended stochastic hybrid systems and their reachability problem. In *in Hybrid Systems: Computation and Control, LNCS 2993*, pages 234–249. Springer-Verlag, 2004.

- [11] Manuela L. Bujorianu and John Lygeros. Reachability questions in piecewise deterministic markov processes. In *Proceedings of the 6th International Conference on Hybrid Systems: Computation and Control*, HSCC'03, pages 126–140, Berlin, Heidelberg, 2003. Springer-Verlag.
- [12] Manuela L. Bujorianu and John Lygeros. Toward a general theory of stochastic hybrid systems. In Henk A.P. Blom and John Lygeros, editors, *Stochastic Hybrid Systems*, volume 337 of *Lecture Notes in Control and Information Science*, pages 3–30. Springer Berlin Heidelberg, 2006.
- [13] R.C. Byrd, J.M. Moss, W.C. Priedhorsky, C.A Pura, G.W. Richter, K.J. Saeger, W.R. Scarlett, S.C. Scott, and R.L. Wagner, Jr. Nuclear detection to prevent or defeat clandestine nuclear attack. *IEEE Sensors Journal*, 5:593–609, 2005.
- [14] J.-C. Chin, N.S.V. Rao, D.K.Y. Yau, M. Shankar, Y. Yang, J.C. Hou, S. Srivathsan, and S. Iyengar. Identification of low-level point radiation sources using a sensor network. *ACM Transactions on Sensor Networks*, 7(3), 2010.
- [15] Jren-Chit Chin, Nageswara S. V. Rao, David K. Y. Yau, Mallikarjun Shankar, Yong Yang, Jennifer C. Hou, Srinivasagopalan Srivathsan, and Sitharama Iyengar. Identification of low-level point radioactive sources using a sensor network. *The ACM Transactions on Sensor Networks*, 7:21:1–21:35, 2010.
- [16] Sanjiban Choudhury, Sebastian Scherer, and Sanjiv Singh. Rrt\*-ar: Sampling-based alternate routes planning with applications to autonomous emergency landing of a helicopter. In *IEEE International Conference on Robotics and Automation*, May 2013.
- [17] David T. Cole, Paul Thompson, Ali Haydar Gkto?an, and Salah Sukkarieh. System development and demonstration of a cooperative uav team for mapping and tracking. *The International Journal of Robotics Research*, 29(11):1371–1399, 2010.
- [18] R. A. Cortez, H. G. Tanner, R. Lumia, and C. T. Abdallah. Information surfing for radiation map building. *International Journal of Robotics and Automation*, 26(1):4–12, 2011.
- [19] R.A. Cortez, X. Papageorgiou, H.G. Tanner, A.V. Klimenko, K.N. Borozdin, R. Lumia, and W.C. Priedhorsky. Smart radiation sensor management; radiation search and mapping using mobile robots. *IEEE Robotics & Automation Magazine*, 15(3):85–93, 2008.
- [20] Dimos V. Dimarogonas, Savvas G. Loizou, Kostas J. Kyriakopoulos, and Michael M. Zavlanos. A feedback stabilization and collision avoidance scheme for multiple independent non-point agents. *Automatica*, 42(2):229 – 243, 2006.

- [21] James E. Evans. Chernoff bounds on the error probability for the detection of non-Gaussian signals. *IEEE Transactions on Information Theory*, 20(5):569–577, 1974.
- [22] S. Fetter, T.M. Cochran, L. Grodzins, H.L. Lynch, and M.S. Zucker. Gamma-ray measurements of a soviet cruise-missile warhead. *Science*, 248:828–834, 1990.
- [23] N. R. Gans, Guoqiang Hu, K. Nagarajan, and W. E. Dixon. Keeping multiple moving targets in the field of view of a mobile camera. *IEEE Transactions on Robotics*, 27(4):822–828, 2011. ID: 1.
- [24] Divya Garg, William W. Hager, and Anil V. Rao. Pseudospectral methods for solving infinite-horizon optimal control problems. *Automatica*, 47(4):829 – 837, 2011.
- [25] Divya Garg, Michael Patterson, Camila Francolin, Christopher Darby, Geoffrey Huntington, William Hager, and Anil Rao. Direct trajectory optimization and costate estimation of finite-horizon and infinite-horizon optimal control problems using a Radau pseudospectral method. *Computational Optimization and Applications*, 49(2):335–358, 2011.
- [26] Divya Garg, Michael Patterson, William W. Hager, Anil V. Rao, David A. Benson, and Geoffrey T. Huntington. A unified framework for the numerical solution of optimal control problems using pseudospectral methods. *Automatica*, 46:1843 – 1851, 2010.
- [27] Geoffrey Grimmett and David Stirzaker. *Probability and Random Processes*. Oxford University Press, 1982.
- [28] Ruijie He, Abraham Bachrach, Michael Achtelik, Alborz Geramifard, Daniel Gurdan, Samuel Prentice, Jan Stumpf, and Nicholas Roy. On the design and use of a micro air vehicle to track and avoid adversaries. *The International Journal of Robotics Research*, 29(5):529–546, April 01 2010.
- [29] B.J. Hockman, Jianxin Sun, and H.G. Tanner. Emulating nuclear emissions with a pulsed laser. *IEEE Transactions on Automation Science and Engineering*, 11(1):317–323, Jan 2014.
- [30] J. Huang, D. Millman, M. Quigley, D. Stavens, S. Thrun, and A. Aggarwal. Efficient, generalized indoor wifi graphslam. In *IEEE International Conference on Robotics and Automation*, pages 1038–1043, Shanghai, China, May 2011.
- [31] Donald L. Snyder Joseph L. Hibey and Jan H. van Schuppen. Error-probability bounds for continuous-time decision problems. *IEEE Transactions on Information Theory*, 24(5):608–622, 1978.

- [32] Sertac Karaman and Emilio Frazzoli. Sampling-based algorithms for optimal motion planning. *The International Journal of Robotics Research*, 30(7):846–894, 2011.
- [33] N. Kariotoglou, D.M. Raimondo, S. Summers, and J. Lygeros. A stochastic reachability framework for autonomous surveillance with pan-tilt-zoom cameras. In *IEEE Conference on Decision and Control and European Control Conference*, pages 1411–1416, Orlando, FL, USA, Dec 2011.
- [34] A.V. Klimenko, W.C. Priedhorsky, H. Tanner, K.N. Borozdin, and N. Hengartner. Intelligent sensor management in nuclear searches and radiological surveys. In *Transactions of the American Nuclear Society*, pages 21–22. 2006.
- [35] Daniel E. Koditschek. Adaptive techniques for mechanical systems. In *Fifth Yale Workshop on Applications of Adaptive Systems Theory*, pages 259–265, May 1987.
- [36] Daniel E. Koditschek and Elon Rimon. Robot navigation functions on manifolds with boundary. *Advances in Applied Mathematics*, 11:412–442, 1990.
- [37] Miroslav Krstic, Petar V. Kokotovic, and Ioannis Kanellakopoulos. *Nonlinear and Adaptive Control Design*. John Wiley & Sons, Inc., New York, NY, USA, 1st edition, 1995.
- [38] Amit Kumar, Herbert G. Tanner, Alexei V. Klimenko, Konstantin Borozdin, and William C. Priedhorsky. Automated sequential search for weak radiation sources. In *Proceedings of the IEEE Mediterranean Conference on Control and Automation*, pages 1–6, June 2006.
- [39] P. A. W Lewis and G. S. Shedler. Simulation of nonhomogeneous Poisson processes by thinning. *Naval Research Logistics Naval Research Logistics Quarterly*, 26(3):403–413, 1979.
- [40] Shu-Jun Liu and M. Krstic. Stochastic averaging in continuous time and its applications to extremum seeking. *IEEE Transactions on Automatic Control*, 55(10):2235–2250, Oct 2010.
- [41] Shu-Jun Liu and Miroslav Krstic. Stochastic source seeking for nonholonomic unicycle. *Automatica*, 46(9):1443 – 1453, 2010.
- [42] S.G. Loizou, H.G. Tanner, V. Kumar, and K.J. Kyriakopoulos. Closed loop navigation for mobile agents in dynamic environments. In *Proceedings of the IEEE/RSJ International Conference on Intelligent Robots and Systems*, volume 4, pages 3769–3774, Oct 2003.
- [43] C.Y.T. Ma, D.K.Y. Yau, N.K. Yip, N.S.V. Rao, and J. Chen. Performance analysis of stochastic network coverage with limited mobility. In *IEEE International Conference on Mobile AdHoc and Sensor Systems*, pages 496–505, 2009.

- [44] J.D. Marble and K.E. Bekris. Asymptotically near-optimal planning with probabilistic roadmap spanners. *IEEE Transactions on Robotics*, 29(2):432–444, April 2013.
- [45] Daniel Mellinger, Nathan Michael, and Vijay Kumar. Trajectory generation and control for precise aggressive maneuvers with quadrotors. *The International Journal of Robotics Research*, 31:664–674, 2012.
- [46] R.J. Nemzek, J.S. Dreicer, D.C. Torney, and T.T. Warnock. Distributed sensor networks for detection of mobile radioactive sources. *IEEE Transactions on Nuclear Science*, 51:1693–1700, 2004.
- [47] Robert J. Nemzek, Jared S. Dreicer, David C. Torney, and Tony T. Warnock. Distributed sensor networks for detection of mobile radioactive sources. *IEEE Transactions on Nuclear Science*, 51(4):1693–1700, 2004.
- [48] C. M. Newman and B. W. Stuck. Chernoff bounds for discriminating between two Markov processes. *Stochastics*, 2:139–153, 1979.
- [49] Chetan D. Pahlajani, Ioannis Poulakakis, and Herbert G. Tanner. Networked decision making for poisson processes with applications to nuclear detection. *IEEE Transactions on Automatic Control*, 59(1):193–198, Jan 2014.
- [50] Chetan D. Pahlajani, Jianxin Sun, Ioannis Poulakakis, and Herbert G. Tanner. Error probability bounds for nuclear detection: Improving accuracy through controlled mobility. *Automatica*, 50(10):2470 – 2481, 2014.
- [51] Raghu Pasupathy. Generating nonhomogeneous Poisson processes. In *Wiley Encyclopedia of Operations Research and Management Science*. Wiley, 2009.
- [52] A. Perez, R. Platt, G.D. Konidaris, L.P. Kaelbling, and T. Lozano-Pérez. Lqr-rrt\*: Optimal sampling-based motion planning with automatically derived extension heuristics. In *IEEE International Conference on Robotics and Automation*, pages 2537–2542, May 2012.
- [53] Anna Petrovskaya and Sebastian Thrun. Model based vehicle detection and tracking for autonomous urban driving. *Autonomous Robots*, 26(2-3):123–139, 2009.
- [54] Anil V. Rao, David A. Benson, Christopher Darby, Michael A. Patterson, Camila Francolin, Ilyssa Sanders, and Geoffrey T. Huntington. Algorithm 902: GPOPS, a MATLAB software for solving multiple-phase optimal control problems using the gauss pseudospectral method. *ACM Transactions on Mathematical Software*, 37(2):22:1–22:39, April 2010.
- [55] Branko Ristic and Ajith Gunatilaka. Information driven localisation of a radiological point source. *Information fusion*, 9(2):317—326, 2008.

- [56] Branko Ristic, Mark Morelande, and Ajith Gunatilaka. Information driven search for point sources of gamma radiation. *Signal Processing*, 90(4):1225–1239, 2010.
- [57] S.K. Shah, H.G. Tanner, and C.D. Pahlajani. Optimal navigation for vehicles with stochastic dynamics. *IEEE Transactions on Control Systems Technology*, PP(99):1–1, 2015.
- [58] Donald L. Snyder. *Random Point Processes*. Wiley-Interscience, 1975.
- [59] Xuan Song, Xiaowei Shao, Quanshi Zhang, R. Shibasaki, Huijing Zhao, and Hongbin Zha. Laser-based intelligent surveillance and abnormality detection in extremely crowded scenarios. In *IEEE International Conference on Robotics and Automation*, pages 2170–2176, St. Paul, USA, 2012. ID: 1.
- [60] Luciano Spinello, Rudolph Triebel, and Roland Siegwart. Multiclass multimodal detection and tracking in urban environments. *The International Journal of Robotics Research*, 29(12):1498–1515, October 01 2010.
- [61] Devabhaktuni Srikrishna, A. Narasimha Chari, and Thomas Tisch. Deterance of nuclear terrorism with mobile radiation detectors. *The Nonproliferation Review*, 12(3):573–614, 2005.
- [62] Sean Summers, Maryam Kamgarpour, John Lygeros, and Claire Tomlin. A stochastic reach-avoid problem with random obstacles. In *Proceedings of the 14th International Conference on Hybrid Systems: Computation and Control, HSCC '11*, pages 251–260, New York, NY, USA, 2011. ACM.
- [63] Sean Summers, Maryam Kamgarpour, Claire Tomlin, and John Lygeros. Stochastic system controller synthesis for reachability specifications encoded by random sets. *Automatica*, 49(9):2906 – 2910, 2013.
- [64] Jianxin Sun and Herbert G. Tanner. Constrained decision-making for low-count radiation detection by mobile sensors. *Autonomous Robots*, 39(4):519–536, 2015.
- [65] Jianxin Sun, H.G. Tanner, and I. Poulakakis. Active sensor networks for nuclear detection. In *2015 IEEE International Conference on Robotics and Automation*, pages 3549–3554, May 2015.
- [66] Ashok Sundaresan, Pramod K. Varshney, and Nageswara S. V. Rao. Distributed detection of a nuclear radioactive source using fusion of correlated decisions. In *Proceedings of the International Conference on Information Fusion*, pages 1–7. IEEE, 2007.
- [67] H.G. Tanner and A. Boddu. Multiagent navigation functions revisited. *IEEE Transactions on Robotics*, 28(6):1346–1359, Dec 2012.

- [68] NicolasA Tsokas and KostasJ Kyriakopoulos. Multi-robot multiple hypothesis tracking for pedestrian tracking. *Autonomous Robots*, 32(1):63–79, 2012.
- [69] J.N. Twigg, J.R. Fink, P.L. Yu, and B.M. Sadler. Rss gradient-assisted frontier exploration and radio source localization. In *IEEE International Conference on Robotics and Automation*, pages 889–895, St. Paul, MN, May 2012.
- [70] Pramod K. Varshney. *Distributed Detection and Data Fusion*. Springer-Verlag, 1997.
- [71] Dizan Vasquez, Thierry Fraichard, and Christian Laugier. Growing hidden markov models: An incremental tool for learning and predicting human and vehicle motion. *The International Journal of Robotics Research*, 28(11-12):1486–1506, November 01 2009.
- [72] S. Venkateswaran, J.T. Isaacs, K. Fregene, R. Ratmansky, B.M. Sadler, J.P. Hespanha, and U. Madhow. Rf source-seeking by a micro aerial vehicle using rotation-based angle of arrival estimates. In *American Control Conference*, pages 2581–2587, Washington, DC, June 2013.
- [73] M. Vidyasagar. Statistical learning theory and randomized algorithms for control. *IEEE Control Systems Magazine*, 18(6):69–85, 1998.
- [74] M. Vidyasagar. Statistical learning theory and randomized algorithms for control. *IEEE Control Systems Magazine*, 18:69–85, 1998.
- [75] H. Wei, W. Lu, P. Zhu, G. Huang, J. Leonard, and S. Ferrari. Visibility-based motion planning for active target tracking and localization. In *Proceedings of the IEEE/RSJ International Conference on Intelligent Robots and Systems*, pages 76–82, Chicago, Illinois, Sept. 2014.
- [76] L.M. Wein and M.P. Atkinson. The last line of defense: designing radiation detection-interdiction systems to protect cities form a nuclear terrorist attack. *IEEE Transactions on Nuclear Science*, 54(3):654–669, 2007.
- [77] Chunlei Zhang, D. Arnold, N. Ghods, A. Siranosian, and M. Krstic. Source seeking with nonholonomic unicycle without position measurement—part i: Tuning of forward velocity. In *IEEE Conference on Decision and Control*, pages 3040–3045, San Diego, CA, USA, Dec 2006.
- [78] Ke Zhou and S. I. Roumeliotis. Multirobot active target tracking with combinations of relative observations. *IEEE Transactions on Robotics*, 27(4):678–695, 2011. ID: 1.
- [79] Ke X. Zhou and S. I. Roumeliotis. Multi-robot active target tracking with distance and bearing observations. In *IEEE/RSJ International Conference on Intelligent Robots and Systems*, pages 2209–2216, St. Louis, USA, 2009. ID: 1.

- [80] J. Ziegler and C. Stiller. Spatiotemporal state lattices for fast trajectory planning in dynamic on-road driving scenarios. In *IEEE/RSJ International Conference on Intelligent Robots and Systems*, pages 1879–1884, Oct 2009.

## Appendix A

### THEOREM 4.3.1: INTERMEDIATE RESULTS

To simplify notation, we drop the subscript  $x_i$  from the expressions of the gradient and hessian of the navigation, with the understanding that all these differentiations are with respect to  $x_i$ . Similarly, instead of distinguishing the obstacle and navigation function of agent  $i$  by writing  $\beta_i$  and  $\varphi_i$ , we simply refer to it generically as  $\beta$  and  $\varphi$ . We will use the index  $i$  to range over obstacles in the environment.

With a slight abuse of notation, we will now think of the free workspace  $\mathcal{P}$  as a subset of  $\mathbb{R}^n$  (instead of just  $\mathbb{R}^3$ ); the results established in this section hold irrespective of the particular value of  $n \in \mathbb{N}_+$ . Let  $\partial\mathcal{S}_T = \{x \in \mathbb{R}^n : \|x - x_t\| = r_t\}$ , for a small  $\epsilon > 0$   $\mathcal{B}_i(\epsilon) \triangleq \{x \in \mathbb{R}^n : 0 < \beta_i(x) < \epsilon\}$ , and (re)define the decomposition of  $\overline{\mathcal{P}}$  into sets  $\partial\mathcal{F}$ ,  $\mathcal{F}_0(\epsilon)$ ,  $\mathcal{F}_1(\epsilon)$ ,  $\mathcal{F}_2(\epsilon)$  and  $\mathcal{W}(\epsilon)$  as follows.

1. the free space boundary

$$\partial\mathcal{F} = \partial\mathcal{P} = \beta^{-1}(0) ;$$

2. the set “near the obstacles”

$$\mathcal{F}_0(\epsilon) \triangleq \bigcup_{i=1}^M \mathcal{B}_i(\epsilon) \setminus \partial\mathcal{S}_T ;$$

3. the set “near the workspace boundary”

$$\mathcal{F}_1(\epsilon) \triangleq \mathcal{B}_0(\epsilon) \setminus (\partial\mathcal{S}_T \cup \mathcal{F}_0(\epsilon)) ;$$

4. the set “away from the obstacles”

$$\mathcal{F}_2(\epsilon) \triangleq \mathcal{P} \setminus (\partial\mathcal{S}_T \cup \partial\mathcal{F} \cup \mathcal{F}_0(\epsilon) \cup \mathcal{F}_1(\epsilon)) .$$

5. the set “away from the obstacles and target”

$$\mathcal{W}(\epsilon) = \mathcal{F}_2(\epsilon) \setminus \mathcal{B}_{x_t}(\delta_t) .$$

Recall that a workspace is called *valid*, if the obstacles do not overlap with each other and the destination (set).

**Proposition A.0.1** *If the workspace is valid, any  $x_d \in \partial\mathcal{S}_T$  is a degenerate local minimum of  $\varphi$ . A vector  $v$  satisfying  $v^\top \nabla^2 \varphi(x_d) v = 0$  has to be tangent to  $\partial\mathcal{S}_T$ .*

**Proof** Evaluate

$$\nabla \varphi(x_d) = \frac{(J^k + \beta)^{1/k} \nabla J - J \nabla (J^k + \beta)^{1/k}}{(J^k + \beta)^{2/k}} \Big|_{x_d}$$

and note that since  $J|_{x_d} = 0$  and  $\nabla J|_{x_d} = 0$ , it is  $\nabla \varphi(x_d) = 0$ . Now

$$\begin{aligned} \nabla^2 \varphi(x_d) &= \frac{(J^k + \beta)^{1/k} \nabla^2 J - J \nabla^2 (J^k + \beta)^{1/k}}{(J^k + \beta)^{2/k}} \Big|_{x_d} \\ &= \beta^{-1/k} \nabla^2 J \Big|_{x_d} = 8 \beta^{-1/k} (x_d - x_t)(x_d - x_t)^\top . \end{aligned}$$

Consider arbitrary vector  $v \in \mathbb{R}^n$  and evaluate the quadratic form

$$v^\top \nabla^2 \varphi(x_d) v = 8 \beta^{-1/k} v^\top (x_d - x_t)(x_d - x_t)^\top v = 8 \beta^{-1/k} \|v^\top (x_d - x_t)\|^2 .$$

This means that  $v^\top \nabla^2 \varphi(x_d) v \geq 0$  with equality if and only if  $v$  is normal to  $(x_d - x_t)$ , that is, when  $v$  is tangent to  $\partial\mathcal{S}_T$ . ■

**Proposition A.0.2** *If the workspace is valid, all the critical points of  $\varphi$  are in the interior of the free space.*

**Proof** Let  $x_0$  be a point in  $\partial\mathcal{F}$ . Then by definition,  $\beta_i(x_0) = 0$  for some  $i \in \{0, \dots, M\}$ . From the workspace being valid, it follows that  $\beta_j > 0$  for all  $j \in \{0, \dots, M\}$ ,  $j \neq i$ . Then,

$$\begin{aligned} \nabla\varphi(x_d) &= \frac{(J^k + \beta)^{1/k} \nabla J - J \nabla(J^k + \beta)^{1/k}}{(J^k + \beta)^{2/k}} \Big|_{x_0} \\ &= \frac{\nabla J - \frac{1}{k} J^{1-k} (kJ^{k-1} \nabla J + \nabla\beta)}{J} \Big|_{x_0} \\ &= -\frac{1}{k} J^{-k} \prod_{j=0, j \neq i}^M \beta_j \nabla\beta_i \neq 0 , \end{aligned}$$

which completes the proof.  $\blacksquare$

**Proposition A.0.3** *For every  $\epsilon > 0$  there exists a positive integer  $N(\epsilon)$  such that if  $k \geq N(\epsilon)$  then there are no critical points of  $\frac{J^k}{\beta}$  in  $\mathcal{W}(\epsilon)$ .*

**Proof** A sufficient condition for  $\frac{J^k}{\beta}$  not having critical points in  $\mathcal{W}$  is [36, Proposition 3.4]]

$$k > \frac{J \|\nabla\beta\|}{\beta \|\nabla J\|} .$$

For this, it is sufficient to have

$$k \geq \sup_{\mathcal{W}} \frac{J}{\|\nabla J\|} \sup_{\mathcal{W}} \frac{\|\nabla\beta\|}{\beta} > \frac{J \|\nabla\beta\|}{\beta \|\nabla J\|} .$$

The existence of a finite bound of  $\sup_{\mathcal{W}} \frac{J}{\|\nabla J\|} \sup_{\mathcal{W}} \frac{\|\nabla\beta\|}{\beta}$  can be established analytically as follows.

$$\sup_{\mathcal{W}} \frac{J}{\|\nabla J\|} = \sup_{\mathcal{W}} \frac{(\|x - x_t\|^2 - r_t^2)^2}{|4\|x - x_t\|^3 - 4r_t^2\|x - x_t\||} = \sup_{\mathcal{W}} \frac{\sqrt{J}}{4\|x - x_t\|} .$$

Since  $\|x - x_t\|$  is bounded from below and above in  $\mathcal{W}$ , and  $\inf_{\mathcal{W}} \|x - x_t\| = \delta_t$ , it is ensured that  $\sup_{\mathcal{W}} \frac{J}{\|\nabla J\|}$  is finite. For the other bound, we have

$$\begin{aligned} \frac{\|\nabla\beta\|}{\beta} &< \sup_{\mathcal{W}} \frac{\|\nabla\beta\|}{\beta} \\ &\leq \sup_{\mathcal{W}} \sum_{i=0}^M \frac{\|\nabla\beta_i\|}{\beta_i} \\ &\leq \frac{2}{\epsilon} \left[ \rho_0 + \sum_{i=1}^M \sup_{\mathcal{W}} \|x - o_i\| \right] . \end{aligned} \tag{A.1}$$

The strict inequality is due to the fact that  $\|x\| < \rho_0$  for any point in  $\mathcal{W}$ . Equation (A.1) implies that  $\sup_{\mathcal{W}} \frac{\|\nabla\beta\|}{\beta}$  exists and is bounded. Thus, a choice of a sufficiently large  $k \geq N(\epsilon)$  would be

$$N(\epsilon) := \frac{1}{\epsilon} \sup_{\mathcal{W}(0)} \left\{ \frac{\sqrt{J}}{2\|x - x_t\|} \right\} \left( \rho_0 + \sum_{i=1}^M \sup_{\mathcal{W}(0)} \|x - o_i\| \right) . \quad (\text{A.2})$$

The proof is thus completed. ■

**Proposition A.0.4** *For any valid workspace, there exists an  $\epsilon_0 > 0$  such that  $\frac{J^k}{\beta}$  has no local minima in  $\mathcal{F}_0(\epsilon)$ , as long as  $\epsilon < \epsilon_0$ .*

**Proof** The analysis focuses on  $\mathcal{F}_0(\epsilon)$ , and that implies that for any critical point  $x_c \in \mathcal{F}_0(\epsilon)$ , for some  $i$  we will have  $x_c \in \mathcal{B}_i(\epsilon)$ ; therefore,  $0 < \beta_i(x_c) < \epsilon$ . The validity of the workspace guarantees that  $\|o_i - x_t\| > r_t + \rho_i + \epsilon_t$ . Because of this, that particular ball  $\mathcal{B}_i(\epsilon)$  is bounded away from  $\partial\mathcal{S}_T$ : for any  $x \in \mathcal{B}_i(\epsilon)$ , it is  $\|x - x_t\| > r_t$  as long as  $0 < \|x - o_i\| - \rho_i < \sqrt{\epsilon + \rho_i^2} - \rho_i < \epsilon_t < \|o_i - x_t\| - r_t - \rho_i$ . Since  $x_c$  is a critical point,  $k\beta \nabla J = J \nabla\beta$  at  $x_c$ . Note that everywhere in  $\mathcal{F}_0(\epsilon)$ ,  $J \neq 0$  and  $\beta \neq 0$ . Therefore,  $\nabla J$  is aligned with  $\nabla\beta$ . Using the concept of the omitted product [ [36]]

$$\bar{\beta}_i \triangleq \prod_{j=0, j \neq i}^M \beta_j ,$$

vector  $\nabla\beta$  expands to

$$\nabla\beta = \sum_{j=1}^M 2(x_c - o_j)\bar{\beta}_j - 2\bar{\beta}_0 x_c = 2(x_c - o_i)\bar{\beta}_i + 2\beta_i \sum_{j=1, j \neq i}^M (x_c - o_j) \frac{\bar{\beta}_j}{\beta_i} - 2\bar{\beta}_0 x_c$$

and by defining

$$\alpha_i \triangleq 2 \sum_{j=1, j \neq i}^M (x_c - o_j) \frac{\bar{\beta}_j}{\beta_i} - 2\frac{\bar{\beta}_0}{\beta_i} x_c ,$$

which is a vector independent from  $\epsilon$ , and bounded in  $\mathcal{F}_0(\epsilon)$ , one has

$$\nabla\beta = 2(x_c - o_i)\bar{\beta}_i + \beta_i \alpha_i .$$

From  $k\beta \nabla J = J \nabla \beta$  at  $x_c$  it now follows that

$$\nabla J = \frac{J}{k\beta} \nabla \beta \iff 4(\|x_c - x_t\|^2 - r_t^2)(x_c - x_t) = \frac{J}{k\beta} [2(x_c - o_i)\bar{\beta}_i + \beta_i \alpha_i]$$

which leads to

$$x_c - x_t = \frac{\|x_c - x_t\|^2 - r_t^2}{4} \left( 2\frac{x_c - o_i}{k\beta_i} + \frac{\alpha_i}{k\bar{\beta}_i} \right). \quad (\text{A.3})$$

If one now sets

$$C_k \triangleq \sup_{\mathcal{W}(0)} \left\{ \frac{\sqrt{J}}{2\|x_c - x_t\|} \right\} \left( \rho_0 + \sum_{i=1}^M \sup_{\mathcal{W}(0)} \|x_c - o_i\| \right),$$

then according to (A.2) in the proof of Proposition A.0.3, a suitable choice of  $k$  would be

$$k := \frac{C_k}{\epsilon},$$

in which case (A.3) becomes

$$x_c - x_t = \frac{\epsilon(\|x_c - x_t\|^2 - r_t^2)}{4C_k} \left( 2\frac{x_c - o_i}{\beta_i} + \frac{\alpha_i}{\bar{\beta}_i} \right). \quad (\text{A.4})$$

Taking the inner product of both sides of  $k\beta \nabla J = J \nabla \beta$  with  $\nabla J$  yields

$$k\beta \nabla J^\top \nabla J = J \nabla \beta^\top \nabla J \implies k\beta = \frac{\bar{\beta}_i \nabla \beta_i^\top \nabla J + \beta_i \nabla \bar{\beta}_i^\top \nabla J}{16\|x_c - x_t\|^2}. \quad (\text{A.5})$$

From this point, one can then prove that the critical point of  $\frac{J^k}{\beta}$  is not a local minimum by showing that  $\nabla^2 \frac{J^k}{\beta}$  has at least one negative eigenvalue at that point. (The procedure follows the exact same steps as [36, Proposition 3.6].) Essentially, it amounts to using any vector  $\hat{v}$  orthogonal to  $\frac{\nabla \beta_i}{\|\nabla \beta_i\|}$  as a test vector, and showing that at  $x_c$  and for small enough  $\epsilon$ ,  $\hat{v}^\top \nabla^2 \frac{J^k}{\beta} \hat{v} < 0$ . The process in detail is as follows:

$$\begin{aligned} \frac{\beta^2}{J^{k-1}} \hat{v}^\top \nabla^2 \frac{J^k}{\beta} \Big|_{x_c} \hat{v} &= k\beta \hat{v}^\top \nabla^2 J \hat{v} - 2J\bar{\beta}_i + \hat{v}^\top J\beta_i \left[ \frac{1 - \frac{1}{k}}{\bar{\beta}_i} \nabla \bar{\beta}_i \nabla \bar{\beta}_i^\top - \nabla^2 \bar{\beta}_i \right] \hat{v} \\ &\stackrel{(\text{A.5})}{=} \frac{\bar{\beta}_i \nabla \beta_i^\top \nabla J + \beta_i \nabla \bar{\beta}_i^\top \nabla J}{16\|x_c - x_t\|^2} \hat{v}^\top \nabla^2 J \hat{v} - 2J\bar{\beta}_i + \hat{v}^\top J\beta_i \left[ \frac{1 - \frac{1}{k}}{\bar{\beta}_i} \nabla \bar{\beta}_i \nabla \bar{\beta}_i^\top - \nabla^2 \bar{\beta}_i \right] \hat{v} \\ &= \bar{\beta}_i \left( \frac{\hat{v}^\top \nabla^2 J \hat{v}}{16\|x_c - x_t\|^2} \nabla \beta_i^\top \nabla J - 2J \right) \\ &\quad + \beta_i \left( \frac{\hat{v}^\top \nabla^2 J \hat{v}}{16\|x_c - x_t\|^2} \nabla \bar{\beta}_i^\top \nabla J + J \hat{v}^\top \left[ \frac{1 - \frac{1}{k}}{\bar{\beta}_i} \nabla \bar{\beta}_i \nabla \bar{\beta}_i^\top - \nabla^2 \bar{\beta}_i \right] \hat{v} \right). \quad (\text{A.6}) \end{aligned}$$

To determine the sign of the far right side of (A.6), perform the expansion of  $\hat{v}^\top \nabla^2 J \hat{v}$  into

$$\begin{aligned} & \hat{v}^\top \left[ 4(\|x_c - x_t\|^2 - r_t^2)\mathbf{I} + 8(x_c - x_t)(x_c - x_t)^\top \right] \hat{v} \\ &= 4(\|x_c - x_t\|^2 - r_t^2) + 8\hat{v}^\top (x_c - x_t)(x_c - x_t)^\top \hat{v} \\ &= 4(\|x_c - x_t\|^2 - r_t^2) + 8(\hat{v}^\top (x_c - x_t))^2, \quad (\text{A.7}) \end{aligned}$$

where  $\mathbf{I}$  denotes the identity matrix, and plug (A.4) into (A.7), to express  $\hat{v}^\top \nabla^2 J \hat{v}$  in the form

$$\begin{aligned} & 4(\|x_c - x_t\|^2 - r_t^2) + 8 \left| \hat{v}^\top \frac{\epsilon(\|x_c - x_t\|^2 - r_t^2)}{4C_k} \left( 2\frac{x_c - o_i}{\beta_i} + \frac{\alpha_i}{\beta_i} \right) \right|^2 \\ &= 4\sqrt{J} + \frac{\epsilon^2 J |\hat{v}^\top \alpha_i|^2}{2C_k^2 \beta_i^2}. \quad (\text{A.8}) \end{aligned}$$

where  $\hat{v}^\top (x_c - o_i) = 0$  and  $\sqrt{J}$  is substituted for  $\|x_c - x_t\|^2 - r_t^2$  (for brevity), since in  $\mathcal{F}_0(\epsilon)$  it holds  $\|x_c - x_t\| > r_t$ .

Given now that the second term in (A.6) can be made arbitrarily small by choosing  $\epsilon > \beta_i$ , one can establish the negative definiteness of (A.6) by ensuring that the first term is strictly below zero. The second factor in the first term in (A.6) can be expanded

$$\begin{aligned} & \frac{\hat{v}^\top \nabla^2 J \hat{v}}{16\|x_c - x_t\|^2} \nabla \beta_i^\top \nabla J - 2J \\ & \stackrel{(\text{A.8})}{=} \frac{2\sqrt{J} + \frac{\epsilon^2 J}{4C_k^2 \beta_i^2} |\hat{v}^\top \alpha_i|^2}{8\|x_c - x_t\|^2} 2(x_c - o_i) 4(x_c - x_t) \sqrt{J} - 2J \\ &= 2J \left[ \frac{(x_c - o_i)^\top (x_c - x_t)}{\|x_c - x_t\|^2} - 1 \right] + \frac{\epsilon^2 J^{1.5} |\hat{v}^\top \alpha_i|^2}{4C_k^2 \beta_i^2 \|x_c - x_t\|^2} (x_c - o_i)^\top (x_c - x_t) \\ &= \frac{2J(x_c - o_i)^\top (x_c - x_t)}{\|x_c - x_t\|^2} + \frac{\epsilon^2 J^{1.5} |\hat{v}^\top \alpha_i|^2 (x_c - o_i)^\top (x_c - x_t)}{4C_k^2 \beta_i^2 \|x_c - x_t\|^2} \end{aligned}$$

and by applying known relations [36, Lemma 3.5] one arrives at

$$\begin{aligned} & \frac{\hat{v}^\top \nabla^2 J \hat{v}}{16\|x_c - x_t\|^2} \nabla \beta_i^\top \nabla J - 2J \\ & \leq \frac{2J\|x_t - o_i\| (\sqrt{\epsilon + \rho_i^2} - \|x_t - o_i\|)}{\|x_c - x_t\|^2} + \epsilon^2 \sup_{\mathcal{F}_0(\epsilon)} \frac{J^{1.5} |\hat{v}^\top \alpha_i|^2 (x_c - o_i)^\top (x_c - x_t)}{4C_k^2 \beta_i^2 \|x_c - x_t\|^2}. \quad (\text{A.9}) \end{aligned}$$

At this point, (A.9) is used in (A.6) to upper bound the left hand side of (A.6)

$$\begin{aligned} \frac{\beta^2}{J^{k-1}} \hat{v}^\top \nabla^2 \frac{J^k}{\beta} \Big|_{x_c} \hat{v} &\leq \frac{2J\bar{\beta}_i \|x_t - o_i\| (\sqrt{\epsilon + \rho_i^2} - \|x_t - o_i\|)}{\|x_c - x_t\|^2} \\ &+ \epsilon \left( \bar{\beta}_i \in \sup_{\mathcal{F}_0(\epsilon)} \frac{J^{1.5} |\hat{v}^\top \alpha_i|^2 (x_c - o_i)^\top (x_c - x_t)}{4C_k^2 \bar{\beta}_i^2 \|x_c - x_t\|^2} + \frac{\hat{v}^\top \nabla^2 J \hat{v}}{16\|x_c - x_t\|^2} \nabla \bar{\beta}_i^\top \nabla J \right. \\ &\quad \left. + J \hat{v}^\top \left[ \frac{1-\frac{1}{k}}{\bar{\beta}_i} \nabla \bar{\beta}_i \nabla \bar{\beta}_i^\top - \nabla^2 \bar{\beta}_i \right] \hat{v} \right) . \end{aligned}$$

Now choosing  $\epsilon$  appropriately small, the second term can be made sufficiently small so that the sign of the first term dominates. The sign of the latter is determined by the expression  $\sqrt{\epsilon + \rho_i^2} - \|x_t - o_i\|$ , which for small  $\epsilon$  approaches  $\rho_i - \|x_t - o_i\|$ , which is guaranteed negative by the validity of the workspace. (The target  $x_t$  is  $(r_t + \rho_i)$  away from the center of obstacle  $i$ .) ■

**Proposition A.0.5** *If  $k \geq \frac{C_k}{\epsilon}$ , then there exists an  $\epsilon_1 > 0$  such that  $\hat{\varphi} = \frac{J^k}{\beta}$  has no critical points on  $\mathcal{F}_1(\epsilon)$ , as long as  $\epsilon < \epsilon_1$ .*

**Proof** The set  $\mathcal{F}_1(\epsilon)$  expresses the neighborhood of the workspace (outer) boundary. Select  $\epsilon$  small enough so that the  $\mathcal{B}_0(\epsilon)$  neighborhood of the outer boundary is disjoint from the  $r_t$ -neighborhood of the target:  $\beta_0 < \epsilon < \rho_0^2 - (\|x_t\| + r_t)^2$ . Then any critical point  $x_c \in \mathcal{F}_1(\epsilon)$  will satisfy  $\beta_0(x_c) = \rho_0^2 - \|x_c\|^2 < \epsilon$ , implying  $\|x_c\| > \|x_t\| + r_t$ . Then in  $\mathcal{B}_0(\epsilon)$

$$\begin{aligned} \nabla J^\top \nabla \beta_0 &= 4(\|x_c - x_t\|^2 - r_t^2)(x_c - x_t)^\top (-2x_c) \\ &= 8(\|x_c - x_t\|^2 - r_t^2)(x_t^\top x_c - \|x_c\|^2) \\ &\leq 8(\|x_c - x_t\|^2 - r_t^2)(\|x_c\|\|x_t\| - \|x_c\|^2) \\ &= 8(\|x_c - x_t\|^2 - r_t^2) \|x_c\| (\|x_t\| - \|x_c\|) \\ &< 0 . \end{aligned}$$

By choosing  $\epsilon$  small enough, we can ensure that  $\nabla\hat{\varphi}$  does not vanish in  $\mathcal{F}_1(\epsilon)$ . Here is why:

$$\begin{aligned}
\nabla\hat{\varphi}^\top \nabla J &= \left[ \frac{kJ^{k-1}}{\beta} \nabla J - \frac{J^k}{\beta^2} \nabla\beta \right]^\top \nabla J \\
&= \frac{J^k (16k\beta \|x_c - x_t\|^2 - \nabla\beta^\top \nabla J)}{\beta^2} \\
&= \frac{J^k [16k\beta \|x_c - x_t\|^2 - (\beta_0 \nabla\bar{\beta}_0^\top \nabla J + \bar{\beta}_0 \nabla\beta_0^\top \nabla J)]}{\beta^2} \\
&\stackrel{(\nabla J^\top \nabla\beta_0 < 0)}{>} \frac{J^k \beta_0 (16k\bar{\beta}_0 \|x_c - x_t\|^2 - \nabla\bar{\beta}_0^\top \nabla J)}{\beta^2}
\end{aligned}$$

and thus any  $\epsilon$  small enough to make  $k > \frac{\nabla\bar{\beta}_0^\top \nabla J}{16\bar{\beta}_0 \|x_c - x_t\|^2}$ , will also make  $\nabla\hat{\varphi}^\top \nabla J$  positive. In fact, the choice utilized earlier, i.e.,  $k = \frac{C_k}{\epsilon}$  suffices. To see this,

$$\begin{aligned}
\frac{\nabla\bar{\beta}_0^\top \nabla J}{16\bar{\beta}_0 \|x_c - x_t\|^2} &\leq \frac{\|\nabla\bar{\beta}_0\| \|\nabla J\|}{16\bar{\beta}_0 \|x_c - x_t\|^2} = \frac{\frac{\sqrt{J}}{\beta} \sum_{i=1}^M \bar{\beta}_i \|\nabla\beta_i\|}{4\|x_c - x_t\|} \\
&< \frac{1}{\epsilon} \sup_{\mathcal{W}(0)} \left\{ \frac{\sqrt{J}}{2\|x_c - x_t\|} \right\} \sum_{i=1}^M \sup_{\mathcal{W}(0)} \|x_c - o_i\| ,
\end{aligned}$$

and compare to

$$\begin{aligned}
k := \frac{C_k}{\epsilon} &= \frac{1}{\epsilon} \sup_{\mathcal{W}(0)} \left\{ \frac{\sqrt{J}}{2\|x_c - x_t\|} \right\} \left( \rho_0 + \sum_{i=1}^M \sup_{\mathcal{W}(0)} \|x_c - o_i\| \right) \\
&> \frac{1}{\epsilon} \sup_{\mathcal{W}(0)} \left\{ \frac{\sqrt{J}}{2\|x_c - x_t\|} \right\} \sum_{i=1}^M \sup_{\mathcal{W}(0)} \|x_c - o_i\| .
\end{aligned}$$

It thus suffices to pick  $\epsilon < \epsilon_1 = (\rho_0)^2 - (\|x_t\| + r_t)^2$  to ensure that no critical points are in  $\mathcal{F}_1(\epsilon)$ . ■

**Proposition A.0.6** *Critical points in the interior of  $\mathcal{F}_0(\epsilon)$  are non-degenerate.*

**Proof** One way to establish such a claim [ [36, Proposition 3.9]] is to partition the tangent space of  $\hat{\varphi}$  into a subspace that yields positive values for the quadratic form constructed with  $\nabla^2\hat{\varphi}$ , and a subset that yields negative values. The negative case is established by Proposition A.0.4. The positive case, again along the lines of [ [36, Proposition 3.9]], is established here by taking a test direction  $\widehat{\nabla}\beta_i = \frac{\nabla\beta_i}{\|\nabla\beta_i\|}$ , and picking

$\epsilon$  small enough to obtain  $\widehat{\nabla\beta}_i^\top \nabla^2 \hat{\varphi} \widehat{\nabla\beta}_i > 0$ . Note that for a given  $i$ ,  $\widehat{\nabla\beta}_i$  defines one subspace, and all the vectors  $\hat{v}$  form its orthogonal complement. To verify the sign of  $\widehat{\nabla\beta}_i^\top \nabla^2 \hat{\varphi} \widehat{\nabla\beta}_i$ , expand the expression

$$\begin{aligned} \frac{\beta^2}{J^{k-1}} \widehat{\nabla\beta}_i^\top \nabla^2 \hat{\varphi} \widehat{\nabla\beta}_i &= \widehat{\nabla\beta}_i^\top k\beta \nabla^2 J \widehat{\nabla\beta}_i \\ &+ \frac{J(1 - \frac{1}{k})}{\beta} (\nabla\beta^\top \widehat{\nabla\beta}_i)^2 - J \widehat{\nabla\beta}_i^\top \nabla^2 \beta \widehat{\nabla\beta}_i . \end{aligned} \quad (\text{A.10})$$

We know [36, Proposition 3.9] that for small enough  $\epsilon$ ,

$$\frac{J\|\nabla\beta\|^2}{2k\beta} + \frac{J(1 - \frac{1}{k})}{\beta} (\nabla\beta^\top \widehat{\nabla\beta}_i)^2 - J \widehat{\nabla\beta}_i^\top \nabla^2 \beta \widehat{\nabla\beta}_i > 0 .$$

Although different  $J$  function is used here, the same derivation in [ [36, Proposition 3.9]] holds here. So to set the sign of (A.10), it suffices to make

$$\widehat{\nabla\beta}_i^\top k\beta \nabla^2 J \widehat{\nabla\beta}_i \geq \frac{J\|\nabla\beta\|^2}{2k\beta} . \quad (\text{A.11})$$

Recalling (A.7), and that  $\|x_c - x_t\|^2 - r_t^2 = \sqrt{J}$  since  $x_c$  is a critical point, the left hand side of (A.11) is

$$\widehat{\nabla\beta}_i^\top k\beta \nabla^2 J \widehat{\nabla\beta}_i = 4k\beta\sqrt{J} + 8k\beta|\widehat{\nabla\beta}_i^\top(x_c - x_t)|^2 \quad (\text{A.12})$$

and because  $x_c$  is a critical point, taking squared norms of both sides of  $k\beta \nabla J = J \nabla\beta$  yields

$$(4k\beta\sqrt{J}\|x_c - x_t\|)^2 = J^2\|\nabla\beta\|^2 ,$$

from which one extracts that

$$4k\beta = \frac{J\|\nabla\beta\|^2}{4k\beta\|x_c - x_t\|^2} . \quad (\text{A.13})$$

Plugging now (A.13) back into (A.12) yields

$$\widehat{\nabla\beta}_i^\top k\beta \nabla^2 J \widehat{\nabla\beta}_i = \frac{J^{3/2}\|\nabla\beta\|^2}{4k\beta\|x_c - x_t\|^2} + \frac{J\|\nabla\beta\|^2 |\widehat{\nabla\beta}_i^\top(x_c - x_t)|^2}{2k\beta\|x_c - x_t\|^2} .$$

Now (A.11) takes the form

$$\begin{aligned}
& \frac{J^{3/2} \|\nabla\beta\|^2}{4k\beta\|x_c - x_t\|^2} + \frac{J\|\nabla\beta\|^2 |\widehat{\nabla\beta}_i^\top(x_c - x_t)|^2}{2k\beta\|x_c - x_t\|^2} \geq \frac{J\|\nabla\beta\|^2}{2k\beta} \\
& \iff \frac{J^{1/2}}{2\|x_c - x_t\|^2} + \frac{|\widehat{\nabla\beta}_i^\top(x_c - x_t)|^2}{\|x_c - x_t\|^2} \geq 1 \\
& \iff \frac{\|x_c - x_t\|^2 - r_t^2 + 2|\widehat{\nabla\beta}_i^\top(x_c - x_t)|^2}{2\|x_c - x_t\|^2} \geq 1 \\
& \iff 2|\widehat{\nabla\beta}_i^\top(x_c - x_t)|^2 \geq \|x_c - x_t\|^2 + r_t^2 . \tag{A.14}
\end{aligned}$$

For  $x_c \in \mathcal{B}_i(\epsilon)$  (guaranteed by Proposition A.0.4),  $\|x_c - x_t\| > r_t$ . Now let  $r_t$  assume the form  $r_t = \zeta \inf_{\mathcal{B}_i(\epsilon)} \|x_c - x_t\|$  for an appropriate  $\zeta < 1$ , and recall that  $\widehat{\nabla\beta}_i = \frac{\nabla\beta_i}{\|\nabla\beta_i\|}$ , where  $\nabla\beta_i = 2(x - o_i)$ . With this in mind, one satisfies (A.14) by ensuring that

$$\frac{1 + \zeta^2}{2} \leq \left( \frac{(x_c - o_i)^\top(x_c - x_t)}{\|x_c - o_i\| \|x_c - x_t\|} \right)^2 \implies 2|\widehat{\nabla\beta}_i^\top(x_c - x_t)|^2 \geq \|x_c - x_t\|^2 + r_t^2 . \tag{A.15}$$

An appropriately small choice of  $\epsilon$  can establish (A.15), as the following derivation shows:

$$\begin{aligned}
& \frac{(x_c - o_i)^\top(x_c - x_t)}{\|x_c - o_i\| \|x_c - x_t\|} \geq \\
& \frac{\frac{\sqrt{J}}{4k} [(2\|x_c - o_i\|^2)/\beta_i + [\alpha_i^\top(x_c - o_i)]/\bar{\beta}_i]}{\frac{\sqrt{J}}{4k} [(2\|x_c - o_i\|)/\beta_i + \|\alpha_i\|/\bar{\beta}_i] \|x_c - o_i\|} \geq \frac{(2\|x_c - o_i\|^2)/\beta_i - (\|\alpha_i\|\|x_c - o_i\|)/\bar{\beta}_i}{(2\|x_c - o_i\|^2)/\beta_i + (\|\alpha_i\|\|x_c - o_i\|)/\bar{\beta}_i} \\
& = \frac{1 - (\beta_i\|\alpha_i\|)/(2\bar{\beta}_i\|x_c - o_i\|)}{1 + (\beta_i\|\alpha_i\|)/(2\bar{\beta}_i\|x_c - o_i\|)} = 1 - \frac{(\beta_i\|\alpha_i\|)/(\bar{\beta}_i\|x_c - o_i\|)}{1 + (\beta_i\|\alpha_i\|)/(2\bar{\beta}_i\|x_c - o_i\|)} \\
& \geq 1 - \frac{\beta_i\|\alpha_i\|}{\bar{\beta}_i\|x_c - o_i\|} \geq 1 - \frac{\epsilon\|\alpha_i\|}{\bar{\beta}_i\|x_c - o_i\|}
\end{aligned}$$

and thus to satisfy (A.11), it suffices to pick

$$\epsilon < \left(1 - \sqrt{\frac{1 + \zeta^2}{2}}\right) \frac{\inf_i(\rho_i \inf_{\mathcal{B}_i(\epsilon)} \bar{\beta}_i)}{\sup_{\mathcal{F}_0(\epsilon)} \|\alpha_i\|} \implies \epsilon < \left(1 - \sqrt{\frac{1 + \zeta^2}{2}}\right) \frac{\bar{\beta}_i\|x_c - o_i\|}{\|\alpha_i\|} .$$

■

**Proposition A.0.7** *There exists  $k_0 > 0$  such that for any  $k > k_0$ , any critical point  $x_c \in \mathcal{B}_{x_t}(\delta_t)$  is a local maximum of  $\frac{J^k}{\beta}$ .*

**Proof** To study the critical points in  $\mathcal{B}_{x_t}(\delta_t)$ , we work on the two cases:

Case I:  $\nabla\beta|_{x_t} = 0$ ,  $x_c = x_t$ ,

$\nabla J|_{x_t} = 0 \Rightarrow k\beta(x_t)\nabla J|_{x_t} = J(x_t)\nabla\beta|_{x_t} = 0$ , we shall have  $x_t$  as one of the critical points in  $\mathcal{B}_{x_t}(\delta_t)$ . In this case, for any unit vector  $q \in \mathbb{R}^n$ :

$$\begin{aligned} & \frac{\beta^2}{J^{k-2}} q^\top \nabla^2 \left( \frac{J^k}{\beta} \right) |_{x_t} q \\ &= q^\top (k\beta J \nabla^2 J + k(k-1)\beta \nabla J \nabla J^\top - J^2 \nabla^2 \beta) q \\ &= q^\top (-4J^{1.5} k\beta \mathbf{I} - J^2 \nabla^2 \beta) q \\ &= -4r_t^6 k\beta - r_t^8 q^\top \nabla^2 \beta q . \end{aligned}$$

Recall that to make the workspace valid,  $\mathcal{B}_{x_t}(r_t)$  should not intersect  $\partial\mathcal{F}$ , then at  $x_t$ ,  $\beta_i > r_t^2$  for  $i \in \{0 \dots m\} \Rightarrow \beta > r_t^{2m}$ . So as long as

$$k > k_1 = \frac{1}{4} r_t^{(2-2m)} \sup_q (|q^\top \nabla^2 \beta q|) ,$$

$q^\top \nabla^2 \left( \frac{J^k}{\beta} \right) |_{x_t} q$  is guaranteed to be negative for any unit vector  $q \in \mathbb{R}^n$  and the critical point  $x_t$  is a local maximum of  $\frac{J^k}{\beta}$ .

Case II: For any  $x_c \neq x_t$ ,  $x_c \in \mathcal{B}_{x_t}(\delta_t)$ :

For any unit vector  $q \in \mathbb{R}^n$ ,  $q$  can be presented as scaled sum of  $v_1 = \frac{\nabla J}{\|\nabla J\|}$  and  $v_2$ , a unit vector perpendicular to  $v_1$ , i.e.  $q = q_1 v_1 + q_2 v_2$ ,  $q_1^2 + q_2^2 = 1$ ,  $q_1 q_2 > 0$ . In order to ensure that  $\nabla^2 \left( \frac{J^k}{\beta} \right)$  is negative definite at  $x_c$ , a critical point of  $\frac{J^k}{\beta}$  in  $\mathcal{B}_{x_t}(\delta_t)$ , we study the sign of  $\frac{\beta^2}{J^{k-2}} q^\top \nabla^2 \left( \frac{J^k}{\beta} \right) |_{x_c} q$ :

$$\begin{aligned} & \frac{\beta^2}{J^{k-2}} q^\top \nabla^2 \left( \frac{J^k}{\beta} \right) |_{x_c} q \\ &= \frac{\beta^2}{J^{k-2}} \left( q_1^2 v_1^\top \nabla^2 \left( \frac{J^k}{\beta} \right) |_{x_c} v_1 + q_2^2 v_2^\top \nabla^2 \left( \frac{J^k}{\beta} \right) |_{x_c} v_2 + q_1 q_2 v_1^\top \nabla^2 \left( \frac{J^k}{\beta} \right) |_{x_c} v_2 + q_1 q_2 v_2^\top \nabla^2 \left( \frac{J^k}{\beta} \right) |_{x_c} v_1 \right) . \end{aligned} \tag{A.16}$$

Recall that at critical point  $x_c$ ,  $k\beta \nabla J = J \nabla \beta$ . Take the norm of both side:

$$k\beta(4J^{0.5} \|x_c - x_t\|) = J \|\nabla \beta\| , \quad k \|x_c - x_t\| = J^{0.5} \frac{\|\nabla \beta\|}{4\beta} . \tag{A.17}$$

The first term in (A.16) can be expanded as:

$$\begin{aligned}
& q_1^2 \frac{\beta^2}{J^{k-2}} v_1^\top \nabla^2 \left( \frac{J^k}{\beta} \right) |_{x_c} v_1 \\
&= q_1^2 v_1^\top (k\beta J \nabla^2 J + k(k-1)\beta \nabla J \nabla J^\top - J^2 \nabla^2 \beta) v_1 \\
&= q_1^2 v_1^\top (k\beta J [8(x_c - x_t)(x_c - x_t)^\top - 4J^{0.5} \mathbf{I}] + k(k-1)\beta \nabla J \nabla J^\top - J^2 \nabla^2 \beta) v_1 \\
&= q_1^2 (8k(2k-1)\beta J \|x_c - x_t\|^2 - 4k\beta J^{1.5} - J^2 v_1^\top \nabla^2 \beta v_1) \\
&\stackrel{(A.17)}{=} q_1^2 \left( \frac{J^2 \|\nabla \beta\|^2}{\beta} - 2J^{1.5} \|\nabla \beta\| \|x_c - x_t\| - J^2 v_1^\top \nabla^2 \beta v_1 - 4k\beta J^{1.5} \right) \\
&\leq q_1^2 \left( \frac{J^2 \|\nabla \beta\|^2}{\beta} - J^2 v_1^\top \nabla^2 \beta v_1 - 4k\beta J^{1.5} \right) .
\end{aligned}$$

Since  $v_2$  is an arbitrary unit vector that is perpendicular to  $\nabla J$ , it is also perpendicular to  $(x_c - x_t)$ . The second term in (A.16) can be expanded as:

$$\begin{aligned}
& q_2^2 \frac{\beta^2}{J^{k-2}} v_2^\top \nabla^2 \left( \frac{J^k}{\beta} \right) |_{x_c} v_2 \\
&= q_2^2 v_2^\top (k\beta J \nabla^2 J + k(k-1)\beta \nabla J \nabla J^\top - J^2 \nabla^2 \beta) v_2 \\
&= q_2^2 v_2^\top (k\beta J [8(x_c - x_t)(x_c - x_t)^\top - 4J^{0.5} \mathbf{I}] + k(k-1)\beta \nabla J \nabla J^\top - J^2 \nabla^2 \beta) v_2 \\
&= q_2^2 (-4k\beta J^{1.5} - J^2 v_2^\top \nabla^2 \beta v_2) .
\end{aligned}$$

Similarly we shall have:

$$\begin{aligned}
q_1 q_2 \frac{\beta^2}{J^{k-2}} v_1^\top \nabla^2 \left( \frac{J^k}{\beta} \right) |_{x_c} v_2 &= q_1 q_2 (-J^2 v_1^\top \nabla^2 \beta v_2) , \\
q_1 q_2 \frac{\beta^2}{J^{k-2}} v_2^\top \nabla^2 \left( \frac{J^k}{\beta} \right) |_{x_c} v_1 &= q_1 q_2 (-J^2 v_2^\top \nabla^2 \beta v_1) .
\end{aligned}$$

Since  $\nabla^2 \beta$  is symmetric,  $v_1^\top \nabla^2 \beta v_2 = v_2^\top \nabla^2 \beta v_1$ . Now (A.16) can be upper bounded by:

$$\begin{aligned}
& \frac{\beta^2}{J^{k-2}} q^\top \nabla^2 \left( \frac{J^k}{\beta} \right) |_{x_c} q \\
&\leq q_1^2 \left( \frac{J^2 \|\nabla \beta\|^2}{\beta} - J^2 v_1^\top \nabla^2 \beta v_1 - 4k\beta J^{1.5} \right) + q_2^2 (-4k\beta J^{1.5} - J^2 v_2^\top \nabla^2 \beta v_2) \\
&\quad + q_1 q_2 (-J^2 v_1^\top \nabla^2 \beta v_2) + q_1 q_2 (-J^2 v_2^\top \nabla^2 \beta v_1) \\
&= -4k\beta J^{1.5} + q_1^2 \left( \frac{J^2 \|\nabla \beta\|^2}{\beta} - J^2 v_1^\top \nabla^2 \beta v_1 \right) + q_2^2 (-J^2 v_2^\top \nabla^2 \beta v_2) + 2q_1 q_2 (-J^2 v_1^\top \nabla^2 \beta v_2)
\end{aligned}$$

$$\leq -4k\beta J^{1.5} + J^2\left(\frac{\|\nabla\beta\|^2}{\beta} + |v_1^\top \nabla^2 \beta v_1| + |v_2^\top \nabla^2 \beta v_2| + |v_1^\top \nabla^2 \beta v_2|\right) .$$

Recall that to make the workspace valid,  $\mathcal{B}_{x_t}(r_t)$  should not intersect  $\partial\mathcal{F}$ , then in  $\mathcal{B}_{x_t}(\delta_t)$ ,  $\beta_i > (r_t - \delta_t)^2$  for  $i \in \{0 \dots m\} \Rightarrow \beta > (r_t - \delta_t)^{2m}$ , and  $J \leq r_t^4$ . So as long as

$$k > k_2 = \frac{r_t^2}{4(r_t - \delta_t)^{2m}} \left[ \sup_{x_c \in \mathcal{B}_{x_t}(\delta_t)} \left( \frac{\|\nabla\beta\|^2}{\beta} + |v_1^\top \nabla^2 \beta v_1| + |v_2^\top \nabla^2 \beta v_2| + |v_1^\top \nabla^2 \beta v_2| \right) \right] ,$$

we shall satisfy  $q^\top \nabla^2(\frac{J^k}{\beta})|_{x_c} q < 0$  for any  $q \in \mathbb{R}^n$  and any critical point  $x_c$  in  $\mathcal{B}_{x_t}(\delta_t)$  other than  $x_t$  is guaranteed to be local maximum of  $\frac{J^k}{\beta}$ .

To sum up two cases,  $k > k_0 = \max\{k_1, k_2\}$  will guarantee any critical point in  $\mathcal{B}_{x_t}(\delta_t)$  to be local maximum of  $\frac{J^k}{\beta}$ .

## Appendix B

### COPYRIGHT PERMISSIONS

This dissertation includes material from the following paper: [65] with IEEE copyright policy, [64] with Springer copyright policy, [50] with Elsevier copyright policy and consent from other authors. The related copyright policies and consent letters are attached.

## IEEE COPYRIGHT AND CONSENT FORM

To ensure uniformity of treatment among all contributors, other forms may not be substituted for this form, nor may any wording of the form be changed. This form is intended for original material submitted to the IEEE and must accompany any such material in order to be published by the IEEE. Please read the form carefully and keep a copy for your files.

TITLE OF PAPER/ARTICLE/REPORT, INCLUDING ALL CONTENT IN ANY FORM, FORMAT, OR MEDIA (hereinafter, "The Work"): **Active Sensor Networks for Nuclear Detection**

COMPLETE LIST OF AUTHORS: **Jianxin Sun, Herbert G. Tanner, Ioannis Poulakakis**

IEEE PUBLICATION TITLE (Journal, Magazine, Conference, Book): **2015 IEEE International Conference on Robotics and Automation, May 26-30, 2015, Washington State Convention Center, Seattle, Washington**

### COPYRIGHT TRANSFER

1. The undersigned hereby assigns to The Institute of Electrical and Electronics Engineers, Incorporated (the "IEEE") all rights under copyright that may exist in and to: (a) the above Work, including any revised or expanded derivative works submitted to the IEEE by the undersigned based on the Work; and (b) any associated written or multimedia components or other enhancements accompanying the Work.

### CONSENT AND RELEASE

2. In the event the undersigned makes a presentation based upon the Work at a conference hosted or sponsored in whole or in part by the IEEE, the undersigned, in consideration for his/her participation in the conference, hereby grants the IEEE the unlimited, worldwide, irrevocable permission to use, distribute, publish, license, exhibit, record, digitize, broadcast, reproduce and archive, in any format or medium, whether now known or hereafter developed: (a) his/her presentation and comments at the conference; (b) any written materials or multimedia files used in connection with his/her presentation; and (c) any recorded interviews of him/her (collectively, the "Presentation"). The permission granted includes the transcription and reproduction of the Presentation for inclusion in products sold or distributed by IEEE and live or recorded broadcast of the Presentation during or after the conference.

3. In connection with the permission granted in Section 2, the undersigned hereby grants IEEE the unlimited, worldwide, irrevocable right to use his/her name, picture, likeness, voice and biographical information as part of the advertisement, distribution and sale of products incorporating the Work or Presentation, and releases IEEE from any claim based on right of privacy or publicity.

4. The undersigned hereby warrants that the Work and Presentation (collectively, the "Materials") are original and that he/she is the author of the Materials. To the extent the Materials incorporate text passages, figures, data or other material from the works of others, the undersigned has obtained any necessary permissions. Where necessary, the undersigned has obtained all third party permissions and consents to grant the license above and has provided copies of such permissions and consents to IEEE.

Please check this box if you do not wish to have video/audio recordings made of your conference presentation.

See below for Retained Rights/Terms and Conditions, and Author Responsibilities.

### AUTHOR RESPONSIBILITIES

The IEEE distributes its technical publications throughout the world and wants to ensure that the material submitted to its publications is properly available to the readership of those publications. Authors must ensure that their Work meets the requirements as stated in section 8.2.1 of the IEEE

PSPB Operations Manual, including provisions covering originality, authorship, author responsibilities and author misconduct. More information on IEEE's publishing policies may be found at [http://www.ieee.org/publications\\_standards/publications/rights/authorrightsresponsibilities.html](http://www.ieee.org/publications_standards/publications/rights/authorrightsresponsibilities.html). Authors are advised especially of IEEE PSPB Operations Manual section 8.2.1.B12: "It is the responsibility of the authors, not the IEEE, to determine whether disclosure of their material requires the prior consent of other parties and, if so, to obtain it." Authors are also advised of IEEE PSPB Operations Manual section 8.1.1B: "Statements and opinions given in work published by the IEEE are the expression of the authors."

## **RETAINED RIGHTS/TERMS AND CONDITIONS**

### **General**

1. Authors/employers retain all proprietary rights in any process, procedure, or article of manufacture described in the Work.
2. Authors/employers may reproduce or authorize others to reproduce the Work, material extracted verbatim from the Work, or derivative works for the author's personal use or for company use, provided that the source and the IEEE copyright notice are indicated, the copies are not used in any way that implies IEEE endorsement of a product or service of any employer, and the copies themselves are not offered for sale.
3. In the case of a Work performed under a U.S. Government contract or grant, the IEEE recognizes that the U.S. Government has royalty-free permission to reproduce all or portions of the Work, and to authorize others to do so, for official U.S. Government purposes only, if the contract/grant so requires.
4. Although authors are permitted to re-use all or portions of the Work in other works, this does not include granting third-party requests for reprinting, republishing, or other types of re-use. The IEEE Intellectual Property Rights office must handle all such third-party requests.
5. Authors whose work was performed under a grant from a government funding agency are free to fulfill any deposit mandates from that funding agency.

### **Author Online Use**

6. Personal Servers. Authors and/or their employers shall have the right to post the accepted version of IEEE-copyrighted articles on their own personal servers or the servers of their institutions or employers without permission from IEEE, provided that the posted version includes a prominently displayed IEEE copyright notice and, when published, a full citation to the original IEEE publication, including a link to the article abstract in IEEE Xplore. Authors shall not post the final, published versions of their papers.
7. Classroom or Internal Training Use. An author is expressly permitted to post any portion of the accepted version of his/her own IEEE-copyrighted articles on the authors personal web site or the servers of the authors institution or company in connection with the authors teaching, training, or work responsibilities, provided that the appropriate copyright, credit, and reuse notices appear prominently with the posted material. Examples of permitted uses are lecture materials, course packs, e-reserves, conference presentations, or in-house training courses.
8. Electronic Preprints. Before submitting an article to an IEEE publication, authors frequently post their manuscripts to their own web site, their employers site, or to another server that invites constructive comment from colleagues. Upon submission of an article to IEEE, an author is required to transfer copyright in the article to IEEE, and the author must update any previously posted version of the article with a prominently displayed IEEE copyright notice. Upon publication of an article by the IEEE, the author must replace any previously posted electronic versions of the article with either (1) the full citation to the IEEE work with a Digital Object Identifier (DOI) or link to the article abstract in IEEE Xplore, or (2) the accepted version only (not the IEEE-published version), including the IEEE copyright notice and full citation, with a link to the final, published article in IEEE Xplore.

## **INFORMATION FOR AUTHORS**

### **IEEE Copyright Ownership**

It is the formal policy of the IEEE to own the copyrights to all copyrightable material in its technical publications and to the individual contributions contained therein, in order to protect the interests of the IEEE, its authors and their employers, and, at the same time, to facilitate the appropriate re-use of this material by others. The IEEE distributes its technical publications throughout the world and does so by various means such as hard copy, microfiche, microfilm, and electronic media. It also abstracts and may translate its publications, and articles contained therein, for inclusion in various compendiums, collective works, databases and similar publications.

### **Author/Employer Rights**

If you are employed and prepared the Work on a subject within the scope of your employment, the copyright in the Work belongs to your employer as a work-for-hire. In that case, the IEEE assumes that when you sign this Form, you are authorized to do so by your employer and that your employer has consented to the transfer of copyright, to the representation and warranty of publication rights, and to all other terms and conditions of this Form. If such authorization and consent has not been given to you, an authorized representative of your employer should sign this Form as the Author.

### **GENERAL TERMS**

1. The undersigned represents that he/she has the power and authority to make and execute this form.
2. The undersigned agrees to identify and hold harmless the IEEE from any damage or expense that may arise in the event of a breach of any of the warranties set forth above.
3. In the event the above work is not accepted and published by the IEEE or is withdrawn by the author(s) before acceptance by the IEEE, the foregoing grant of rights shall become null and void and all materials embodying the Work submitted to the IEEE will be destroyed.
4. For jointly authored Works, all joint authors should sign, or one of the authors should sign as authorized agent for the others.

**Jianxin Sun**

**Author/Authorized Agent For Joint Authors**

**26-02-2015**

**Date(dd-mm-yy)**

THIS FORM MUST ACCOMPANY THE SUBMISSION OF THE AUTHOR'S MANUSCRIPT.

Questions about the submission of the form or manuscript must be sent to the publication's editor. Please direct all questions about IEEE copyright policy to:

IEEE Intellectual Property Rights Office, copyrights@ieee.org, +1-732-562-3966 (telephone)

From: **Springer** [springerauthorquery@springeronline.com](mailto:springerauthorquery@springeronline.com)  
Subject: **Copyright Transfer Statement (CTS) for your article in Autonomous Robots (9468)**  
Date: July 9, 2015 at 3:36 PM  
To: [jxsun@udel.edu](mailto:jxsun@udel.edu)

S



*Copyright Transfer*

09.07.2015

visit us at [springer.com](http://springer.com)

## Confirmation of your Copyright Transfer

Dear Author,

Please note: This e-mail is a confirmation of your copyright transfer and was sent to you only for your own records.

The copyright to this article, including any graphic elements therein (e.g. illustrations, charts, moving images), is hereby assigned for good and valuable consideration to Springer Science+Business Media New York effective if and when the article is accepted for publication and to the extent assignable if assignability is restricted for by applicable law or regulations (e.g. for U.S. government or crown employees). Author warrants (i) that he/she is the sole owner or has been authorized by any additional copyright owner to assign the right, (ii) that the article does not infringe any third party rights and no license from or payments to a third party is required to publish the article and (iii) that the article has not been previously published or licensed.

The copyright assignment includes without limitation the exclusive, assignable and sublicensable right, unlimited in time and territory, to reproduce, publish, distribute, transmit, make available and store the article, including abstracts thereof, in all forms of media of expression now known or developed in the future, including pre- and reprints, translations, photographic reproductions and microform. Springer may use the article in whole or in part in electronic form, such as use in databases or data networks for display, print or download to stationary or portable devices. This includes interactive and multimedia use and the right to alter the article to the extent necessary for such use.

Authors may self-archive the Author's accepted manuscript of their articles on their own websites. Authors may also deposit this version of the article in any repository, provided it is only made publicly available 12 months after official publication or later. He/she may not use the publisher's version (the final article), which is posted on SpringerLink and other Springer websites, for the purpose of self-archiving or deposit. Furthermore, the Author may only post his/her version provided acknowledgement is given to the original source of publication and a link is inserted to the published article on Springer's website. The link must be provided by inserting the DOI number of the article in the following sentence: "The final publication is available at Springer via [http://dx.doi.org/\[insert DOI\]](http://dx.doi.org/[insert DOI])".

Prior versions of the article published on non-commercial pre-print servers like arXiv.org can remain on these servers and/or can be updated with Author's accepted version. The final published version (in pdf or html/xml format) cannot be used for this purpose. Acknowledgement needs to be given to the final publication and a link must be inserted to the published article on Springer's website, by inserting the DOI number of the article in the following sentence: "The final publication is available at Springer via [http://dx.doi.org/\[insert DOI\]](http://dx.doi.org/[insert DOI])". Author retains the right to use his/her article for his/her further scientific career by including the final published journal article in other publications such as dissertations and postdoctoral qualifications provided acknowledgement is given to the original source of publication.

Articles disseminated via <http://link.springer.com> are indexed, abstracted and referenced by many abstracting and information services, bibliographic networks, subscription agencies, library networks, and consortia.

After submission of the agreement signed by the corresponding author, changes of authorship or in the order of the authors listed will not be accepted by Springer.

This is an automated e-mail; please do not reply to this account. If you have any questions, please go to our [help pages](#).

Thank you very much.

Kind regards,

Springer Author Services

[Article Details](#)

---

**Journal title**

Autonomous Robots

**DOI**

10.1007/s10514-015-9468-6

**Copyright transferred to**

Springer Science+Business Media New York

**Article title**

Constrained Decision-making for Low-count Radiation Detection by Mobile Sensors

**Corresponding Author**

Jianxin Sun

**Transferred on**

Thu Jul 09 21:36:38 CEST 2015

---

**What would you like to do next?****The New SpringerLink**

Delivering results with the speed, accuracy and convenience that today's researchers need.

 [FIND OUT MORE](#)

**MySpringer for Authors**

Your personal page at Springer: the publication status of your article and your discounts and much more...

 [LOG IN NOW](#)

---

**Service Contacts****Springer Customer Service Center**

Haberstr. 7  
69129 Heidelberg  
Germany  
phone: +49 6221 345 0  
fax: +49 6221 345 4229  
[customerservice@springer.com](mailto:customerservice@springer.com)

**Springer New York, LCC**

233 Spring Street  
New York, NY 10013  
USA  
phone: +1 212 460 1500 or 800-SPRINGER  
(Weekdays 8:30am - 5:30pm ET)  
fax: +1 212-460-1700  
[customerservice@springer.com](mailto:customerservice@springer.com)

---

## Personal use

Authors can use their articles, in full or in part, for a wide range of scholarly, non-commercial purposes as outlined below:

- Use by an author in the author's classroom teaching (including distribution of copies, paper or electronic)
- Distribution of copies (including through e-mail) to known research colleagues for their personal use (but not for Commercial Use)
- Inclusion in a thesis or dissertation (provided that this is not to be published commercially)
- Use in a subsequent compilation of the author's works
- Extending the Article to book-length form
- Preparation of other derivative works (but not for Commercial Use)
- Otherwise using or re-using portions or excerpts in other works

These rights apply for all Elsevier authors who publish their article as either a subscription article or an open access article. In all cases we require that all Elsevier authors always include a full acknowledgement and, if appropriate, a link to the final published version hosted on Science Direct.

Copyright © 2016 Elsevier B.V.

Advertising (<https://www.elsevier.com/advertisers>) - Careers (<https://www.elsevier.com/about/careers>) - Feedback (<https://www.elsevier.com/feedback>) - Sitemap (<https://www.elsevier.com/sitemap>) - Terms and Conditions (<https://www.elsevier.com/legal/elsevier-website-terms-and-conditions>) - Privacy Policy (<https://www.elsevier.com/legal/privacy-policy>) - Help and Contact (<https://service.elsevier.com>)

Cookies are used by this site. To decline or learn more, visit our Cookies (<https://www.elsevier.com/legal/use-of-cookies>) page.





Jianxin Sun &lt;jxsun@udel.edu&gt;

---

## Permission to use material from the 2014 Automatica paper in Jianxin's PhD dissertation

4 messages

---

**Jianxin Sun** <jxsun@udel.edu>

Fri, Feb 26, 2016 at 8:53 PM

To: cdpahlajani@iitgn.ac.in, Herbert Tanner &lt;btanner@udel.edu&gt;, Ioannis Poulakakis &lt;poulakas@udel.edu&gt;

Dear Authors,

I am writing this letter to ask permission for using the material from the following paper in my PhD dissertation:

*Error probability bounds for nuclear detection: Improving accuracy through controlled mobility.* Chetan D. Pahlajani, Jianxin Sun, Ioannis Poulakakis and Herbert G. Tanner. *Automatica*, vol. 50, issue 10 (2014), pp. 2470-2481

To abide the copyright rules, an email/letter permission should be obtained from all the authors before finalizing the dissertation.

I would like to use the following materials in my dissertation:

1. A rewritten combination of section 3.2 "Realizing the Probability Bounds" and section 4 "Analytical Threshold Selection" (Section 3.2 in dissertation draft)
2. Section 3.3 Error Probabilities: Bounds and Monte Carlo Estimates (Section 6.1 in dissertation draft)
3. Section 5 Optimal Control of Mobile Sensors (Section 3.3.2 in dissertation draft)
4. Section 6 Experimental Results in One Dimension (Section 7.5.1 in dissertation draft)
5. Rewritten paragraph 5 and 7 in the introduction (Section 1.4.1 in dissertation draft)

Please review the attached dissertation draft and let me know if you have any concern over the usage of the material listed here.

Regards,

Jianxin Sun  
Ph.D. Candidate  
Cooperative Robotics Lab  
University of Delaware

---

 **dissertation-main.pdf**  
7341K

---

**Tanner, Herbert Glenn** <btanner@udel.edu>

Sat, Feb 27, 2016 at 8:33 AM

To: "Sun, Jianxin" &lt;jxsun@udel.edu&gt;, "cdpahlajani@iitgn.ac.in" &lt;cdpahlajani@iitgn.ac.in&gt;, "Poulakakis, Ioannis" &lt;poulakas@udel.edu&gt;

Jianxin,

I believe that if you properly acknowledge the source at every instance, there should be no

issue with copyright from at least my side.

---

Herbert G. Tanner  
Associate Professor  
Mechanical Engineering  
University of Delaware

---

**From:** Jianxin Sun <jxsun@udel.edu>  
**Sent:** Friday, February 26, 2016 8:53 PM  
**To:** cdpahlajani@iitgn.ac.in; Tanner, Herbert Glenn; Poulakakis, Ioannis  
**Subject:** Permission to use material from the 2014 Automatica paper in Jianxin's PhD dissertation

[Quoted text hidden]

---

**Ioannis Poulakakis** <poulakas@udel.edu> Sun, Feb 28, 2016 at 5:55 PM  
To: "Tanner, Herbert Glenn" <btanner@udel.edu>  
Cc: "Sun, Jianxin" <jxsun@udel.edu>, "cdpahlajani@iitgn.ac.in" <cdpahlajani@iitgn.ac.in>

Jianxin,

I am not sure, but I believe that we have transferred the copyright to the journal. If you want to be rigorous about copyright, you should contact the journal, but I don't think this is necessary. In any case, I have no issue with respect to using this material as part of your PhD thesis.

Thanks,

Ioannis

[Quoted text hidden]

--

---

Ioannis Poulakakis, PhD

Assistant Professor  
Department of Mechanical Engineering  
University of Delaware

130 Academy Street (108 SPL)  
Newark, DE 19716-3140, U.S.A.

Phone: (+1) 302-831-3563 (office)  
Fax: (+1) 302-831-3619 (office)  
E-Mail: poulakas@udel.edu  
Web: <http://research.me.udel.edu/~poulakas/>

---

---

**Chetan Pahlajani** <cdpahlajani@iitgn.ac.in> Sun, Feb 28, 2016 at 10:45 PM  
To: Ioannis Poulakakis <poulakas@udel.edu>  
Cc: "Tanner, Herbert Glenn" <btanner@udel.edu>, "Sun, Jianxin" <jxsun@udel.edu>

Jianxin,

As long as good practices about citing sources is followed (as in Bert's email), there are no concerns about using the material from my end.

In terms of copyright, I think Ioannis is right; I'm pretty sure we have transferred copyright to the journal. But I would think that journal policy does allow authors to use it for personal purposes such as dissertations.

And finally, congratulations! It seems that the completion of your PhD is within sight!

[Quoted text hidden]

--

Best regards,  
Chetan D. Pahlajani  
Assistant Professor, Mathematics  
IIT Gandhinagar  
VGEC Campus, Chandkheda  
Ahmedabad, Gujarat 382 424  
Webpage: <https://sites.google.com/site/chetanpahlajani/>